

# PHOTONIC SLABS WITH ANISOTROPIC COLLOID AND COLLOID INSPIRED BASES

A Dissertation

Presented to the Faculty of the Graduate School  
of Cornell University

in Partial Fulfillment of the Requirements for the Degree of  
Doctor of Philosophy

by

Erin Kathleen Riley

May 2014

© 2014 Erin Kathleen Riley  
ALL RIGHTS RESERVED

PHOTONIC SLABS WITH ANISOTROPIC COLLOID AND COLLOID INSPIRED  
BASES

Erin Kathleen Riley, Ph.D.

Cornell University 2014

The concept of photonic crystals as 'semiconductors for light' has given rise to strategies for the design and fabrication of periodic dielectric materials with dramatic effects on photon dispersion relations. Photonic crystal theory has revealed numerous reduced symmetry and/or complex basis champion structures that enhance light-matter interactions and promote photonic band gap properties. Realizations of such structures at visible and near infrared wavelengths are often challenging and may be achieved a decade or more after they are envisioned. Colloidal self-assembly routes, in particular, have been desired for visible light control, low cost, ability to span from two- to three- dimensions and potentially large area, parallel processing. Thermodynamic simulation literature in the context of supramolecular chemistry studies indicates non-spherical building blocks hold promise for incorporating a rich diversity of packing arrangements inaccessible with commonly available spherical bases. Investigations in the synthesis and processing science foundations for obtaining order (i.e., mesophases and crystals) along with the optical characterization consistent with the thin film forms are essential to understanding structure-property correlations for photonic solids from colloids.

This dissertation demonstrates the application of physical confinement to direct self-assembly. In addition, the photonic band gap characterization of two-dimensional (2D) and quasi-2D structures from mushroom cap and asymmetric dimer shaped colloids was performed using photonic crystal 'slab' configurations. Aqueous suspensions of micron-sized mushroom cap-shaped particles were self-organized by gravitational sedimentation

in a wedge-shaped confinement cell. The sequence of phases with increased cell height was studied with precise spatial and temporal resolution via fast confocal microscopy. In addition to the phase symmetry transitions found for spheres, rotator (i.e., plastic crystal) and orientation-dependent states were determined. The photonic band gap forming properties of the buckled phase observed in the mushroom-cap particle system under confinement were theoretically modeled. The 2D finite height photonic crystals with dielectric shaping in three dimensions imparted variation to the cross-sectional profile of the slab. The configuration is atypical for lithographic realizations of photonic slabs and also for 2D photonic crystal models assumed to extend infinitely with fixed cross-section along the  $z$ -axis. The experimentally tunable variables of shape and degree of buckling were captured using structural parameters. Complete band gaps in the guided modes were determined as a function of shape parameters, lattice distortion, filling fraction, refractive index contrast between low and high dielectric regions, etc. Slab structures were also modeled based on dimers (i.e., two adjacent or overlapping spheres) in centered-rectangular lattices previously realized through convective (i.e., evaporation-assisted) or confinement self-assembly. The degree of lobe fusion and the degree of lobe symmetry shape parameters accessible experimentally were mapped in addition to the structural and materials parameters. Large band gaps for each light polarization as well as polarization independent band gaps were found in a wide range of structures. Additionally, dimer cylinder bases on centered rectangular lattices were modeled to compare properties of realizations consistent with microfabrication using lithography and with colloidal processing for self-assembly of photonic templates. The study suggests that the ideation for structural design in slabs can be enriched by the combination of thermodynamically-inspired structures with the ease of optimizing slab height (i.e., through lithographic fabrication).

## BIOGRAPHICAL SKETCH

Erin Riley was born and raised in Melbourne, Florida. From a young age, she has been fascinated with light and its interactions with materials. She double majored in Physics and Electrical Engineering at the University of Central Florida (UCF). While at UCF, she served as vice-president and president of the Society of Physics Students (SPS). For three summers she interned as an undergraduate student at Harris Corporation. At the Harris Electro-Optics Center she worked on several projects including modeling photonic crystal fiber structures under Dr. Michael Lange, Senior Scientist and Harris Fellow. In the summer of 2006, she participated in an International Research Experience for Undergraduates at the University of Bordeaux 1. Working in the lab of Dr. Lionel Canoni, she investigated the formation of silver complexes and of silver nanoparticles following femtosecond irradiation of a Ag-doped phosphate glass. These experiences emphasized the influence and limitations of materials on engineering desirable optical properties. She graduated summa cum laude in 2007 and moved to Ithaca, NY to continue her studies at Cornell University in the Department of Materials Science and Engineering. She joined the Colloid Based Materials Research Lab (CBMRL), under the supervision of Professor Chekesha M. Liddell Watson. In 2008, she received a National Science Foundation Graduate Fellowship (NSF, accepted), a National Defense Science and Engineering Graduate Fellowship (NDSEG, accepted) and a Science, Mathematics, and Research for Transformation Defense Scholarship fellowship for Service (SMART, declined). Her work focused on the self-assembly and optical properties of non-spherical based colloidal crystals. Erin earned her M.S. degree from Cornell in 2011, and completed her doctoral work in the spring of 2014.

To my family.

## ACKNOWLEDGEMENTS

A number of people have influenced my life and helped me reach this goal. First, I would like to thank my advisor, Prof. Chekesha Liddell Watson, whose support and interest to cultivate learning was always appreciated. I would also like to thank my committee members, Prof. Michal Lipson and Prof. Richard Hennig for their support and assistance.

Many thanks to all present and past members of the Liddell Watson group. You made going to lab fun as well as exciting. Especial thanks also to my collaborators— Sharon Gerbode, Mark Buckley, Umang Argawal, Carlos Jimenez, Prof. Itai Cohen and Prof. Fernando Escobedo— for advancing the crazy ideas, stimulating conversations and lab trouble-shooting. To the Cohen group, thank you for letting your lab be a second home. I also want to thank my funding agencies, the National Science Foundation, the Department of Defense and the Department of Energy, for making this research possible. Additional thanks to the staff at NBTC, BRC and CNF for support and equipment assistance and to the Materials Science and Engineering Department staff. Thank you for keeping my head on straight. Special appreciation to the Harris Corporation Electro-Optic Center and, in particular, Dr. Michael Lange and Pat Bentley, for answering endless questions, stimulating my interest in the field and welcoming a high-school student into the lab.

Finally, I would like to thank my friends for all the Settlers matches, being sounding boards and keeping me grounded. You made my time in Ithaca enjoyable. Lastly, I want to thank my family— for their endless support, love and putting up with me— and Yogesh Sharma for bringing the light into my world. Without you, none of this would be possible.

## TABLE OF CONTENTS

Biographical Sketch . . . . .	iii
Dedication . . . . .	iv
Acknowledgements . . . . .	v
Table of Contents . . . . .	vi
List of Tables . . . . .	viii
List of Figures . . . . .	ix
<b>1 Introduction</b>	<b>1</b>
1.1 Photonic Crystals . . . . .	1
1.2 Self-assembly . . . . .	6
References . . . . .	10
<b>2 Confinement-Controlled Self Assembly of Colloids with Simultaneous Isotropic &amp; Anisotropic Cross-Section</b>	<b>17</b>
2.1 Abstract . . . . .	17
2.2 Introduction . . . . .	18
2.3 Experimental Section . . . . .	21
2.3.1 Particle Synthesis . . . . .	21
2.3.2 Particle Assembly . . . . .	22
2.4 Results and Discussion . . . . .	23
2.5 Conclusion . . . . .	39
References . . . . .	42
<b>3 Buckled Colloidal Crystals with Nonspherical Bases for Two-Dimensional Slab Photonic Band Gaps</b>	<b>48</b>
3.1 Abstract . . . . .	48
3.2 Introduction . . . . .	49
3.3 Model and Calculation . . . . .	54
3.4 Results and Discussion . . . . .	58
3.5 Conclusions . . . . .	74
3.6 Acknowledgments . . . . .	74
3.7 Appendix: Synthesis Procedures . . . . .	75
References . . . . .	77
<b>4 Slab Photonic Crystals with Dimer Colloid Bases</b>	<b>81</b>
4.1 Abstract . . . . .	81
4.2 Introduction . . . . .	82
4.3 Computational Method . . . . .	84
4.4 Results and Discussion . . . . .	87
4.5 Conclusions . . . . .	104
References . . . . .	105

<b>5</b>	<b>Slab Photonic Crystals With Dimer Cylinder Bases</b>	<b>110</b>
5.1	Abstract . . . . .	110
5.2	Introduction . . . . .	111
5.3	Computational Method . . . . .	115
5.4	Results and Discussion . . . . .	117
5.5	Conclusions . . . . .	144
	References . . . . .	145

## LIST OF TABLES

2.1	Confinement height and density corresponding to monolayer and bilayer structures of mushroom caps . . . . .	38
3.1	Largest photonic band gaps in tangent buckled structures . . . . .	71
3.2	Largest photonic band gaps in non-tangent buckled structures . . . . .	71
4.1	Shape and structural parameters yielding maximum gap sizes in centered rectangular dimer slabs . . . . .	101
5.1	Shape and structural parameters yielding maximum gap sizes for direct dimer cylinder slabs . . . . .	132

## LIST OF FIGURES

1.1	Biological examples of photonic crystals with dielectric periodicity in one-, two- and three dimensions. . . . .	2
1.2	1D photonic crystal with alternating dielectric constant values . . . . .	4
2.1	SEM image perspective views of mushroom cap particles and confinement cell schematic . . . . .	22
2.2	Wedge confinement cell with side and top views of idealized phases for mushroom caps . . . . .	24
2.3	Confocal image and structural characterization for hexagonal monolayer region in wedge cell . . . . .	25
2.4	Confocal image of buckled monolayer region in wedge cell . . . . .	27
2.5	Confocal image and structural characterization for sides monolayer region in wedge cell . . . . .	29
2.6	Confocal image and structural characterization for square bilayer region in wedge cell . . . . .	31
2.7	Confocal image and structural characterization for hexagonal bilayer region in wedge cell . . . . .	32
2.8	Confocal images and structural characterization for sides bilayer region in wedge cell . . . . .	34
2.9	Structural characterization for smectic-like sides bilayer region in wedge cell. . . . .	35
2.10	Effective density of idealized phases for mushroom cap particles as a function of confinement cell height . . . . .	38
2.11	Idealized oblique structures of sides monolayer phase . . . . .	40
3.1	SEM images of mushroom cap morphologies from seeded emulsion polymerization . . . . .	50
3.2	Model buckled structure schematics of unit cell and Brillouin zone . . . . .	51
3.3	Schematics of direct and inverted buckled structures . . . . .	52
3.4	Band diagrams of inverted buckled mushroom cap structures as a function of toroidal shape parameter . . . . .	57
3.5	Dielectric filling fraction as a function of toroidal shape parameter for inverted buckled structures . . . . .	59
3.6	Relative gap width as a function of dielectric contrast for inverted buckled structures . . . . .	61
3.7	Displacement field at M symmetry point for inverted buckled structures of mushroom caps . . . . .	62
3.8	12 – 13 band gap in square bilayer as a function of toroidal shape parameter	64
3.9	14 – 15 gap and 16 – 17 gap in square bilayer structures as a function of toroidal shape parameter . . . . .	65
3.10	Band gaps for inverted square bilayer structures as a function of toroidal shape parameters . . . . .	68

3.11	Band diagrams of direct buckled structures with rectangular aspect ratio of 1.02 and dielectric contrast of 14.0 . . . . .	70
3.12	Contour map of the largest gaps for inverted buckled structures . . . . .	73
4.1	SEM images of asymmetric dimers and schematics of centered rectangular dimer structure model unit cell and Brillouin zone . . . . .	85
4.2	Band diagrams for direct asymmetric dimer structures as a function of filling fraction . . . . .	88
4.3	Contour plots of largest odd mode gaps in direct asymmetric dimer structures and contour plots of dielectric filling fraction as a function of shape parameters . . . . .	89
4.4	Contour plots of largest even mode gaps in direct asymmetric dimer structures as a function of shape parameters . . . . .	90
4.5	Schematics of representative asymmetric dimer structures . . . . .	91
4.6	Contour plots of maximum polarization independent gaps in direct asymmetric dimer structures as a function of shape parameters . . . . .	93
4.7	Representative gap maps for separation parameter, $r_l = 0.40$ , asymmetric dimer arrangements . . . . .	95
4.8	Gap maps for asymmetric dimer structures with $r_l$ values of 0.35 and 0.45 . . . . .	97
4.9	Contour plots of minimum dielectric contrasts of odd mode gaps for dimer slabs . . . . .	98
4.10	Contour plots of minimum dielectric contrasts at which even mode gaps open for dimer slabs . . . . .	99
4.11	Contour plots of minimum dielectric contrast for polarization independent gaps in dimers . . . . .	100
4.12	Band diagram for a dimer cylinder-based photonic crystal . . . . .	103
5.1	Schematics depicting unit cells and Brillouin zones for centered rectangular dimer cylinders . . . . .	114
5.2	Maximum odd mode gaps for dimer cylinder and dimer particle bases . . . . .	116
5.3	Schematics of dimer structures at $r_l$ value of 0.35 . . . . .	118
5.4	Dielectric filling fraction comparison for cylinder morphology and dimer morphology . . . . .	120
5.5	Maximum even mode gaps for dimer cylinder and dimer particle bases . . . . .	121
5.6	Contour plots of largest even gaps for dimer cylinder bases . . . . .	123
5.7	Contour plots of maximum polarization independent gaps in dimer cylinder bases . . . . .	124
5.8	Gap maps for asymmetric dimer cylinder structures with $r_l$ values of 0.35 . . . . .	126
5.9	Gap maps for dimer cylinder structures with $r_l$ value of 0.30 . . . . .	127
5.10	Gap maps for dimer cylinder structures with $r_l$ value of 0.40 . . . . .	128
5.11	Minimum dielectric contrasts of odd mode gaps for dimer cylinder and dimer particle bases . . . . .	130
5.12	Minimum dielectric contrasts of even mode gaps for dimer cylinder and dimer particle bases . . . . .	131

5.13	Relative gap width variation with slab height . . . . .	133
5.14	Gap maps as a function of dielectric contrast at varying slab heights . . . .	134
5.15	Displacement field distribution at the $K'$ symmetry point for dimer cylinders . . . . .	135
5.16	Magnetic field distribution at the $K'$ symmetry point for dimer cylinders .	136
5.17	Contour plots of maximum polarization independent gaps for reduced slab height dimer cylinder bases . . . . .	138
5.18	Contour plots of largest even mode gaps for dimer cylinder bases at reduced slab height . . . . .	139
5.19	Contour plots of largest odd mode gaps for dimer cylinder bases at reduced slab height . . . . .	140
5.20	Gap maps for direct dimer cylinder structures at reduced slab height with $r_l$ value of 0.40 . . . . .	141
5.21	Gap maps for inverted dimer cylinder structures at reduced slab height with $r_l$ value of 0.45 . . . . .	143

# CHAPTER 1

## INTRODUCTION

### 1.1 Photonic Crystals

A photonic crystal is a material possessing a periodic spatial variation of dielectric constant. An analogy to electron propagation in semiconductor atomic crystals can be drawn. Many stunning biological examples with regular dielectric variation in one-, two- and three dimensions have been studied (Figure 1.1). Bright coloration in animals, such as the wings of the *Parides sesostris* (the Emerald-patched Cattleheart butterfly) and the scales covering the exoskeleton of the *Lamprocyphus augustus* (a Brazilian weevil), arises from submicron scale structure. Additional examples exist in inorganic systems. The characteristic colors of gem opals similarly arises from the crystalline structure formed by silica spheres.[66, 68] From an engineering perspective, appropriate choices of dielectric material and dielectric thickness results in constructive interference and elimination of a forward-propagating wave.[58] Similar to atomic crystals, photonic crystals can have energy band gaps at which frequencies inside the gap can not propagate in the crystal.[73, 27, 26]

The interest in photonic band gap materials springs from the ability to modify spontaneous emission and confine radiation. Photonic crystals also offer the possibility of such exotic effects as superprism phenomena, self-collimation and negative refraction[49, 11, 60, 7, 31, 32] and slow light with low group velocity at frequencies near the band gap.[3] Numerous applications have been designed utilizing these properties— integrated optical chips; filters; waveguides and resonators; sub-diffraction limit planar lenses; biological sensors; improved efficiency photovoltaic cells; etc.[26, 48, 47, 64, 16, 4, 1]

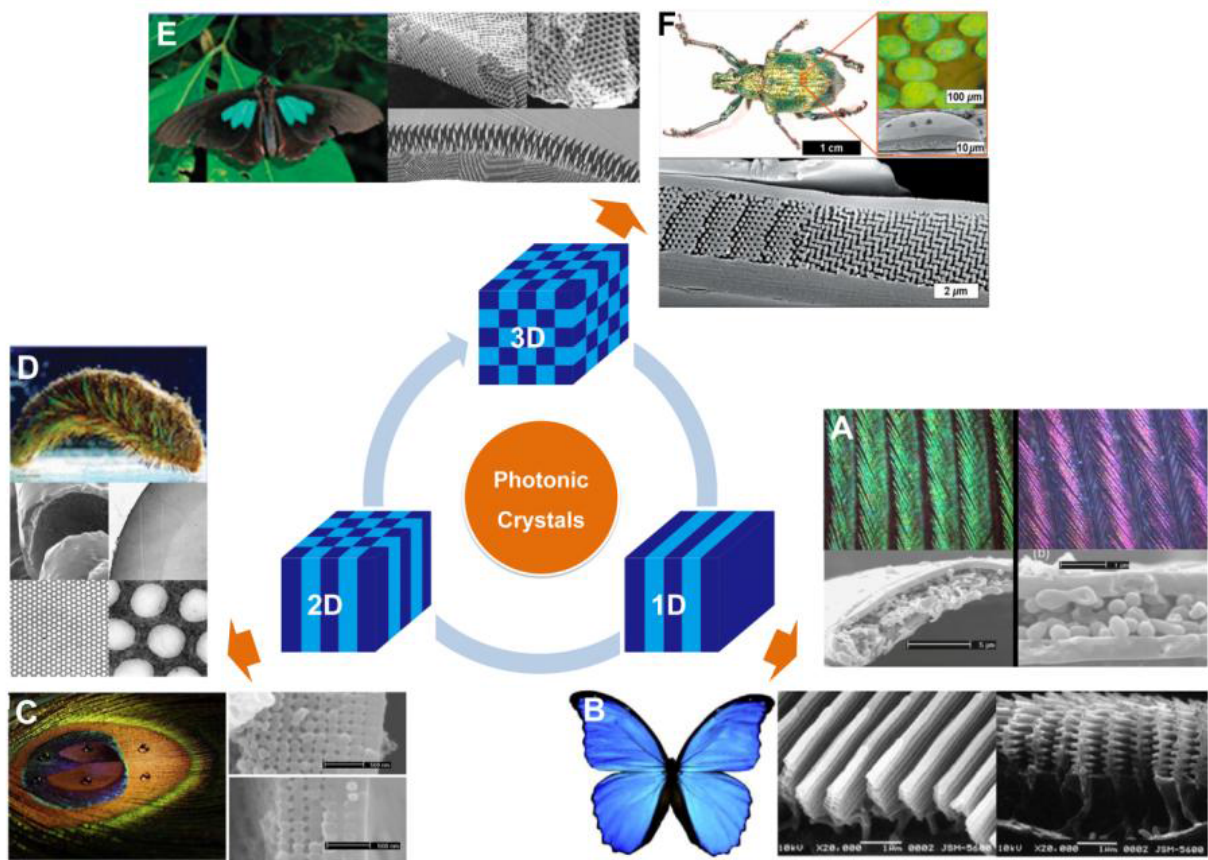


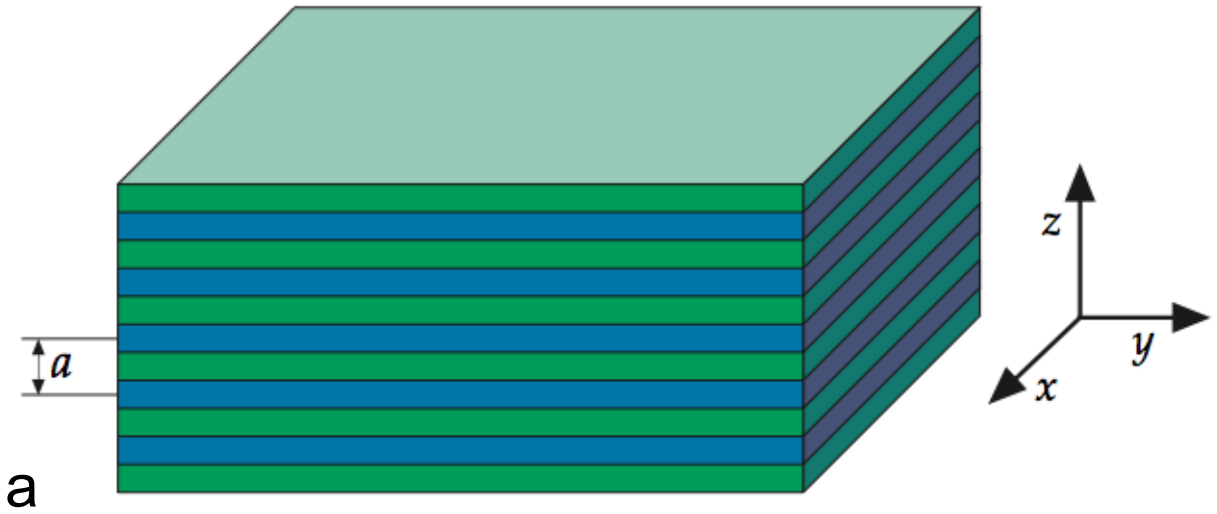
Figure 1.1: Biological examples of photonic crystals with dielectric periodicity in one-, two- and three dimensions.[68]

Figure 1.2a shows an alternating dielectric stack in 1D. A band diagram of a homogeneous material with an artificial periodicity overlaid on it is presented in Figure 1.2b. The band diagram expresses the relationship between the frequency of light in the material to the wavevectors supported (i.e., the dispersion relationship). Along the alternating dielectric axis of the stack, the structure has discrete translational symmetry instead of continuous symmetry. The Fourier transform of the direct structure yields the reciprocal space lattice vectors. The unique reciprocal space wavevectors are collectively known as the first Brillouin zone.

From Bloch's theorem the wave solutions in a periodic potential must be self-replicating with the same periodicity as the structure.[30] Maxwell's equations govern classical electromagnetic interactions with matter. Assuming a material is free of sources (i.e., charges and currents), linear (the dielectric polarization is proportional to the electric field), isotropic (the material permittivity and permeability are scalar), time-harmonic (electric and magnetic fields vary periodically with time), without explicit frequency dependence and the permeability is unity, combining Maxwell's equations with Bloch's theorem yields an eigenvalue problem:[26]

$$\nabla \times \left( \frac{1}{\epsilon(\vec{r})} \nabla \times \vec{H}(\vec{r}) \right) = \left( \frac{\omega}{c} \right)^2 \vec{H}(\vec{r})$$

The field is concentrated in the high dielectric material for the cosine solution and in the low dielectric material for the sine solution. The electromagnetic energy depends on the refractive index and the electric field squared. A mode with the electric field concentrated in the high dielectric has a lower frequency than a mode with the electric field concentrated in the low dielectric, resulting in a gap.[26] Increasing the dielectric contrast, the ratio of the high dielectric constant to the low dielectric constant, increases the frequency range of the gap. In the band diagrams the ordinate is normalized by the spatial period since Maxwell's laws are scale invariant. Band gaps found for a given structure may be tuned to the desired frequency by scaling accordingly.



a

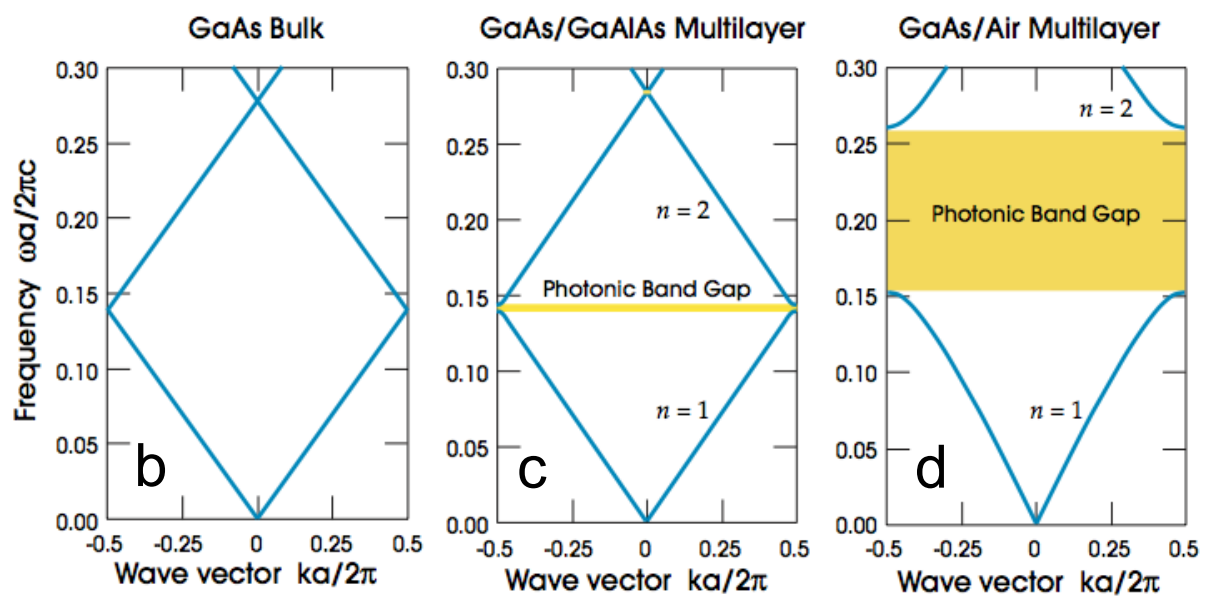


Figure 1.2: 1D photonic crystal with alternating dielectric constant values of a) 13 and 13, b) 13 and 12, c) 13 and 1. [26]

In two-dimensional (2D) lattices, the Brillouin zone is the area in reciprocal space that is closest to the origin and is constructed by finding the envelope of the perpendicular bisectors of the lines drawn between the reciprocal lattice origin and its nearest neighbors. Considering the example of a rectangular lattice, there is a two fold rotation as well as two orthogonal mirror planes. The Brillouin zone may be reduced to a region that, by application of these point group symmetries ( $2mm$ ), reproduces the Brillouin zone. This quadrant is called the irreducible Brillouin zone and its corners, reciprocal space points of high symmetry, are labeled according to convention. Band diagrams present the abscissa as a series of panels based on points of high symmetry in the lattice. Each direction in a crystal (2D or three-dimensional, 3D) can be regarded as a 1D system with its own periodicity. In the 1D system, gaps are found only at the Brillouin zone boundary. Therefore, only the boundaries between the high symmetry points in reciprocal space need be calculated in higher dimension structures.

Photonic crystal applications were conceptualized requiring 3D dielectric periodicity to control light in three dimensions. A few face centered cubic-based structures have been identified.[21, 72, 22, 65, 61] The champion diamond structure has proven elusive due to the lower free energy close-packed face centered cubic structure in spheres, although an experimental diamond lattice was built via nanorobotic placement of individual spheres to confirm the photonic band gap.[17] 3D light confinement can be more readily attained in experiment using planar waveguide techniques.

In photonic crystal slabs, structures with two-dimensional periodicity and finite height, the electromagnetic fields are controlled in-plane through the photonic crystal patterning and out-of-plane via index guiding.[28] The light cone is the lower boundary of the frequencies supported by the bulk background material. This boundary is defined as the wavevector magnitude divided by the refractive index of the cladding or as the lowest

band for a periodically structured cladding. Below the light cone the perpendicular component of the wave vector is imaginary and the light is guided by the slab. Outside of the slab the guided field decays evanescently. Complete band gaps in slabs are determined in the sense that no guided modes exist for the frequency range.

## 1.2 Self-assembly

Theoretical studies suggest more complex structures such as Archimedean tilings (i.e.,  $3^2 \cdot 4 \cdot 3 \cdot 4$  and  $4 \cdot 8^2$ , Schläfli symbols for ‘lady bug’ and ‘bathroom tile’), five-fold and eight-fold symmetric quasicrystals, amorphous diamond and honeycomb lattices of binary sized circular-pores promote gap formation.[69, 15, 71, 62, 43, 18, 9] More complicated structures increases the fabrication challenges. Holographic lithography requires more involved optical set up to generate the interference pattern. Alternative fabrication techniques such as photolithography may be limited by the wavelength resolution; stitching errors and imprecise vertical alignment in large area ( $150 \mu\text{m} \times 150 \mu\text{m}$ ) fabrication using electron beam lithography can occur and heterogeneous materials showed structural damage and deviations from the desired pattern when micromachining using focused ion beam etching. Additionally, all of these methods require more expensive equipment than colloidal self-assembly which lends itself to large-scale arrangements.[39, 16]

For photonic crystals, colloidal self-assembly offers a bottom-up approach where the feature size and basis morphology is inherent in the building block. In the hard potential limit where the particles are not allowed to overlap but otherwise do not interact with each other, ordered phases arise from maximizing the entropy (particle orientation and free volume) of the system. For example, in the spherocylinder system the disordered isotropic fluid undergoes a phase transition to the oriented nematic and smectic phases

at higher concentrations. The more dense states reduces the orientational order of the system, however, the free volume entropy is increased by the reduced excluded volume of the ordered phase.[52]

Spherical particle systems can access a limited range of structures, i.e., the face centered cubic (FCC) crystal has the highest packing density in bulk. Direct FCC crystals have only a partial band gap over a limited range of wave vectors. The inverted structure has a gap between the 8th and 9th bands.[61, 21] However, the gap is sensitive to defects (i.e., closes for particle dispersity greater than 2 % and reduces to gap sizes under 2.5 % with less than 86 % backfilling).[14, 61, 38] When spheres are assembled under physical confinement a hexagonal monolayer assembles at the most restricted height. As the confinement height increases, a corrugated out-of-plane rectangular buckled phase transitions between the hexagonal monolayer and square bilayer. Additional rhombic, prism and hexagonal-close-packed-like phases appear between increased numbers of alternating hexagonal and square particle layers.[56, 54, 46, 41, 57, 40] Monolayer and bilayer crystals feature 2D periodicity and finite height characteristics of slab photonic crystals. However, limited studies have examined the photonic properties, specifically the band gap properties, of structures other than the bulk FCC crystal. Of these works, the focus remained on the hexagonal monolayer of spheres.[67, 50]

The photonic band gap limitations of the FCC crystals prepared from spherical particles prompted the modeling of dimer-based 3D photonic crystals. Theoretical predictions of band gaps between the 2nd and 3rd bands[36, 37] and higher indexed bands[24, 23] inspired the synthesis of non-spherical colloids for photonics. The expanding range of monodisperse colloidal building block shapes that can be used includes ellipsoids; boomerang; square cross; flying saucer; blood cell; w-motif; cubes; cylinders; hex nuts; hexagonal-, square-, triangular-, trapezoidal- and pentagonal prisms; spherocylinders;

dumbbells; asymmetric dimers; and sphere clusters with tetrahedral, octahedral, and square-bipyramidal, etc. geometry.[19, 53, 74, 12, 6, 77, 45, 76, 63, 51, 44, 20, 29]

A rich variety of assembly techniques developed for spherical systems are available for anisotropic colloids.[75, 10, 35, 42, 13, 33] Of particular interest, confinement assembly in a wedge cell enables multiple phases to be studied simultaneously through the continuous evolution of colloidal structure at varying heights. Additionally, incommensurate cell height leads to different packing strategies. A range of self-organization has been demonstrated in thermodynamic simulations of asymmetric dimer and cut sphere particles. Translationally regular center-of-mass structures with uniform or random orientation (i.e., plastic crystal phases) as well as aperiodic crystals (i.e, degenerate crystals) are stable in Monte Carlo simulations.[8, 70, 2] Monolayer plastic crystal, oblique and degenerate crystal phases have been experimentally realized by self-assembly of ‘mushroom caps’ and dimers under physical confinement.[34, 25, 23, 59, 55] With many particle morphologies synthesized at mesoscale dimensions (approximately 100 nm to 2  $\mu\text{m}$ ),[5] finite height mono- and bilayer colloidal crystals offer a diverse range of structures with relatively unexplored photonic band gap properties.

This dissertation investigates 2D and quasi-2D structures self-assembled from anisotropic colloids through physical confinement. Additionally, photonic band gap characterization of ordered mushroom cap and asymmetric dimer shaped colloid arrangements at moderate to high dielectric contrast was performed using photonic crystal ‘slab’ configurations. In chapter two, the mushroom cap-shaped colloidal system and the confinement assembly technique are introduced. Aqueous suspensions of the particles were gravitationally sedimented between the glass walls of a wedge profile confinement cell and were studied with precise spatial and temporal resolution via fast confocal microscopy. Chapter three examines the photonic band gap properties of a buckled

phase found in the mushroom-cap system between the first and second particulate layers of confined colloidal suspensions. Dielectric shaping in three dimensions, consistent with the experimental system, imparted variation to the cross-sectional profile of the slab atypical for lithographic realizations. In chapter four, a centered rectangular lattice with dimer (i.e., interpenetrating sphere) bases, observed in evaporation-assisted (convective assembly) and confinement assembly, was computationally modeled. Photonic band gap characterization was conducted over physically realizable particle morphologies spanning from spheres to lobe-tangent dimers. Chapter five is an extension from the previous chapter and investigates a centered rectangular lattice with dimer cylinder bases. Slab thickness was tuned to overlap even and odd mode gap frequency ranges generating a sizable polarization independent gap.

## REFERENCES

- [1] Kevin A. Arpin, Agustin Mihi, Harley T. Johnson, Alfred J. Baca, John A. Rogers, Jennifer A. Lewis, and Paul V. Braun. Multidimensional architectures for functional optical devices. *Adv. Mater.*, 22(10):1084–1101, February 2010.
- [2] Carlos Avendaño, Chekeshia M. Liddell Watson, and Fernando A. Escobedo. Directed self-assembly of spherical caps via confinement. *Soft Matter*, 9(38):9153, 2013.
- [3] T. Baba. Slow light in photonic crystals. *Nature Photonics*, 2(8):465–473, 2008.
- [4] Shrestha Basu Mallick, Nicholas P. Sergeant, Mukul Agrawal, Jung-Yong Lee, and Peter Peumans. Coherent light trapping in thin-film photovoltaics. *MRS Bull.*, 36(06):453–460, June 2011.
- [5] Mila Boncheva and George M. Whitesides. Making things by self-assembly. *MRS Bulletin-Materials Research Society*, 30(10):736, 2005.
- [6] Julie A. Champion, Yogesh K. Katare, and Samir Mitragotri. Particle shape: A new design parameter for micro- and nanoscale drug delivery carriers. *J. Controlled Release*, 121(1-2):3–9, August 2007.
- [7] Ertugrul Cubukcu, Koray Aydin, Ekmel Ozbay, Stavroula Foteinopoulou, and Costas M. Soukoulis. Electromagnetic waves: Negative refraction by photonic crystals. *Nature*, 423(6940):604–605, June 2003.
- [8] Matthew Dennison, Kristina Milinković, and Marjolein Dijkstra. Phase diagram of hard snowman-shaped particles. *J. Chem. Phys.*, 137(4):044507, 2012.
- [9] Keiichi Edagawa, Satoshi Kanoko, and Masaya Notomi. Photonic amorphous diamond structure with a 3D photonic band gap. *Phys. Rev. Lett.*, 100(1):013901, January 2008.
- [10] Akira Emoto, Emi Uchida, and Takashi Fukuda. Fabrication and optical properties of binary colloidal crystal monolayers consisting of micro- and nano-polystyrene spheres. *Colloids Surf., A*, 396:189–194, February 2012.
- [11] S. Foteinopoulou and C. Soukoulis. Electromagnetic wave propagation in two-dimensional photonic crystals: A study of anomalous refractive effects. *Phys. Rev. B*, 72(16), October 2005.

- [12] E. Y. K. Fung, K. Muangnapoh, and C. M. L. Watson. Anisotropic photonic crystal building blocks: colloids tuned from mushroom-caps to dimers. *J. Mater. Chem.*, 22:10507–10513, 2012.
- [13] Eric M. Furst. Directed self-assembly. *Soft Matter*, 9(38):9039, 2013.
- [14] D. Gaillot, T. Yamashita, and C. Summers. Photonic band gaps in highly conformal inverse-opal based photonic crystals. *Phys. Rev. B*, 72(20), November 2005.
- [15] R. Gajić, D. Jovanović, K. Hingerl, R. Meisels, and F. Kuchar. 2D photonic crystals on the archimedean lattices (tribute to johannes kepler (1571-1630)). *Opt. Mater.*, 30(7):1065–1069, March 2008.
- [16] Juan F. Galisteo-López, Marta Ibisate, Riccardo Sapienza, Luis S. Froufe-Pérez, Álvaro Blanco, and Cefe López. Self-assembled photonic structures. *Adv. Mater.*, 23(1):30–69, January 2011.
- [17] Florencio García-Santamaría, Hideki T. Miyazaki, Alfonso Urquía, Marta Ibisate, Manuel Belmonte, Norio Shinya, Francisco Meseguer, and Cefe López. Nanorobotic manipulation of microspheres for on-chip diamond architectures. *Adv. Mater.*, 14(16):1144, 2002.
- [18] Masashi Hase, Mitsuru Egashira, Norio Shinya, Hiroshi Miyazaki, Kenji M. Kojima, and Shin-ichi Uchida. Optical transmission spectra of two-dimensional quasiperiodic photonic crystals based on penrose-tiling and octagonal-tiling systems. *J. Alloys Compd.*, 342(1):455–459, 2002.
- [19] Kevin P. Herlihy, Janine Nunes, and Joseph M. DeSimone. Electrically driven alignment and crystallization of unique anisotropic polymer particles. *Langmuir*, 24(16):8421–8426, August 2008.
- [20] C.J. Hernandez and T.G. Mason. Colloidal alphabet soup: Monodisperse dispersions of shape-designed LithoParticles. *J. Phys. Chem. C*, 111(12):4477–4480, March 2007.
- [21] K. Ho, C. Chan, and C. Soukoulis. Existence of a photonic gap in periodic dielectric structures. *Phys. Rev. Lett.*, 65(25):3152–3155, December 1990.
- [22] K. M. Ho, C. T. Chan, C. M. Soukoulis, R. Biswas, and M. Sigalas. Photonic band gaps in three dimensions: New layer-by-layer periodic structures. *Solid State Commun.*, 89(5):413 – 416, 1994.
- [23] I. D. Hosein, M. Ghebrebrhan, J. D. Joannopoulos, and C. M. Liddell. Dimer shape

- anisotropy: a nonspherical colloidal approach to omnidirectional photonic band gaps. *Langmuir*, 26(3):2151–2159, 2009.
- [24] I. D. Hosein, S. H. Lee, and C. M. Liddell. Dimer-based three-dimensional photonic crystals. *Adv. Funct. Mater.*, 20(18):3085–3091, 2010.
- [25] I. D. Hosein and C. M. Liddell. Convectively assembled nonspherical mushroom cap-based colloidal crystals. *Langmuir*, 23(17):8810–8814, 2007.
- [26] J. D. Joannopoulos, Steven G. Johnson, Joshua N. Winn, and Robert D. Meade. *Photonic Crystals: Molding the Flow of Light*. Princeton University Press, Princeton, 2nd edition, 2008.
- [27] Sajeev John. Strong localization of photons in certain disordered dielectric superlattices. *Phys. Rev. Lett.*, 58(23):2486–2489, June 1987.
- [28] Steven G. Johnson, Shanhui Fan, Pierre R. Villeneuve, J. D. Joannopoulos, and L. A. Kolodziejski. Guided modes in photonic crystal slabs. *Phys. Rev. B*, 60(8):5751–5758, August 1999.
- [29] Jin-Woong Kim and Kyung-Do Suh. Monodisperse polymer particles synthesized by seeded polymerization techniques. *J. Ind. Eng. Chem.*, 14(1):1 – 9, 2008.
- [30] Charles Kittel. *Introduction to solid state physics*. Wiley, Hoboken, NJ, 8th edition, 2005.
- [31] Hideo Kosaka, Takayuki Kawashima, Akihisa Tomita, Masaya Notomi, Toshiaki Tamamura, Takashi Sato, and Shojiro Kawakami. Superprism phenomena in photonic crystals. *Phys. Rev. B*, 58(16):R10096–R10099, October 1998.
- [32] Hideo Kosaka, Takayuki Kawashima, Akihisa Tomita, Masaya Notomi, Toshiaki Tamamura, Takashi Sato, and Shojiro Kawakami. Self-collimating phenomena in photonic crystals. *Appl. Phys. Lett.*, 74(9):1212, 1999.
- [33] S. H. Lee, S. J. Gerbode, B. S. John, A. K. Wolfgang, F. A. Escobedo, I. Cohen, and C. M. Liddell. Synthesis and assembly of nonspherical hollow silica colloids under confinement. *J. Mater. Chem.*, 18(41):4912–4916, 2008.
- [34] Stephanie H Lee, Esther Y. Fung, E. K. Riley, and C. M. Liddell. Asymmetric colloidal dimers under quasi-2D confinement. *Langmuir*, 25(13):7193–7195, 2009.

- [35] Mirjam E. Leunissen, Christina G. Christova, Antti-Pekka Hynninen, C. Patrick Royall, Andrew I. Campbell, Arnout Imhof, Marjolein Dijkstra, René van Roij, and Alfons van Blaaderen. Ionic colloidal crystals of oppositely charged particles. *Nature*, 437(7056):235–240, September 2005.
- [36] Zhi-Yuan Li, Jian Wang, and Ben-Yuan Gu. Creation of partial band gaps in anisotropic photonic-band-gap structures. *Phys. Rev. B*, 58(7):3721, 1998.
- [37] Zhi-Yuan Li, Jian Wang, and Ben-Yuan Gu. Full band gap in fcc and bcc photonic band gaps structure: Non-Spherical atom. *J. Phys. Soc. Jpn.*, 67(9):3288–3291, 1998.
- [38] Zhi-Yuan Li and Zhao-Qing Zhang. Fragility of photonic band gaps in inverse-opal photonic crystals. *Phys. Rev. B*, 62(3):1516, 2000.
- [39] C. López. Materials aspects of photonic crystals. *Adv. Mater.*, 15(20):1679–1704, 2003.
- [40] H Löwen. Twenty years of confined colloids: from confinement-induced freezing to giant breathing. *Journal of Physics: Condensed Matter*, 21(47):474203, November 2009.
- [41] H. Löwen and M. Schmidt. Freezing in confined suspensions. *Optical Methods and Physics of Colloidal Dispersions*, pages 81–89, 1997.
- [42] Simon O. Lumsdon, Eric W. Kaler, and Orlin D. Velev. Two-dimensional crystallization of microspheres by a coplanar AC electric field. *Langmuir*, 20(6):2108–2116, March 2004.
- [43] H. Men, N. C. Nguyen, R. M. Freund, K. M. Lim, P. A. Parrilo, and J. Peraire. Design of photonic crystals with multiple and combined band gaps. *Phys. Rev. E*, 83(4):046703, April 2011.
- [44] Eric B. Mock and Charles F. Zukoski. Determination of static microstructure of dilute and concentrated suspensions of anisotropic particles by ultra-small-angle x-ray scattering. *Langmuir*, 23(17):8760–8771, August 2007.
- [45] Ali Mohraz and Michael J. Solomon. Direct visualization of colloidal rod assembly by confocal microscopy. *Langmuir*, 21(12):5298–5306, June 2005.
- [46] Stephan Nesper, Clemens Bechinger, Paul Leiderer, and Thomas Palberg. Finite-size effects on the closest packing of hard spheres. *Phys. Rev. Lett.*, 79(12):2348–2351, 1997.
- [47] Susumu Noda. Recent progresses and future prospects of two- and three-

- dimensional photonic crystals. *J. Lightwave Technol.*, 24(12):4554–4567, December 2006.
- [48] Mikhail A. Noginov, Graeme Dewar, Martin W. McCall, and Nikolay I. Zheludev, editors. *Tutorials in Complex Photonic Media*, volume PM194. SPIE Press, Bellingham, Wash, 2009.
- [49] M. Notomi. Theory of light propagation in strongly modulated photonic crystals: Refractionlike behavior in the vicinity of the photonic band gap. *Phys. Rev. B*, 62(16):10696–10705, October 2000.
- [50] K. Ohtaka, Y. Suda, S. Nagano, T. Ueta, A. Imada, T. Koda, J. S. Bae, K. Mizuno, S. Yano, and Y. Segawa. Photonic band effects in a two-dimensional array of dielectric spheres in the millimeter-wave region. *Phys. Rev. B*, 61(8):5267, 2000.
- [51] Masayoshi Okubo and Hideto Minami. Production of micron-sized monodispersed anomalous polymer particles having red blood corpuscle shape. *Macromol. Symp.*, 150(1):201–210, February 2000.
- [52] Lars Onsager. The effects of shape on the interaction of colloidal particles. *Annals of the New York Academy of Sciences*, 51(4):627–659, May 1949.
- [53] Priyadarshi Panda, Kai P. Yuet, T. Alan Hatton, and Patrick S. Doyle. Tuning curvature in flow lithography: A new class of Concave/Convex particles. *Langmuir*, 25(10):5986–5992, May 2009.
- [54] B. Pansu, Pi. Pieranski, and Pa. Pieranski. Structures of thin layers of hard spheres : high pressure limit. *J. Phys. (Paris)*, 45(2):331–339, 1984.
- [55] Jin-Gyu Park, Jason D. Forster, and Eric R. Dufresne. High-yield synthesis of monodisperse dumbbell-shaped polymer nanoparticles. *J. Am. Chem. Soc.*, 132(17):5960–5961, May 2010.
- [56] Pawel Pieranski, L. Strzelecki, and B. Pansu. Thin colloidal crystals. *Phys. Rev. Lett.*, 50(12):900, 1983.
- [57] F. Ramiro-Manzano, E. Bonet, I. Rodriguez, and F. Meseguer. Layering transitions in confined colloidal crystals: The hcp-like phase. *Phys. Rev. E*, 76(5):050401R, November 2007.
- [58] Lord Rayleigh. XXVI. on the remarkable phenomenon of crystalline reflexion de-

- scribed by prof. stokes. *Philosophical Magazine Series 5*, 26(160):256–265, September 1888.
- [59] E. K. Riley and C. M. Liddell. Confinement-controlled self assembly of colloids with simultaneous isotropic and anisotropic cross-section. *Langmuir*, 26(14):11648–11656, 2010.
- [60] C. M. Soukoulis, M. Kafesaki, and E. N. Economou. Negative-index materials: New frontiers in optics. *Adv. Mater.*, 18(15):1941–1952, August 2006.
- [61] H. S. Sözüer, J. W. Haus, and Ramarao Inguva. Photonic bands: Convergence problems with the plane-wave method. *Phys. Rev. B*, 45(24):13962, 1992.
- [62] Sei-ichi Takayama, Hitoshi Kitagawa, Yoshinori Tanaka, Takashi Asano, and Susumu Noda. Experimental demonstration of complete photonic band gap in two-dimensional photonic crystal slabs. *Appl. Phys. Lett.*, 87(6):061107, 2005.
- [63] Zhenquan Tan, Akito Masuhara, Hitoshi Kasai, Hachiro Nakanishi, and Hidetoshi Oikawa. Multibranched c 60 Micro/Nanocrystals fabricated by reprecipitation method. *Jpn. J. Appl. Phys.*, 47(2):1426–1428, February 2008.
- [64] Daniela Threm, Yousef Nazirizadeh, and Martina Gerken. Photonic crystal biosensors towards on-chip integration. *Journal of Biophotonics*, 5(8-9):601–616, August 2012.
- [65] Ovidiu Toader and Sajeew John. Proposed square spiral microfabrication architecture for large three-dimensional photonic band gap crystals. *Science*, 292(5519):1133–1135, May 2001.
- [66] Pete Vukusic and J. Roy Sambles. Photonic structures in biology. *Nature*, 424(6950):852–855, August 2003.
- [67] Kevin Vynck, David Cassagne, and Emmanuel Centeno. Superlattice for photonic band gap opening in monolayers of dielectric spheres. *Opt. Express*, 14:6668–6674, 2006.
- [68] Hui Wang and Ke-Qin Zhang. Photonic crystal structures with tunable structure color as colorimetric sensors. *Sensors*, 13(4):4192–4213, March 2013.
- [69] Feng Wen, Sylvain David, Xavier Checoury, Moustafa El Kurdi, and Philippe Boucaud. Two-dimensional photonic crystals with large complete photonic band gaps in both TE and TM polarizations. *Opt. Express*, 16(16):12278–12289, 2008.

- [70] K. Wojciechowski. Monte carlo simulations of highly anisotropic two-dimensional hard dumbbell-shaped molecules: Nonperiodic phase between fluid and dense solid. *Phys. Rev. B*, 46(1):26–39, July 1992.
- [71] Y. Xia, B. Gates, and Z.-Y. Li. Self-assembly approaches to three-dimensional photonic crystals. *Adv. Mater.*, 13(6):409–413, March 2001.
- [72] E. Yablonovitch et al. Photonic band-gap structures. *J. Opt. Soc. Am. B: Opt. Phys.*, 10:283–283, 1993.
- [73] Eli Yablonovitch. Inhibited spontaneous emission in solid-state physics and electronics. *Phys. Rev. Lett.*, 58(20):2059–2062, May 1987.
- [74] Seung-Man Yang, Shin-Hyun Kim, Jong-Min Lim, and Gi-Ra Yi. Synthesis and assembly of structured colloidal particles. *J. Mater. Chem.*, 18(19):2177, 2008.
- [75] Xiaozhou Ye and Limin Qi. Two-dimensionally patterned nanostructures based on monolayer colloidal crystals: Controllable fabrication, assembly, and applications. *Nano Today*, 6(6):608–631, December 2011.
- [76] G.-R. Yi, V. N. Manoharan, E. Michel, M. T. Elsesser, S.-M. Yang, and D. J. Pine. Colloidal clusters of silica or polymer microspheres. *Adv. Mater.*, 16(14):1204–1208, July 2004.
- [77] Y. Yin and Y. Xia. Self-assembly of monodispersed spherical colloids into complex aggregates with well-defined sizes, shapes, and structures. *Adv. Mater.*, 13(4):267–271, February 2001.

CHAPTER 2

CONFINEMENT-CONTROLLED SELF ASSEMBLY OF COLLOIDS WITH  
SIMULTANEOUS ISOTROPIC & ANISOTROPIC CROSS-SECTION\*

## 2.1 Abstract

The phase behavior of building blocks with mushroom cap-shaped particle morphology is explored under 2D and quasi-2D confinement conditions. Fast confocal microscopy imaging of the particles sedimented in a wedge cell reveals a range of mono- and bilayer structures partially directed by the isotropic and anisotropic profiles of the particle geometry. The sequence of phases tracked with increasing confinement height includes those reported in spheres, in addition to the more complex rotator and orientation-dependent phases observed for a class of short rod-like colloids. In the later case, the major particle axis reorients with respect to the substrate. Closest packing considerations provide rationale for the observed  $1\Delta$  (hexagonal)- $1Buckled-1Sides$  (rotator)- $2\Box$  (square)- $2\Delta$  (hexagonal)- $2Sides$  (rotator) structural transitions with height.

---

\*Originally published as: Erin K. Riley and Chekesha M. Liddell, "Confinement-controlled self assembly of colloids with simultaneous isotropic and anisotropic cross-section," *Langmuir*, **26**, 11648 (2010). Reprinted by permission of the American Chemical Society, <http://pubs.acs.org/doi/abs/10.1021/la100361y>.

## 2.2 Introduction

The promise of transformative technological effects that include negative refraction,[48, 9, 44, 64, 37, 11] superprism,[31, 50] self-collimation,[32] ultralow-loss waveguiding,[2] sensing with minuscule detection limits (via dramatic electromagnetic field enhancement),[63] and inhibited spontaneous emission have fueled the search for structures with large, stable photonic band gaps (PBGs) and tailored dispersion properties. A methodology with great appeal is to specify an ideal optical property (i.e., a large PBG) and then extract the necessary structure.[4, 16] However, the inverse problem is often more difficult than solving the forward case, for which current algorithms and computational power yield exact and efficient solutions.[62] Empirical “guess and check” techniques guided by principles such as symmetry reduction, connectivity of dielectric, and atomic structure analogy uncovered structures possessing PBGs, including the sphere-based diamond,[61, 23, 6] woodpile,[24] square spiral,[58] A7 geometries[7] and the more easily fabricated 2D triangular or square pillar structures. Alternatively, rational material design produced the level-set mathematical approach[38] and genetic algorithms[56, 51, 53] for investigating PBG forming potential. Desired structures must also be physically realized using current processes such as conventional and holographic lithography or self-assembly,[38, 60] further limiting the viable structures.

Recently, unconventional nonspherical colloidal particles (boomerangs, square crosses, hexagonal prisms, UFO shapes, red blood corpuscle shapes, w-motifs, ellipsoids, cylinders, spherocylinders, asymmetric dimers, etc.)[65, 57, 46, 5, 41, 40, 20, 21, 30] have been manufactured with low size dispersity in large quantity. In particular, dimer and tetrahedral colloidal particles are thought to be likely candidates for producing diamond-analogue structures.[43] Simulations of bulk face-centered cubic tangent dimers showed full band gaps between the 2 – 3 (second and third) and 8 – 9 (eighth and ninth) bands

for both direct and inverted structures as a function of the degree of lobe asymmetry and lobe fusion. A 5 – 6 band gap was also determined for the direct case with suitable structural parameters.[25] In addition, one-dimensional aperiodic arrangements based on simple mathematical progressions,[17] fractal structures,[28, 10, 22] as well as 2D and 3D quasicrystals[8, 66] have been shown to possess photonic band gaps. A richer understanding of how structure relates to optical characteristics such as dispersion relationships and band gaps is necessary to realize materials with the desired optical properties.

The pursuit to determine the possible structures formed by anisotropic particles is foundational for colloidal solutions correlating structure and properties for photonics. Several self-assembly techniques are in use— convective and electrophoretic assembly, sedimentation, spin coating, confinement, to name a few. Among them the controlled height of confinement in a wedge enables the systematic study of diverse phases with ease. The progressive confinement height of spherical particle suspensions results in hexagonal ( $1\Delta$ ) and buckled monolayers ( $1B$ ); square ( $2\Box$ ), rhombic ( $2R$ ), hexagonal ( $2\Delta$ ), prism ( $2P$ ) bilayers; and at sufficient gap sizes, hcp-like and  $n\Box$ ,  $nP$ ,  $n\Delta$  multilayers (where  $n$  is an integer).[49, 47, 54, 42, 52] The  $1B$  phase provides a stable transition mechanism from  $1\Delta$  to  $2\Box$ , in which the hexagonal layer is a precursor to two sublayers with particles' centers of mass separated by a fraction of the confinement height.[49, 42]

While extensive work has focused on spherical building blocks under confinement and in bulk, experimental studies that have examined assembly of nonspherical submicrometer particles are relatively few. Simulations of the crystallization of bowl-shaped particles [ $D/\sigma$  (bowl depth/diameter)] revealed a stable columnar structure with columns of alternating particle orientation as well as herringbone-type columnar arrangements ( $D/\sigma \leq 1/2$ ). At higher aspect ratio, an FCC structure of spheres composed of two hard bowls with opposite orientation was determined ( $D/\sigma \sim 1/2$ ).[15] Also in theory reports,

spherocylinders (spherical end-caps on a cylindrical body) have been predicted to transition from an isotropic phase through a plastic or rotator phase to the crystalline ABC-stacked solid, as density increases in the case of low aspect ratio [ $L/D$  (length/diameter)  $< 0.35$ ] shapes. Higher aspect ratio ( $L/D > 3.5$ ) spherocylinders exhibit liquid crystal smectic-A and nematic phases prior to crystallizing to the ABC-stacked solid. Rod-like spherocylinders ( $L/D > 7$ ) form a hexagonal AAA-stacked crystal before the transition to the more dense ABC-stacked solid.[1] Scattering studies on homonuclear dimers ( $L/D = 0.26$ ) demonstrated a plastic phase in highly concentrated suspension.[40] Related studies using convective assembly of asymmetric dimers with low- and high degree of lobe fusion have shown several distinct 2D phases including oblique, rotator, and hexagonal (major particle axis oriented out-of-plane), for which particle reorientation was attributed to confinement by the sloping meniscus.[26] The suggestion was further supported by the observation of the same sequence for asymmetric dimer structures in a rigid confinement wedge where height increased systematically.[33]

Here, we assemble mushroom cap-shaped particles in a wedge cell by gravitational sedimentation. We find the mushroom caps to adopt a series of high density configurations commensurate with the confinement height in the following sequence: [1] hexagonal monolayer (triangular lattice,  $1\Delta$ ); [2] buckled ( $1B$ ) monolayer in which adjacent particles are promoted or demoted along the  $z$ -height, distorting the hexagonal packing to a rectangular one; [3] rotator crystal on an oblique lattice, where the axis of spherical symmetry reorients parallel rather than perpendicular to the plane of the substrate ( $1sides$ ); [4] bilayer square ( $2\Box$ ) with the lower layer particles centered in the interstitials of the top layer; [5] bilayer hexagonal ( $2\Delta$ ); [6] bilayer rotator crystal ( $2sides$ ). Order parameters and correlation functions were determined as quantitative measures of the phase quality. The ideal density of each phase at the minimum geometrically allowed height was also calculated and used to rationalize the stability range of each structure observed.

The mushroom cap particle geometry has associated projection profiles of anisotropic and isotropic systems. Thus, features of both are apparent in the phase behavior of the mushroom caps and they provide an expanded range of ordered phases over hard spheres or rod-like particles, including dimers.

## **2.3 Experimental Section**

### **2.3.1 Particle Synthesis**

Mushroom cap polystyrene (PS) core particles were purchased from Interfacial Dynamics Corporation (batch 1926, 1). The particles were coated with fluorescently labeled silica, encased in plain silica, and stabilized with poly(vinylpyrrolidone) (PVP, 40 000 MW). To make silica compatible to the PS surface, 204 mg of core particles were tumbled overnight with 9.5 mL absolute ethanol (Pharmco Inc.) and 500  $\mu$ L 3-aminopropyl- triethoxysilane (APS, Aldrich), before collection by centrifugation for the remaining steps. The colloids were coated using a dynalene bath at 30 °C under constant sonication at 11 – 14 W applied with an immersion probe (Sonics & Materials Inc., Model VCX-500). For the typical procedure, PS mushroom caps were added to 94 mL of isopropyl alcohol (Aldrich) and 4 mL of ammonia solution (27 %v/v, Mallinckrodt), with aliquots of a sol-gel precursor injected each hour for a total of three additions. The additions consisted of 15  $\mu$ L rhodamineisothiocyanate dye solution (900  $\mu$ L APS, 250 mg dye, 10 mg absolute ethanol) and 30  $\mu$ L tetraethylorthosilicate (TEOS) each time. The mixture was sonicated overnight and washed via centrifugation and redispersion cycles. For the final coat of nonfluorescently labeled plain silica, a single dose of 75  $\mu$ L TEOS was introduced at the start of the 3 h sonication period in 84 mL of isopropyl alcohol (Aldrich), 12 mL of ammonia solution

(27 %v/v, Mallinckrodt), and 4 mL of deionized water (DI, 18.2 M $\Omega$ , Millipore). This was repeated twice. The particles were washed and treated with PVP by tumbling overnight, prior to the final transfer into DI water.

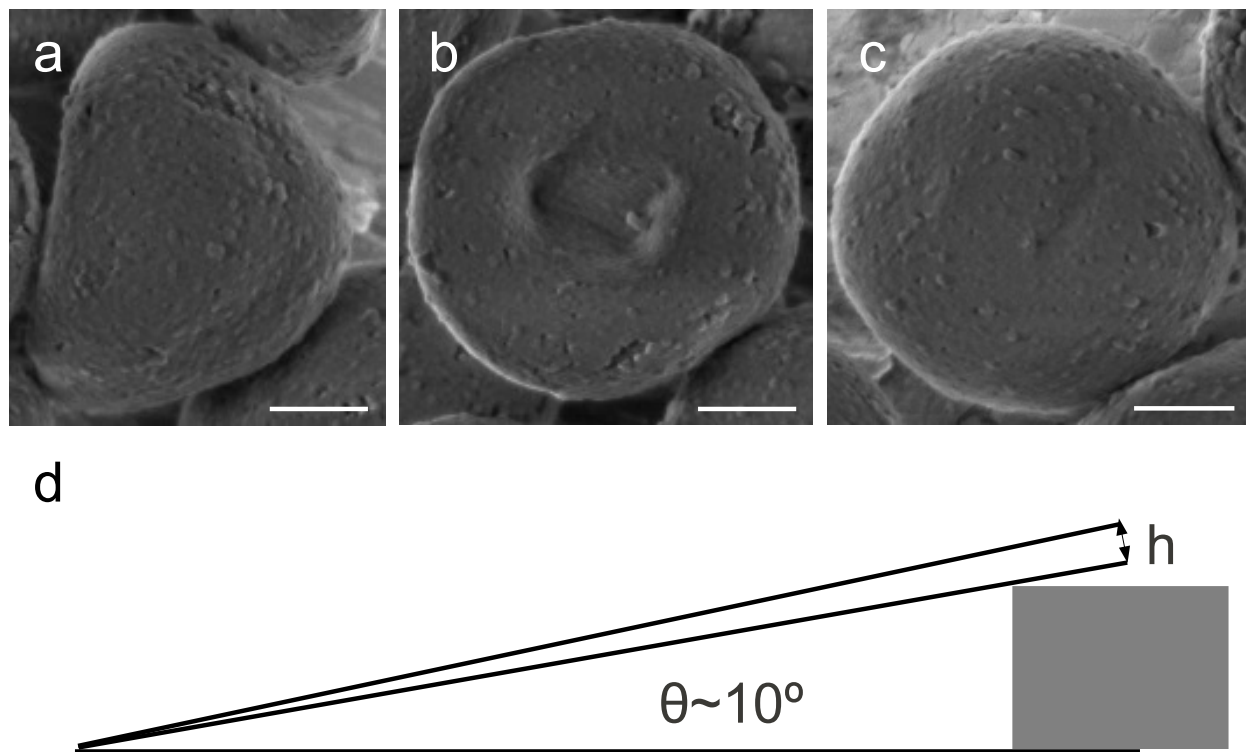


Figure 2.1: (a-c) SEM image perspective views of mushroom cap particles, scale bar is 300 nm. (a) Side, (b) dimple facing up, and (c) dimple facing down orientations are shown. (d) Schematic of confinement cell as positioned during sedimentation.

### 2.3.2 Particle Assembly

The confinement wedge was constructed using three glass surfaces, 22 mm  $\times$  50 mm coverslips (no. 11/2, VWR) and a 1 in  $\times$  3 in microscope slide (VWR). The coverslips were washed in a NaOH, ethanol and DI water solution of pH 14 and thoroughly rinsed in DI water before use. A coverslip was bonded to the support microscope slide using Norland UV adhesive. A spacer array was formed by curing small drops of the UV adhesive and a

second coverslip was placed on top. Pressure was applied to the top coverslip by hand to achieve zero height separation at the tip of the wedge. The cell was sealed along three of four sides with adhesive, leaving one edge propped open for particle injection. Before introducing the sample suspension, the confinement cell was filled with a PVP and DI water solution by pipette to coat the interior surfaces of the coverslips and placed in a low pressure chamber to boil off the excess. The particles were resuspended in  $2.4 \times 10^{-7}$ M PVP solution. Approximately 50  $\mu$ L of the particle suspension was inserted with a pipette and the confinement cell was completely sealed. To sediment the particles into the regions for 2D and quasi 2D observations, the cells were tilted at  $\sim 10^\circ$  for at least 3 days. Confocal data was collected using a Zeiss LSM 5 LIVE confocal microscope.

## 2.4 Results and Discussion

Mushroom cap particles can be synthesized by the dynamic swelling method in which the polymer core-shell particles collapse during seeded polymerization.[46] The depressed surface results from the unbalanced hydrostatic pressure when the evaporation rate of unpolymerized divinybenzene and toluene in the core exceeds the water penetration rate through the hydrophobic shell.[45] The mushroom cap-shaped particles used in this study were 1.2  $\mu$ m in diameter (coefficient of variation,  $CV = 4.2\%$ ). The silica shell thickness of 42 nm (5 nm and dimple planar dimensions of  $\sim 240$  nm (major axis) by  $\sim 130$  nm (minor axis) were determined using transmission and scanning electron microscopy (TEM and SEM). This model shape is of interest in several contexts; for example, as synthetic red blood cells which may concentrate in rouleaux columnar stacks along the flow axes of capillaries,[3, 59] as motifs in microlens arrays,[35] and as bowl-shaped partial fullerene morphs (buckybowls).[39] Most notably for the current work, the shape combines isotropic and anisotropic cross sections in a single particle species.

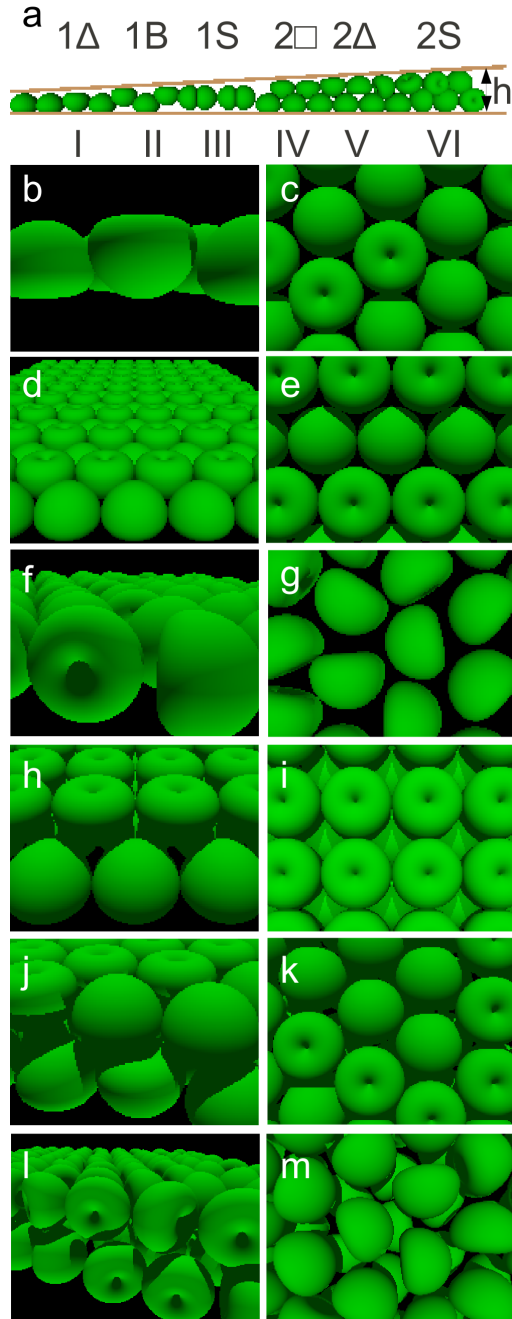


Figure 2.2: (a) Profile of the wedge confinement cell. Side (left) and top (right) views of the idealized mushroom cap phases: (b, c) hexagonal monolayer ( $1\Delta$ ),  $h_{min} = 1.5r$ , (d, e) buckled monolayer ( $1B$ ),  $h_{min} = 1.5r - 2.4r$ , (f, g) sides monolayer ( $1Sides$ ),  $h_{min} = 2r$ , (h, i) square bilayer ( $2\Box$ ),  $h_{min} = 2.4r$ , (j, k) hexagonal bilayer ( $2\Delta$ ),  $h_{min} = 2.6r$ , and (l, m) sides bilayer ( $2Sides$ ),  $h_{min} = 4r$ .

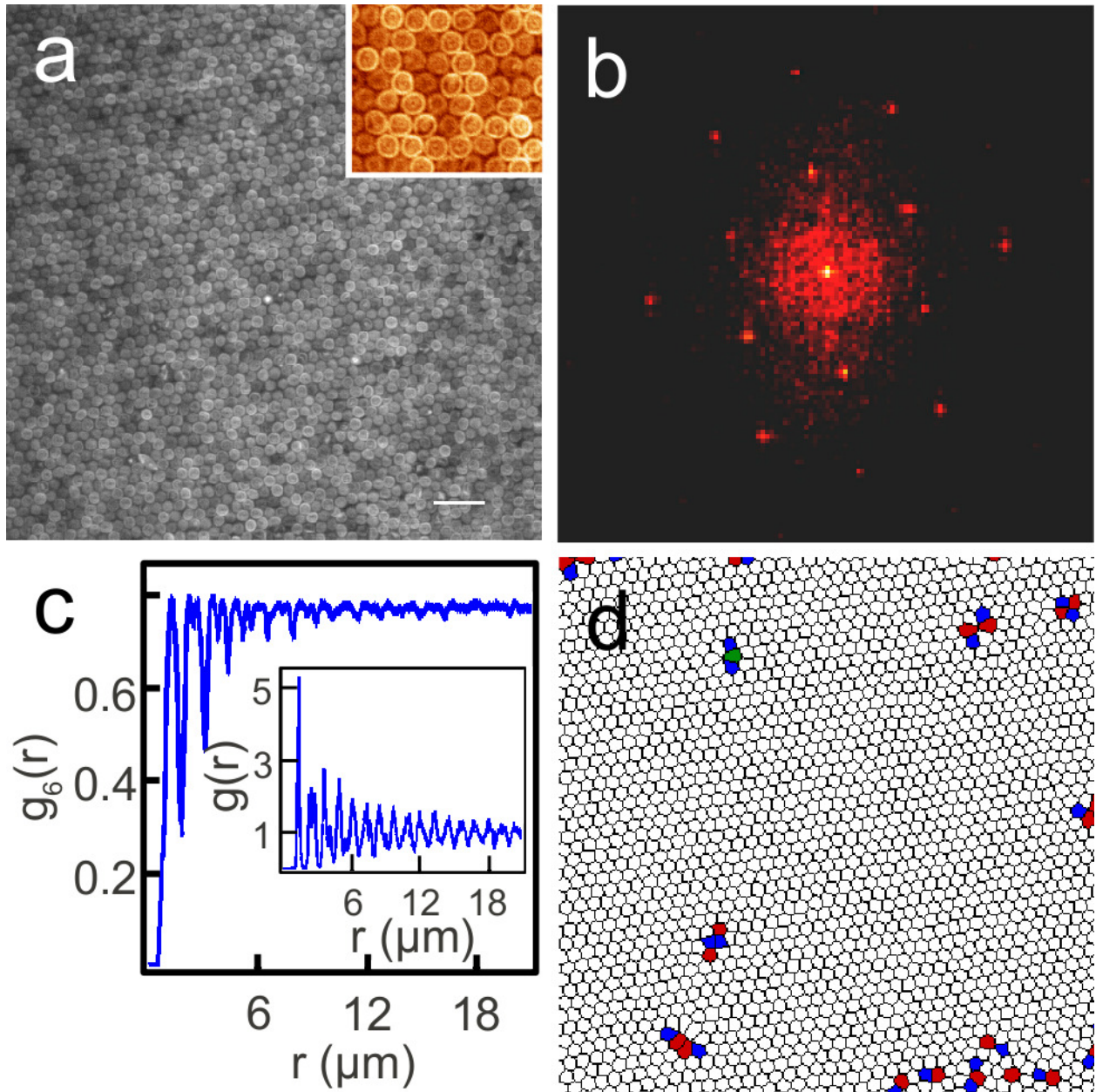


Figure 2.3: (a) Confocal micrograph of  $1\Delta$  region. Scale bar is  $6\ \mu\text{m}$ . Inset is an enlarged display of random dimple-up/dimple-down particle orientations. (b) FFT of a characteristic region in part a indicating 6-fold symmetry. (c) Hexagonal bond-orientation correlation function for  $1\Delta$  phase. The radial distribution function is provided in the inset. (d) Voronoi construction from image in part a. Number of nearest neighbors indicated by color: 4, orange; 5, blue; 6, white; 7, red; 8, green.

Figure 2.2 shows the schematic profile of the wedge with the side and top views of the idealized phases illustrated. Six main regions are denoted that contain well-defined particle configurations. Region I was comprised of randomly mixed dimple-up and dimple-down oriented particles in a monolayer with hexagonal symmetry ( $1\Delta$ ), as seen in Figure 2.2b,c. A fast Fourier transform (FFT) of a representative area from the crystal shows 6-fold symmetry in the well-defined spot pattern (Figure 2.3b). The hexagonal bond-orientational correlation function  $g_6(r)$  is given by  $\langle \psi_6^*(0) \psi_6(r) \rangle$ , where

$$\psi_6(r_i) = \frac{1}{N_b} \sum_{j=0}^{N_b} \exp(i6\theta(r_{ij}))$$

and was computed applying particle tracking algorithms (with manual verification) to the gray-scaled but otherwise unmodified image in Figure 2.3a.[13, 18] The  $g_6(r)$  maintains a value of 1.0 in the case of perfect 6-fold symmetry. The bond-orientational order parameter  $\psi_6 = 0.82$  in Figure 2.3c compares favorably with that of a 2D hexagonal monolayer of spheres ( $\psi_6 = 0.95$ ).[14] The bond-orientational order parameter was calculated over  $N$  total particles by the following expression

$$\psi_6(r_i) = \left| \frac{1}{N} \sum_N \left( \frac{1}{N_b} \sum_{j=0}^{N_b} \exp(i6\theta_k) \right) \right|$$

where  $N_b$  is the number of nearest neighbors, and  $\theta_k$  is the angle formed by an arbitrary reference vector and the nearest neighbor bond vector. The  $g_6(r)$  shows only minor decay over a long spatial range, which suggests the presence of defects and grain boundaries in a roughly  $2900 \mu\text{m}^2$  region, both of which are visible in the Voronoi tessellation (Figure 2.3d) generated from the confocal image. Long-range positional order is further identified by the large coherence length ( $> 15$  peaks) of the pair correlation function,  $g(r)$ , shown in the inset of Figure 2.3c. A hexagonal monolayer phase assembled convectively in prior work was also found to contain particles arbitrarily oriented dimple-up and dimple-down.[27]

The  $1B$  buckled phase occurred in region II (Figure 2.4). The phase exhibits rectangular symmetry with a two-particle unit cell basis as indicated in the inset of Figure 2.4a.

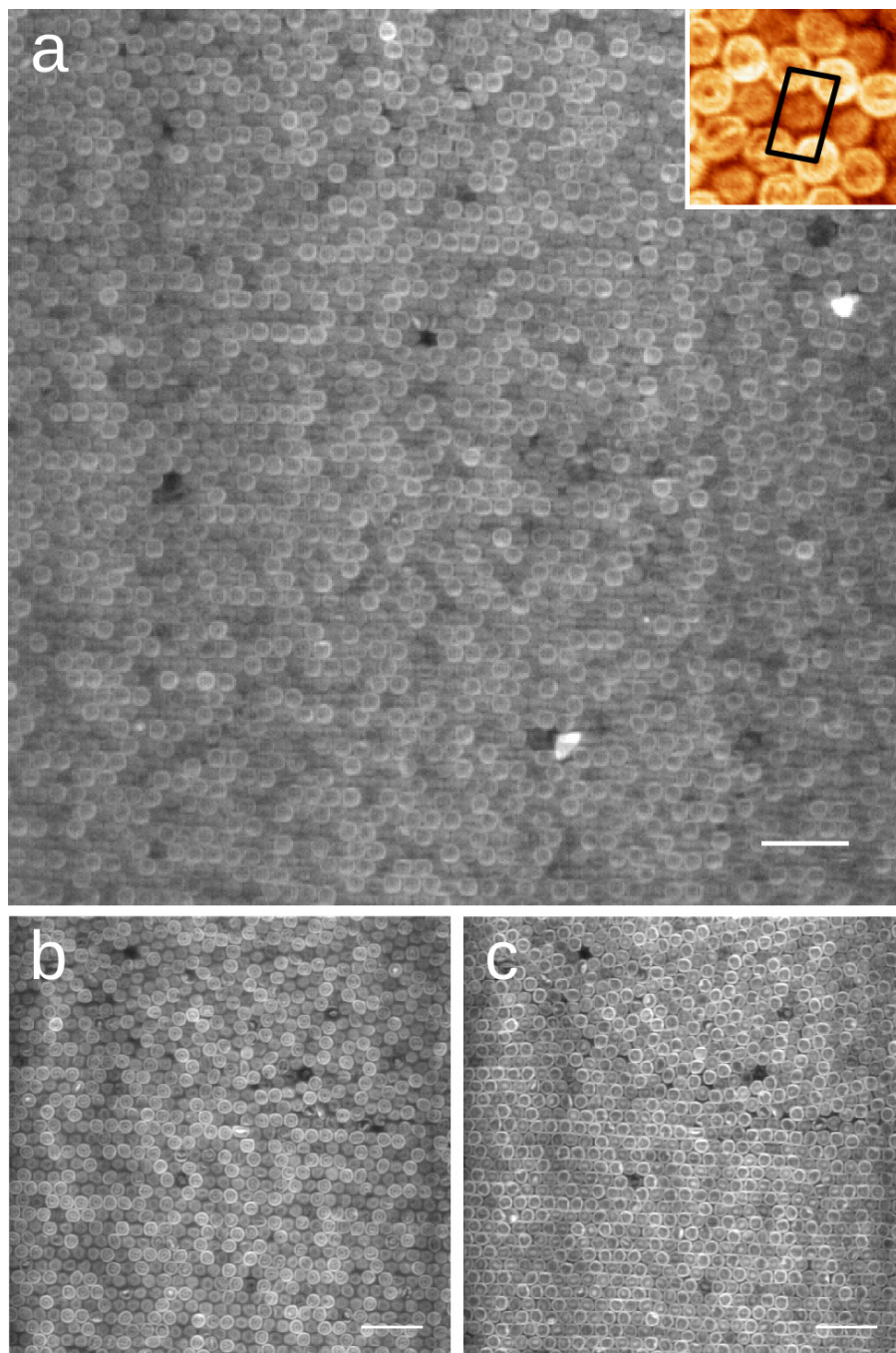


Figure 2.4: a) Confocal micrograph of 1B region with 'straight' and 'zigzag' buckling. Inset is an enlarged view of the rectangular lattice. (b, c) Confocal micrographs with focal planes in (b) the upper sublayer displaying dimple-up particle orientation and (c) between the sublayers where dimple-up particles show a bright ring and dimple-down particles have a bright center. Scale bars are 6  $\mu\text{m}$ .

Figure 2.4b shows a confocal image captured at the z-height of an upper sublayer. In Figure 2.4c, the same crystal region is presented at a focal plane located between the two sublayers. The particles, which in part (b) are clearly seen with the central dimple facing up, are ringed with a bright edge in part (c). As well, the particles which face dimple-down are visible as having a bright center in part (c). The mushroom caps in each sublayer were thus determined to have an orientation preference toward the confining walls in the  $1B$  phase. This is a distinguishing feature as compared to the symmetrical  $1B$  phase in spheres. The ordered bifurcation in orientation allows a higher packing density for a specified height  $h$ . Interestingly the buckled phase of spherical particles has been studied as a parallel to magnetic moments on a lattice where each spin is in one of two states and interacts only with its nearest neighbors according to an antiferromagnetic Ising model. Three main types of buckling were seen in the particle system: [1] raised particles randomly situated among lattice sites (disordered buckling); [2] parallel alternating lines of raised adjacent particles (straight stripes), as shown in the idealized  $1B$  phase Figure 2.2d,e; [3] bent, buckled rows (zigzag stripes).[19, 54] Such variations of frustration-induced structure are apparent in Figure 2.4.

The  $1Sides$  phase was observed in region III and is presented in Figure 2.5a,b. A rotator structure on a centered rectangular or oblique lattice was deduced from the autocorrelation of a representative area in Figure 2.5a inset paired with the apparent rotational freedom of each particle. The region is limited to grains of  $\sim 200$  particles. Only ten major peaks arise in the pair correlation function (Figure 2.5d) due to the incorporation of irregular-sized or shaped particle defects. As the system density increased over time, the character of the particle rotation converted from fully three-dimensional to in-plane and was restricted by the contoured interstices of neighboring particles (see Supporting Information). For a spherical particle system, the  $1B$  phase persisted over the expanse of intermediate heights between  $1\Delta$  and  $2\Box$ .[47, 54] However, the confinement height per-

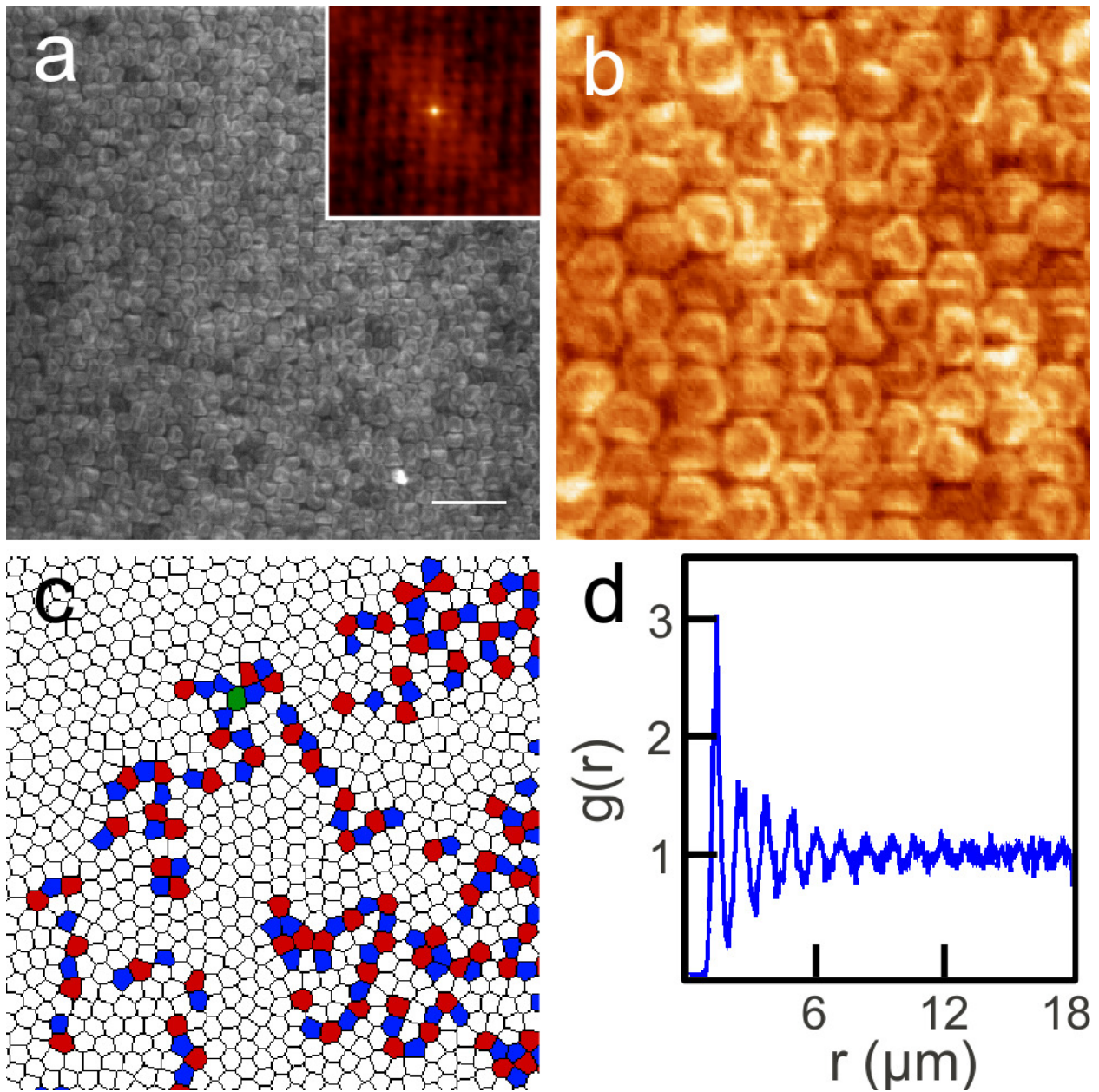


Figure 2.5: (a) Confocal micrograph of  $1Sides$  region. Scale bar is  $6\ \mu\text{m}$ . Inset, autocorrelation function indicating an oblique lattice. (b) Magnified confocal view showing the rotator  $1Sides$  phase. (c) Voronoi construction calculated from part a and (d) radial distribution function,  $g(r)$ .

mitted the particles to rotate out- of-plane onto their sides and interrupted the transition from  $1B$  to  $2\Box$  for the mushroom caps.

Figure 2.6 shows the focal plane progression through the square- packed top layer (a) to the discernible square-packed underlying layer (c) for the  $2\Box$  structure in Region IV. An intermediate focal plane is shown in part b, revealing the bright mushroom “dimple” of the underlying layer centered beneath the interstitial site (white asterisk, Figure 2.6d) formed by four particles in the top layer. The enlarged image of the particles (d inset) exposes the orientation preference of the top layer as dimple-up. The FFT of a representative region (d) shows 4-fold symmetry and equal lattice constants, consistent with square packing. For both the upper and lower layers, the pair correlation functions (f) demonstrate long-range order. The confocal image of the underlying layer is not sharply focused due to increased optical scattering from the polymer cores which are not index matched to the suspension medium. The Voronoi construction in Figure 2.6e emphasizes the distortion caused by large malformed particles. Although the polygons remain predominantly square, higher order polygons indicated by light blue, green, yellow and red color arise due to the slight motion of the particles around the lattice sites. ‘Twisted bond’ (non- $90^\circ$  angle between Wigner-Seitz cells of two adjacent particles) and ‘twisted triangular’ (Wigner-Seitz cells of three adjacent particles intersect at one corner) defects are also visible.[55] The underlying layers of some  $2\Box$  crystals suggest another positioning of the base layer particles, at the site indicated by the black asterisk in the inset of Figure 2.6d.

Region V of the wedge cell contained two layers with hexagonally packed particles, the  $2\Delta$  phase, as shown in Figure 2.7a,b. The FFT of a representative area shows an oblique structure with reciprocal space lattice parameters in the ratio of 1 : 1.03 with an interplanar angle of  $123^\circ$ . The enlarged inset indicates random dimple-up and dimple-down particle orientations similar to the  $1\Delta$  phase. The pair correlation function for the first layer

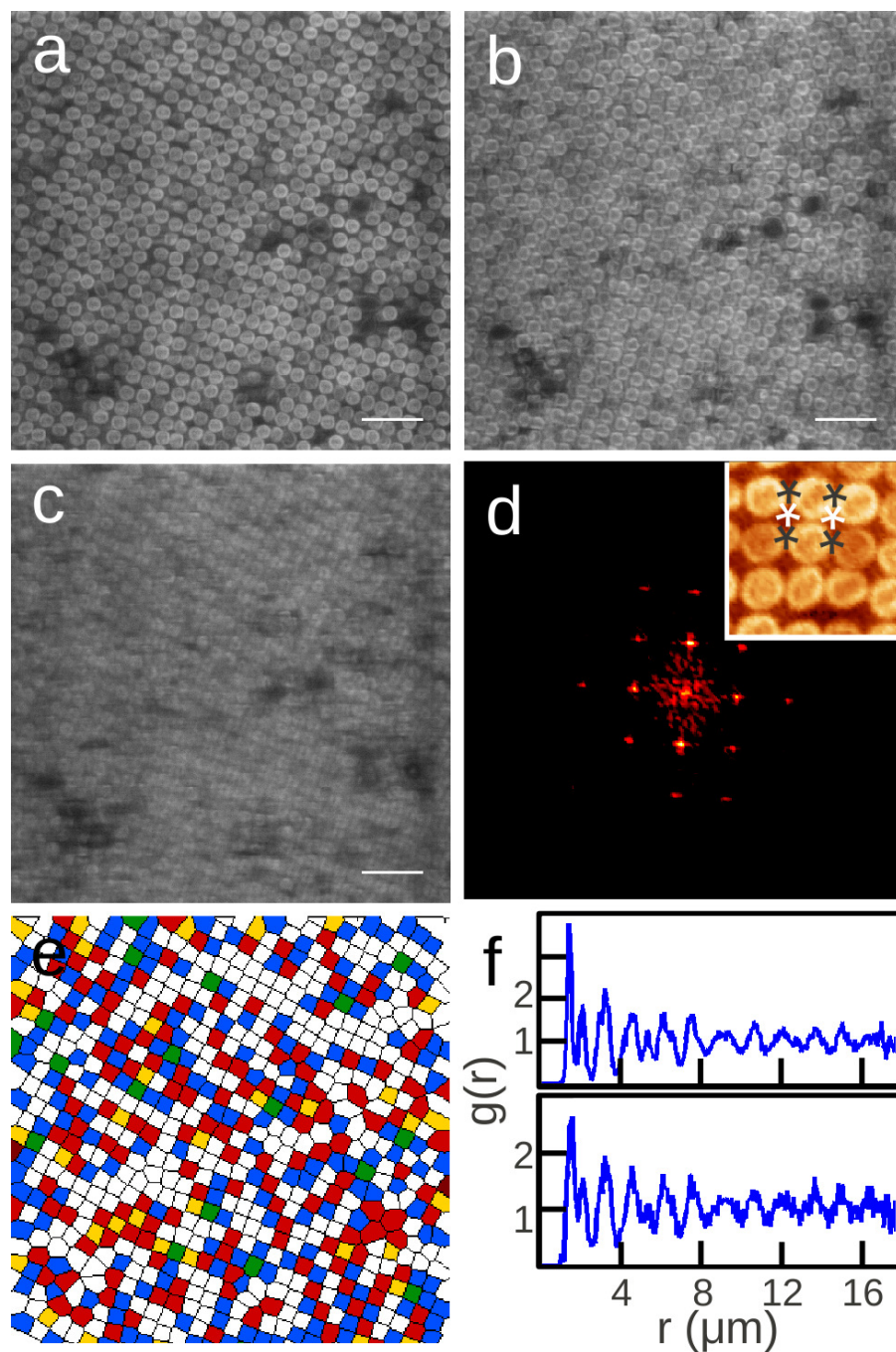


Figure 2.6: (a-c) Confocal micrograph of  $2\sqrt{3}$  region. Scale bars,  $6 \mu\text{m}$ . Focal plane at (a) the upper layer showing the dimple-up particle orientation; (b) between the layers, revealing the bright dimple centered below the upper interstitial site; and (c) at the lower layer. (d) FFT pattern of a representative region of part a showing 4-fold symmetry. Inset, magnified view of the upper layer. (e) Voronoi construction. (f) Radial distribution functions of parts a and c, upper and lower, respectively.

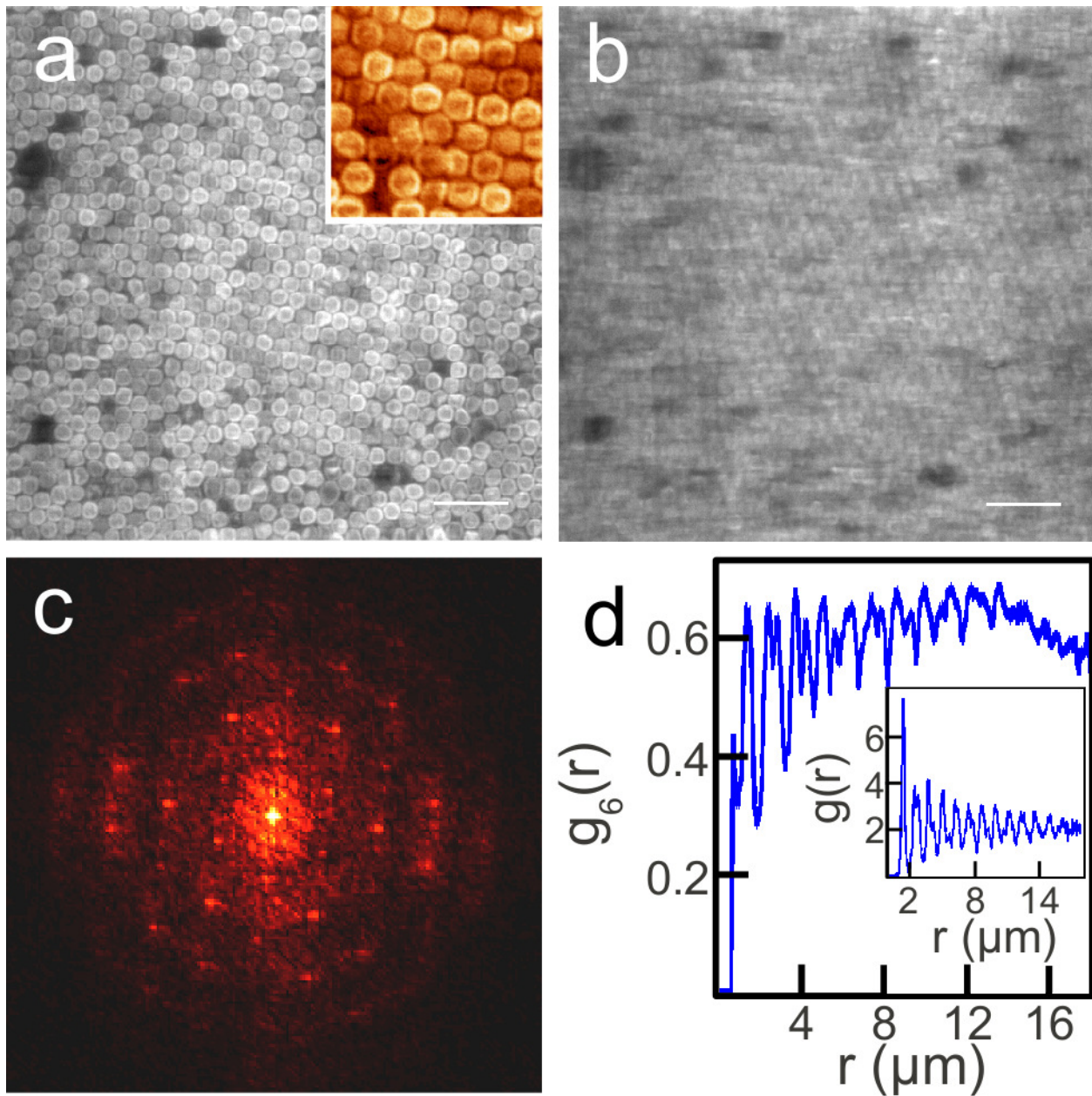


Figure 2.7: (a,b) Confocal micrographs of  $2\Delta$  region. Scale bars,  $6\ \mu\text{m}$ . (a) Focal plane at the upper layer. Inset, enlarged view. (b) Focal plane at the lower layer. (c) FFT pattern of part a. (d) Hexagonal bond-orientational correlation function,  $g_6(r)$ , for the  $2\Delta$  phase. The radial distribution function is inset.

(Figure 2.7d inset) had a coherence length of twelve nearest neighbor distances. The inset hexagonal bond-orientational order parameter indicates some disruption of the ideal 6-fold symmetry, due in part to the ‘mutant’ particles. The value of  $\psi_6$  is lowered to 0.4305 compared to that of the  $1\Delta$  case. While a stable rhombic phase is seen in the spherical particle system on transition to the  $2\Delta$  phase, this was not observed over a meaningful range in the mushroom cap system.[54]

The *2Sides* phase, a bilayer of mushroom caps having major axes out-of-plane, appeared in Region VI. Two structural forms were found, a more open rotator solid (Figure 2.8a,  $\sigma = 0.49$  particles/ $\mu\text{m}^2$ ) and a smectic-type structure of particulate ‘chains’ (Figure 2.8c,  $\sigma = 0.56$  particles/ $\mu\text{m}^2$ ). The layered arrangement is reflected in the periodicity of the  $g_x$  distribution function provided in Supporting Information, Figure 2.9a. The rotator solid exhibits near 6-fold symmetry that is apparent in the FFT in the Figure 2.8b inset. The hexagonal bond-orientational correlation function in Figure 2.8e shows minor decay at large distances, however, and the  $\psi_6$  value of 0.6412 indicates a significant deviation from the values that characterize a high quality hexagonal crystal. The crystal retains long-range order as evidenced by the many peaks of the pair correlation function in the inset of Figure 2.8e. The chaining effect is composed of more closely packed particles in columns. The mushroom caps still have rotational freedom. The smeared linear features of the autocorrelation for this phase (Figure 2.8d) emphasize chaining in contrast to the spot pattern discernible from the autocorrelation for the *2Sides* rotator structure (Figure 2.8b). The *2Sides* phases are more robust than the *1Sides* structure in that they accommodate the large misshapen particles without significant deterioration of the ordering (Figures 2.5c and 2.8f).

The structures formed in regions I-VI as  $h$  increased may be rationalized by considering the competition between the densities of the allowed phases at each separation height

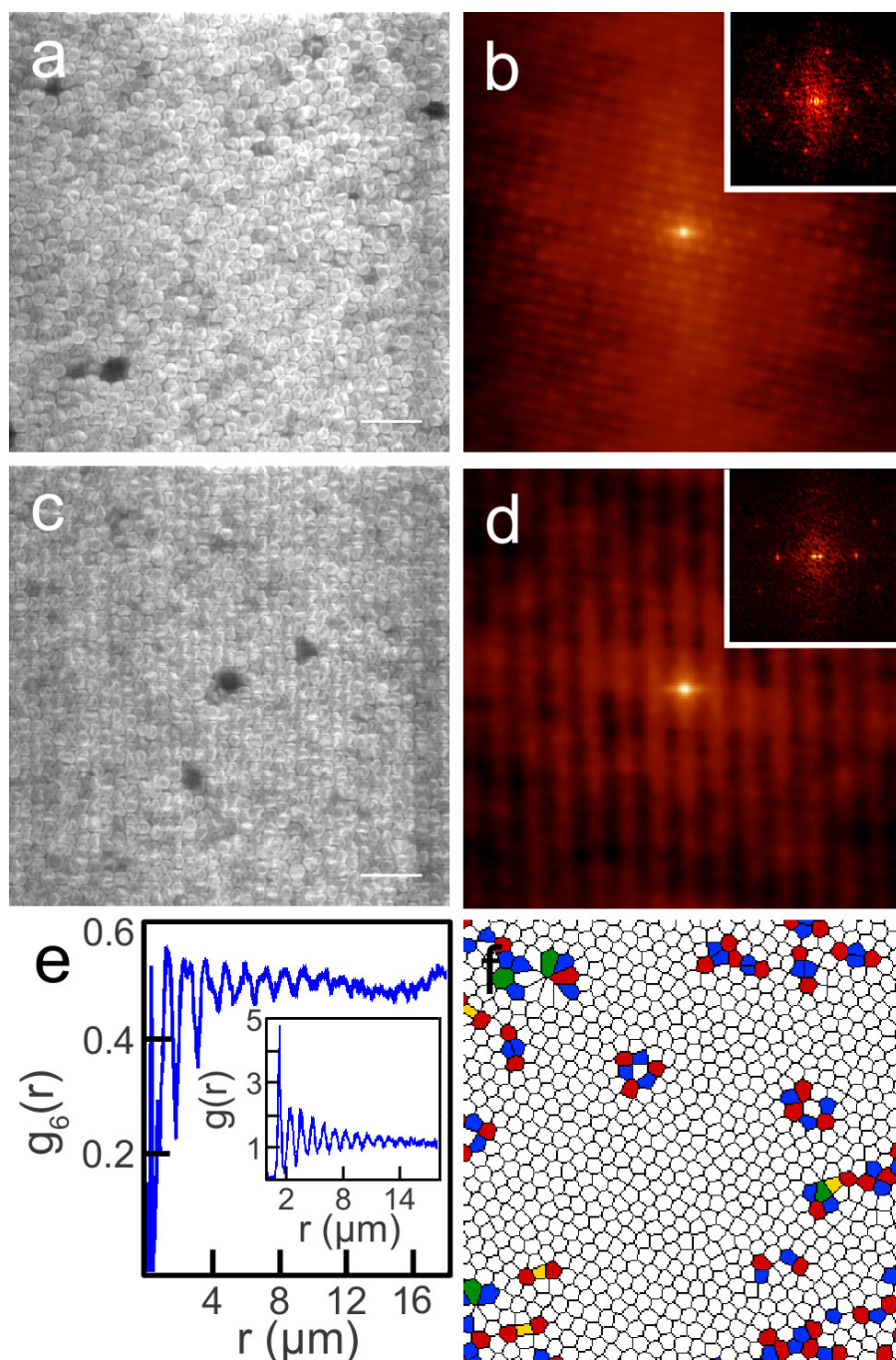


Figure 2.8: (a) Confocal micrograph of *2Sides* oblique rotator region. (b) Autocorrelation function of part a. Inset, FFT pattern of *2Sides* region in part a. (c) Confocal micrograph of *2Sides* "chaining" region. (d) Autocorrelation function of part c. Inset, FFT pattern of *2Sides* region, showing 2-fold symmetry. (e) Hexagonal bond-orientational correlation function,  $g_6(r)$ , of part a with radial distribution function of (a) inset. (f) Voronoi construction of part a. Scale bars,  $6 \mu\text{m}$ . The calculated  $g_6(r)$  and  $g(r)$  for the chained *2Sides* structure in part c are provided in Figure 2.9b.

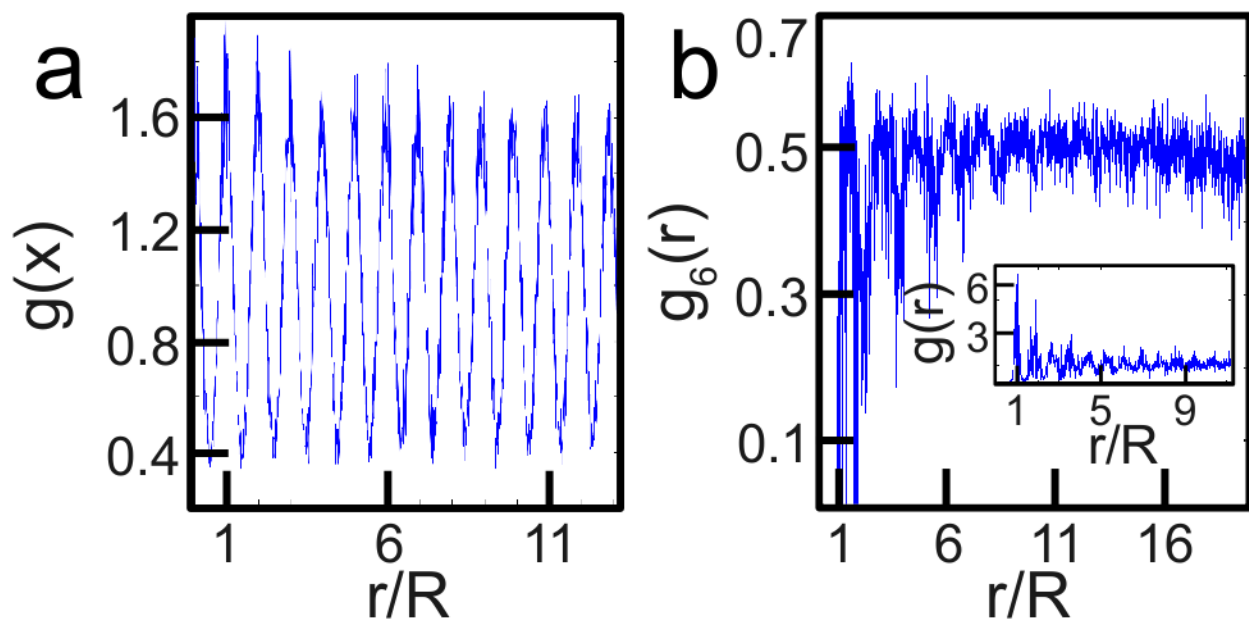


Figure 2.9: a) Distribution function for smectic-like *2Sides* phase. b) Calculated hexagonal bond-orientation correlation function for Figure 2.8c. The radial distribution function is provided in the inset. The  $\psi_6$  value was found to be 0.6581.

(Figure 2.10). The realized phase possesses the highest density at the given  $h$ , satisfying the driving force to maximize the free volume and thus minimize the free energy of the system.[19, 29] We consider a mushroom cap model particle shape formed by a hemisphere of radius  $r$  and a half torus, giving a volume of  $\pi(2/3 + \pi/8)r^3$  per particle. The minimum height ( $h_{min}$ ) geometrically required for each structure and the ideal packing fraction for each phase at  $h_{min}$  are detailed in Table 2.1. The ideal density was calculated from the total volume of particles that occupy area  $A$  of the unit cell (u.c.) divided by  $A \times h_{min}$  for each phase. For example, the density of the  $1\Delta$  arrangement was determined from a primitive rhombic cell ( $a = b = 2r$ ,  $R = 120^\circ$  and  $\beta = 60^\circ$ ) as  $V_{occupied}/V_{u.c.} = [\pi(2/3 + \pi/8)r^3] / [(2\sqrt{3}r^2)(1.5r)] = 0.64$ .

The  $1B$  phase was modeled with a two-particle basis on a rectangular lattice (Figure 2.2d,e), and with the particles in opposite orientations to minimize  $h$ . The assumption was made that particles in each sublayer row remained tangent, based on confocal images. This requirement establishes that  $h$  be related to the spacing between rows ( $2x$ ) in the same sublayer, where  $x = \sqrt{3r^2 - (h - r)^2}$ . The packing density for the buckled phase, therefore, is constant over a range of heights and its density at the minimum height is the same as that of the  $2\Box$  structure (Figure 2.10). An idealized rotator (Figure 2.2f,g) was chosen as a lower bound to approximate the ideal  $1Sides$  phase packing fraction. The mushroom caps were modeled to be centered on the same positions as spheres of radius  $r$  in a hexagonal lattice with  $h_{min} = 2r$ . Full rotation of the particles in the plane is allowed and results in a significantly lower density (0.33) than for the other monolayer phases. Additional ideal oblique phases were modeled in which the mushroom caps have hindered rotation; a primitive oblique lattice ( $a = 2r, b = \sqrt{3}r, R = 125^\circ$ , and  $\beta = 55^\circ$ ) with all particles in a common orientation, and an oblique lattice with a two particle basis ( $a = 2r, b = 3r, R = 120^\circ$ , and  $\beta = 60^\circ$ ) of oppositely oriented mushroom caps. Phase density values of 0.59 and 0.64, respectively, were obtained. The  $2\Box$  assembly was represented (Figure 2.2h,i) by a two-particle basis on a square lattice [ $a = 2r$ ; particle locations at  $(0, 0, 0)$  and  $(r, r, (1 + \sqrt{2})r)$ ] with mushroom caps oriented dimple-up in the upper layer. A lower layer oriented dimple-down yields the minimum height structure and was assumed for the model. The parameters for the  $2\Delta$  model were  $a = b = 2r, R = 120^\circ, \beta = 60^\circ$  and  $h_{min} = [2\sqrt{2/3} + 1]r$ , (half the height of a hexagonal bilayer of spheres plus two half-toroid segments). At heights larger than  $h_{min}$ , mixed dimple-up and dimple-down configurations are allowed (Figure 2.2j,k). Characteristic structural parameters for the idealized phases are summarized in Table 2.1.

Generally, each model structure is stable over the range where its plotted density profile is the highest compared with the other phases allowed by the confinement height

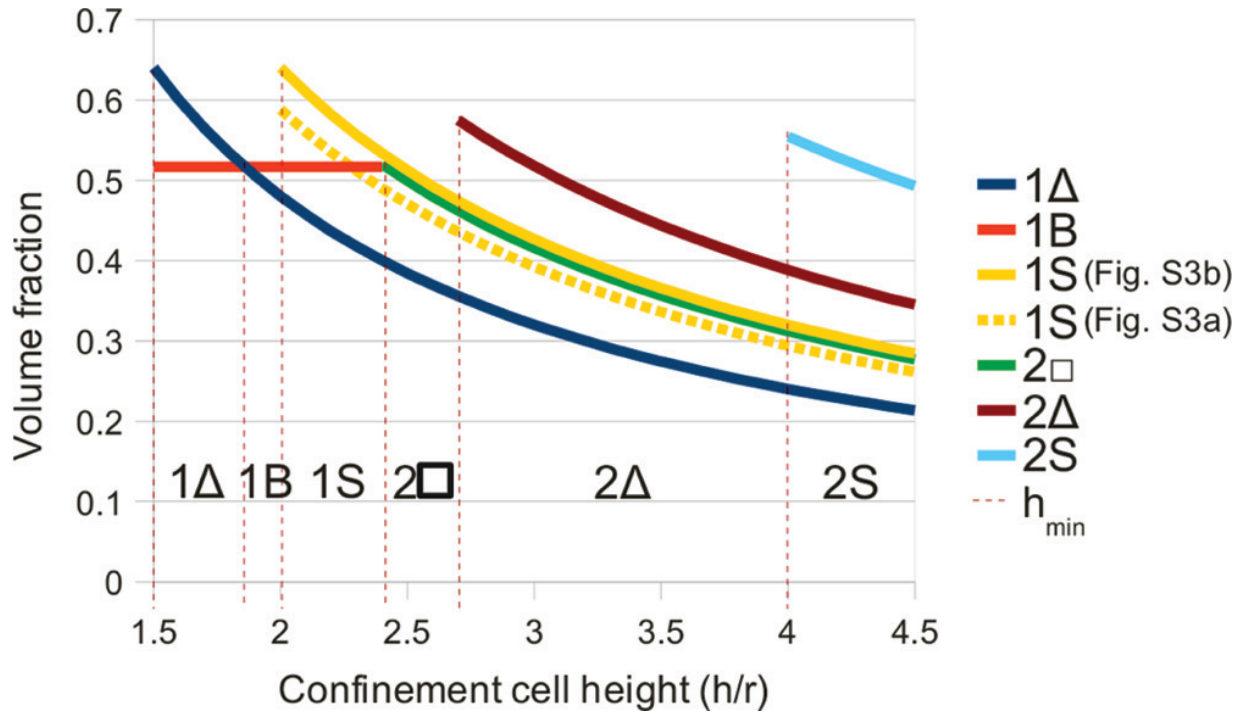


Figure 2.10: Effective density of idealized phases for mushroom cap particles as a function of confinement cell height. The cell height is given in terms of mushroom cap radius value,  $r$ .

Table 2.1: Confinement height and density constraints on monolayer and bilayer structures of mushroom caps

phases	height minimum	density @ $h_{min}$	symmetry	lattice
$1\Delta$	$1.5r$	0.64	$p6mm$	hexagonal
$1B$	$1.5r - 2.424r$	0.52	$p2mm$	rectangular
$1S_{ides}$	$2r$	0.59 – 0.64	$p2$	oblique
$2\Box$	$2.414r$	0.52	$p4mm$	square
$2\Delta$	$2.63r$	0.59	$p6mm$ , AB stacking	hexagonal
$2S_{ides}$	$4r$	0.55	$p2$ , AB stacking	oblique

(Figure 2.10). The hexagonal monolayer is the first phase geometrically allowed by the confinement conditions at the lowest height. Beyond  $h_{min}$ , the phase density decreases because more empty volume is available than is necessary to accommodate the close-packed arrangement. The  $1B$  phase becomes possible based on geometric arguments at  $h > 1.5r$ . However, the free energy of the system in the  $1B$  arrangement is only minimized once the effective density of the  $1\Delta$  phase drops below that of the  $1B$  phase. The higher density of  $1Sides$  at its  $h_{min}$  truncates the stability region of  $1B$  to  $h < 2r$ . A version of the  $1Sides$  phase (Supporting Information Figure 2.11b) is plotted to have greater density values than the  $2\Box$  phase at all heights. The suggested stability of  $1Sides$  over  $2\Box$  from theory is not supported by the experimentally observed phase behavior.

Frequent misorientation in the close-packed  $1Sides$  structure may decrease the density. The more open rotator  $1Sides$  phase must also be considered when settling rates are low enough for the orientationally disordered arrangements to be isolated as the structures evolve over time. The  $1Sides$  transition to  $2\Box$  may occur where  $h_{min} = 2.414r$  and takes place when the decreasing effective density of  $1Sides$  renders the free energy of the  $2\Box$  phase preferable. The transitions to  $2\Delta$  and  $2Sides$  may be explained following similar framework.

## 2.5 Conclusion

This work explores structural transformations for nonspherical mushroom cap-shaped colloids as directed by the gradient of confinement height in a wedge cell. Certain monolayer and bilayer phases of the system have commonality with those identified in spherical systems. However, the preferential orientation of particles in the  $1B$  and  $2\Box$  phases, as well as the existence of new  $1-$  and  $2Sides$  structures, is uniquely attributed to the mush-

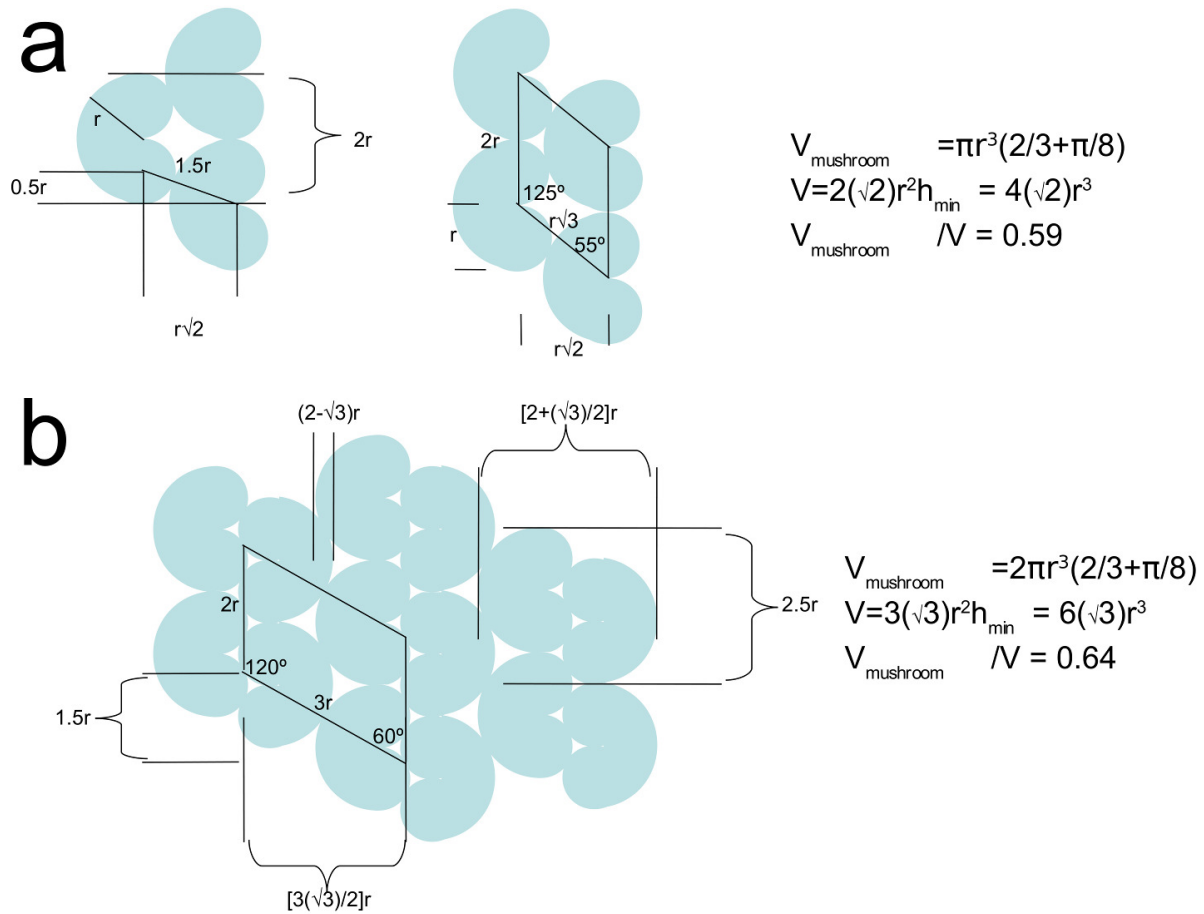


Figure 2.11: Idealized oblique structures for approximating the *1Sides* phase density.

room cap anisotropy. The quasi 2D regions, in which solidification occurs at intermediate confinement heights between integral numbers of particle layers, contained colloids that reorient and pack on oblique lattices either with rotational freedom or in dense smectic-like chaining formation at higher density. The sequence of phases determined as a function of height is  $1\Delta-1B-1Sides-2\Box-2\Delta-2Sides$ . The more complex orientation-dependent phases are reminiscent of the behavior in nonspherical spherocylinders and asymmetric dimers under confinement. Such processing methods that provide self-assembly of *any arbitrary shape* into ordered structures are central to the realization of low cost complex structures, in contrast to approaches that have relied on simple sphere deformation (i.e., stretching and pressing).[36, 12, 34] Exploring the mushroom cap films in dry form with appropriate dielectric backfilling is the subject of our further work toward photonic applications.

## REFERENCES

- [1] Peter Bolhuis and Daan Frenkel. Tracing the phase boundaries of hard spherocylinders. *J. Chem. Phys.*, 106(2):666–687, 1997.
- [2] P. I. Borel, Anders Harpøth, L. Frandsen, Martin Kristensen, Peixiong Shi, J. Jensen, and Ole Sigmund. Topology optimization and fabrication of photonic crystal structures. *Opt. Express*, 12(9):1996–2001, 2004.
- [3] Krzysztof Boryczko, Witold Dzwinel, and David A. Yuen. Dynamical clustering of red blood cells in capillary vessels. *J. Mol. Model.*, 9(1):16–33, 2003.
- [4] Martin Burger, Stanley J. Osher, and Eli Yablonovitch. Inverse problem techniques for the design of photonic crystals. *IEICE Trans. Electron.*, 87(3):258–265, 2004.
- [5] Julie A. Champion, Yogesh K. Katare, and Samir Mitragotri. Particle shape: A new design parameter for micro- and nanoscale drug delivery carriers. *J. Controlled Release*, 121(1-2):3–9, August 2007.
- [6] C. T. Chan, K. M. Ho, and C. M. Soukoulis. Photonic band gaps in experimentally realizable periodic dielectric structures. *Europhys. Lett.*, 16(6):563, 1991.
- [7] C.T. Chan, S. Datta, K.M. Ho, and C.M. Soukoulis. A7 structure: A family of photonic crystals. *Phys. Rev. B*, 50(3):1988–1991, July 1994.
- [8] Y. S. Chan, C. T. Chan, and Z. Y. Liu. Photonic band gaps in two dimensional photonic quasicrystals. *Phys. Rev. Lett.*, 80(5):956, 1998.
- [9] E. Cubukcu, K. Aydin, E. Ozbay, S. Foteinopoulou, and C. Soukoulis. Subwavelength resolution in a two-dimensional photonic-crystal-based superlens. *Phys. Rev. Lett.*, 91(20):207401, November 2003.
- [10] L. Dal Negro, M. Stolfi, Y. Yi, J. Michel, X. Duan, L. C. Kimerling, J. LeBlanc, and J. Haavisto. Photon band gap properties and omnidirectional reflectance in Si/SiO<sub>2</sub> Thue-Morse quasicrystals. *Appl. Phys. Lett.*, 84(25):5186–5188, 2004.
- [11] T. Decoopman, G. Tayeb, S. Enoch, D. Maystre, and B. Gralak. Photonic crystal lens: From negative refraction and negative index to negative permittivity and permeability. *Phys. Rev. Lett.*, 97(7):073905, August 2006.

- [12] Tao Ding, Zhan-Fang Liu, Kai Song, Koen Clays, and Chen-Ho Tung. Photonic crystals of oblate spheroids by blown film extrusion of prefabricated colloidal crystals. *Langmuir*, 25(17):10218–10222, September 2009.
- [13] A. D. Dinsmore, Eric R. Weeks, Vikram Prasad, Andrew C. Levitt, and D. A. Weitz. Three-dimensional confocal microscopy of colloids. *Appl. Opt.*, 40(24):4152–4159, August 2001.
- [14] Roel Dullens, Maurice Mourad, Dirk Aarts, Jacob Hoogenboom, and Willem Kegel. Shape-induced frustration of hexagonal order in polyhedral colloids. *Phys. Rev. Lett.*, 96(2):028304, January 2006.
- [15] Laura Filion, Matthieu Marechal, Bas van Oorschot, Daniël Pelt, Frank Smalenburg, and Marjolein Dijkstra. Efficient method for predicting crystal structures at finite temperature: Variable box shape simulations. *Phys. Rev. Lett.*, 103(18):188302, October 2009.
- [16] Marian Florescu, Salvatore Torquato, and Paul J. Steinhardt. Designer disordered materials with large, complete photonic band gaps. *Proc. Natl. Acad. Sci. U.S.A.*, 106(49):20658–20663, 2009.
- [17] T. Fujiwara, M. Kohmoto, and T. Tokihiro. Multifractal wave functions on a fibonacci lattice. *Phys. Rev. B*, 40(10):7413–7416, October 1989.
- [18] U. Gasser. Real-space imaging of nucleation and growth in colloidal crystallization. *Science*, 292(5515):258–262, April 2001.
- [19] Yilong Han, Yair Shokef, Ahmed M. Alsayed, Peter Yunker, Tom C. Lubensky, and Arjun G. Yodh. Geometric frustration in buckled colloidal monolayers. *Nature*, 456(7224):898–903, December 2008.
- [20] Kevin P. Herlihy, Janine Nunes, and Joseph M. DeSimone. Electrically driven alignment and crystallization of unique anisotropic polymer particles. *Langmuir*, 24(16):8421–8426, August 2008.
- [21] C.J. Hernandez and T.G. Mason. Colloidal alphabet soup: Monodisperse dispersions of shape-designed LithoParticles. *J. Phys. Chem. C*, 111(12):4477–4480, March 2007.
- [22] Marianne Hiltunen, Luca Dal Negro, Ning-Ning Feng, Lionel C. Kimerling, and Jurgen Michel. Modeling of aperiodic fractal waveguide structures for multifrequency light transport. *J. Lightwave Technol.*, 25(7):1841–1847, July 2007.

- [23] K. Ho, C. Chan, and C. Soukoulis. Existence of a photonic gap in periodic dielectric structures. *Phys. Rev. Lett.*, 65(25):3152–3155, December 1990.
- [24] K. M. Ho, C. T. Chan, C. M. Soukoulis, R. Biswas, and M. Sigalas. Photonic band gaps in three dimensions: New layer-by-layer periodic structures. *Solid State Commun.*, 89(5):413 – 416, 1994.
- [25] I. D. Hosein, M. Ghebrebrhan, J. D. Joannopoulos, and C. M. Liddell. Dimer shape anisotropy: a nonspherical colloidal approach to omnidirectional photonic band gaps. *Langmuir*, 26(3):2151–2159, 2009.
- [26] I. D. Hosein and C. M. Liddell. Convectively assembled asymmetric dimer-based colloidal crystals. *Langmuir*, 23(21):10479–10485, 2007.
- [27] I. D. Hosein and C. M. Liddell. Convectively assembled nonspherical mushroom cap-based colloidal crystals. *Langmuir*, 23(17):8810–8814, 2007.
- [28] Xunya Jiang, Yonggang Zhang, Songlin Feng, Kerwyn C. Huang, Yasha Yi, and J. D. Joannopoulos. Photonic band gaps and localization in the Thue-Morse structures. *Appl. Phys. Lett.*, 86(20):201110, 2005.
- [29] S.A. Kadlec, P.D. Beale, and J.C. Rainwater. Three-dimensional hard dumbbell solid free energy calculation via the fluctuating cell model. *Int. J. Thermophys.*, 25(5):1415–1427, 2004.
- [30] Jin-Woong Kim and Kyung-Do Suh. Monodisperse polymer particles synthesized by seeded polymerization techniques. *J. Ind. Eng. Chem.*, 14(1):1 – 9, 2008.
- [31] Hideo Kosaka, Takayuki Kawashima, Akihisa Tomita, Masaya Notomi, Toshiaki Tamamura, Takashi Sato, and Shojiro Kawakami. Superprism phenomena in photonic crystals. *Phys. Rev. B*, 58(16):R10096–R10099, October 1998.
- [32] Hideo Kosaka, Takayuki Kawashima, Akihisa Tomita, Masaya Notomi, Toshiaki Tamamura, Takashi Sato, and Shojiro Kawakami. Self-collimating phenomena in photonic crystals. *Appl. Phys. Lett.*, 74(9):1212, 1999.
- [33] Stephanie H Lee, Esther Y. Fung, E. K. Riley, and C. M. Liddell. Asymmetric colloidal dimers under quasi-2D confinement. *Langmuir*, 25(13):7193–7195, 2009.
- [34] Pushkar P. Lele and Eric M. Furst. Assemble-and-stretch method for creating two- and three-dimensional structures of anisotropic particles. *Langmuir*, 25(16):8875–8878, August 2009.

- [35] Jongsun Lim, Seung Seok Oh, Doo Youp Kim, Sang Hee Cho, In Tae Kim, S. H. Han, Hideo Takezoe, Eun Ha Choi, Guang Sup Cho, Yoon Ho Seo, Seung Oun Kang, and Byoungchoo Park. Enhanced out-coupling factor of microcavity organic light-emitting devices with irregular microlens array. *Opt. Express*, 14(14):6564–6571, July 2006.
- [36] Yu Lu, Yadong Yin, Zhi-Yuan Li, and Younan Xia. Colloidal crystals made of polystyrene spheroids: Fabrication and Structural/Optical characterization. *Langmuir*, 18(20):7722–7727, October 2002.
- [37] Chiyan Luo, Steven G. Johnson, J. D. Joannopoulos, and J. B. Pendry. All-angle negative refraction without negative effective index. *Phys. Rev. B*, 65(20):201104, May 2002.
- [38] Martin Maldovan, Chaitanya K. Ullal, W. Craig Carter, and Edwin L. Thomas. Exploring for 3D photonic bandgap structures in the 11 f.c.c. space groups. *Nature Mater.*, 2(10):664–667, September 2003.
- [39] Leo Merz, Manfred Parschau, Laura Zoppi, Kim K. Baldrige, Jay S. Siegel, and Karl-Heinz Ernst. Reversible phase transitions in a buckyball monolayer. *Angew. Chem., Int. Ed.*, 48(11):1966–1969, March 2009.
- [40] Eric B. Mock and Charles F. Zukoski. Determination of static microstructure of dilute and concentrated suspensions of anisotropic particles by ultra-small-angle x-ray scattering. *Langmuir*, 23(17):8760–8771, August 2007.
- [41] Ali Mohraz and Michael J. Solomon. Direct visualization of colloidal rod assembly by confocal microscopy. *Langmuir*, 21(12):5298–5306, June 2005.
- [42] Stephan Nesper, Clemens Bechinger, Paul Leiderer, and Thomas Palberg. Finite-size effects on the closest packing of hard spheres. *Phys. Rev. Lett.*, 79(12):2348–2351, 1997.
- [43] T. T. Ngo, C. M. Liddell, M. Ghebrebrhan, and J. D. Joannopoulos. Tetrastack: Colloidal diamond-inspired structure with omnidirectional photonic band gap for low refractive index contrast. *Appl. Phys. Lett.*, 88(24):241920, 2006.
- [44] M. Notomi. Theory of light propagation in strongly modulated photonic crystals: Refractionlike behavior in the vicinity of the photonic band gap. *Phys. Rev. B*, 62(16):10696–10705, October 2000.
- [45] M. Okubo, H. Minami, and K. Morikawa. Production of micron-sized, monodis-

- perse, transformable rugby-ball-like-shaped polymer particles. *Colloid Polym. Sci.*, 279(9):931–935, 2001.
- [46] Masayoshi Okubo and Hideto Minami. Production of micron-sized monodispersed anomalous polymer particles having red blood corpuscle shape. *Macromol. Symp.*, 150(1):201–210, February 2000.
- [47] B. Pansu, Pi. Pieranski, and Pa. Pieranski. Structures of thin layers of hard spheres : high pressure limit. *J. Phys. (Paris)*, 45(2):331–339, 1984.
- [48] John Brian Pendry. Negative refraction makes a perfect lens. *Phys. Rev. Lett.*, 85(18):3966–3969, 2000.
- [49] Pawel Pieranski, L. Strzelecki, and B. Pansu. Thin colloidal crystals. *Phys. Rev. Lett.*, 50(12):900, 1983.
- [50] Tushar Prasad, Vicki Colvin, and Daniel Mittleman. Superprism phenomenon in three-dimensional macroporous polymer photonic crystals. *Phys. Rev. B*, 67(16):165103, April 2003.
- [51] Stefan Preble, Michal Lipson, and Hod Lipson. Two-dimensional photonic crystals designed by evolutionary algorithms. *Appl. Phys. Lett.*, 86(6):061111, 2005.
- [52] F. Ramiro-Manzano, E. Bonet, I. Rodriguez, and F. Meseguer. Layering transitions in confined colloidal crystals: The hcp-like phase. *Phys. Rev. E*, 76(5):050401R, November 2007.
- [53] James W. Rinne and Pierre Wiltzius. Design of holographic structures using genetic algorithms. *Opt. Express*, 14(21):9909–9916, 2006.
- [54] Matthias Schmidt and Hartmut Löwen. Freezing between two and three dimensions. *Phys. Rev. Lett.*, 76(24):4552–4555, 1996.
- [55] I. V. Schweigert, V. A. Schweigert, and F. M. Peeters. Enhanced stability of the square lattice of a classical bilayer wigner crystal. *Phys. Rev. B*, 60(21):14665–14674, December 1999.
- [56] Linfang Shen, Zhuo Ye, and Sailing He. Design of two-dimensional photonic crystals with large absolute band gaps using a genetic algorithm. *Phys. Rev. B*, 68(3):035109, July 2003.

- [57] Zhenquan Tan, Akito Masuhara, Hitoshi Kasai, Hachiro Nakanishi, and Hidetoshi Oikawa. Multibranched c 60 Micro/Nanocrystals fabricated by reprecipitation method. *Jpn. J. Appl. Phys.*, 47(2):1426–1428, February 2008.
- [58] Ovidiu Toader and Sajeev John. Proposed square spiral microfabrication architecture for large three-dimensional photonic band gap crystals. *Science*, 292(5519):1133–1135, May 2001.
- [59] Ken-ichi Tsubota, Shigeo Wada, Hiroki Kamada, Yoshitaka Kitagawa, Rui Lima, and Takami Yamaguchi. A particle method for blood flow simulation: application to flowing red blood cells and platelets. *J. Earth Sim.*, 5:2–7, March 2006.
- [60] Y. Xia, B. Gates, and Z.-Y. Li. Self-assembly approaches to three-dimensional photonic crystals. *Adv. Mater.*, 13(6):409–413, March 2001.
- [61] E. Yablonovitch, T. Gmitter, and K. Leung. Photonic band structure: The face-centered-cubic case employing nonspherical atoms. *Phys. Rev. Lett.*, 67(17):2295–2298, October 1991.
- [62] Eli Yablonovitch. Photonic crystals: Towards rational material design. *Nature Mater.*, 2(10):648–649, 2003.
- [63] He Yan, Claire Gu, Changxi Yang, Jie Liu, Guofan Jin, Jiatao Zhang, Lantian Hou, and Yuan Yao. Hollow core photonic crystal fiber surface-enhanced raman probe. *Appl. Phys. Lett.*, 89(20):204101, 2006.
- [64] Vassilios Yannopapas. Negative refractive index in the near-UV from au-coated CuCl nanoparticle superlattices. *Phys. Status Solidi RRL*, 1(5):208–210, October 2007.
- [65] Y. Yin and Y. Xia. Self-assembly of monodispersed spherical colloids into complex aggregates with well-defined sizes, shapes, and structures. *Adv. Mater.*, 13(4):267–271, February 2001.
- [66] M. E. Zoorob, M. D. B. Charlton, G. J. Parker, J. J. Baumberg, and M. C. Netti. Complete photonic bandgaps in 12-fold symmetric quasicrystals. *Nature*, 404(6779):740–743, 2000.

## CHAPTER 3

# BUCKLED COLLOIDAL CRYSTALS WITH NONSPHERICAL BASES FOR TWO-DIMENSIONAL SLAB PHOTONIC BAND GAPS\*

### 3.1 Abstract

Theoretical modeling of the photonic band gap forming properties is reported for the buckled phase of anisotropic particles. These exist between the first and second particulate layers of confined colloidal suspensions. Inspired by the range of non-spherical mushroom-cap building blocks for self-assembly that have been synthesized using seeded emulsion-polymerization, we explore in particular the band structures as a function of toroid shape parameter. The parameter is adjusted to incrementally transform hemispheres to spheres. Additionally, corrugation heights that systematically modulate the slab photonic crystal unit cell from rectangular monolayer to square bilayer are investigated. Polarization independent gaps in the guided modes are determined for direct and inverted structures that exhibit bifurcation in the particle orientation perpendicular to the slab plane. Gaps in the guided modes are observed between the fourth and fifth, twelfth and thirteenth, as well as higher band locales as the particle morphology and lattice aspect ratio vary.

---

\*Originally published as: Erin K. Riley, Esther Y. Fung, and Chekesha M. Liddell Watson. "Buckled colloidal crystals with nonspherical bases for two-dimensional slab photonic band gaps", *J Appl Phys*, **111**, 093504 (2012). Reprinted by permission of the American Institute of Physics, <http://dx.doi.org/10.1063/1.4706556>.

## 3.2 Introduction

Advances in synthesis and processing science undergird the growth of low cost, large area manufacturing at the mesoscale, so that utilizing features of diverse unconventional structures in light control is becoming a reality. For instance, three or four beam interference in holography techniques has been used to define the period, symmetry, and shape of photonic crystal lattice elements in photosensitive polymers. The wavelength, relative phases, polarization, and incidence directions of continuous-wave visible lasers provide the controls.[26, 27, 43] Inverse design is possible where given a desired optical profile, the proper beam pattern can be devised, in contrast to the common empirical 'guess and check' approach to the search for band gaps. However, the complexity of the optical set up presents limitations on the ability to fabricate any arbitrary structure as a photonic crystal template.

Elastic deformation and solvent-induced swelling instability have produced derivatives from a PDMS (polydimethylsiloxane) membrane with a variety of arrangements that were calculated to sustain 2D optical band gaps. These were established predominantly for the transverse magnetic polarization (TM, magnetic field component in-plane) when patterns were transferred to high refractive index silicon posts. The applied uniaxial strain transformed square lattice structures of ellipses in 'herringbone' orientations to (1) centered-rectangular compound structures (i.e., a basis of elliptical lines with different aspect ratios or of circles and ellipse features) and (2) primitive rectangular lattices of elliptical scatterers aligned along the stretching direction.[45]

Colloidal self-assembly under confinement in wedge geometry as well allows a range of atypical structures to be systematically accessed with ease. The cell height relative to the particle size determines changes in state. Particularly, the availability of nonspherical

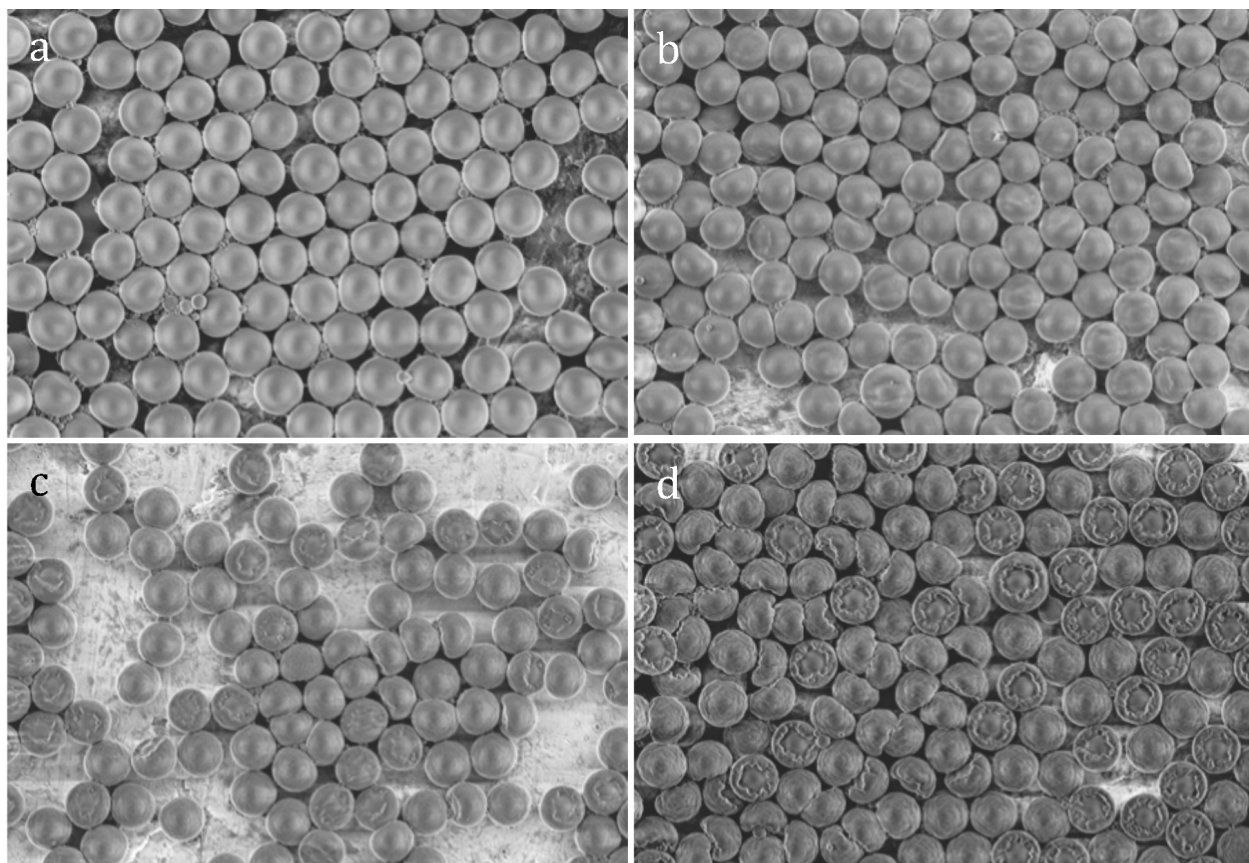


Figure 3.1: SEM images of morphologies obtained using 2% DVB seed PS particles and DVB content in the second stage swelling of (a) 10% DVB, minor non-spherical deformation, slightly flattened side; (b) 15% DVB, toroid shape parameter 54%; (c) 20% DVB, toroid shape parameter 42%; and (d) 30% DVB, toroid shape parameter 34%. Collapsed shape becomes obvious for particles deposited with axis of circular symmetry near parallel to the substrate plane. Scale bars indicate 1  $\mu\text{m}$ .

particle morphologies with narrow size/shape distribution— boomerang, square cross, hexagonal prism, flying saucer, blood cell, w-motif, ellipsoid, peanut, cylinder, spherocylinder, heteronuclear dimer, etc.— expands the approach.[44, 39, 33, 3, 31, 30, 12, 13, 20] Recently, buckled phases ( $1B$ ) of anisotropic particles were captured at transition heights between the first and second particulate layers.[36] The mushroom cap-shaped building blocks in the idealized  $1B$  phase self-organize on a rectangular lattice into vertically shifted sublayers, each having a particle orientation preference towards opposite confining walls to achieve the highest packing density (Figures 3.2 and 3.3).

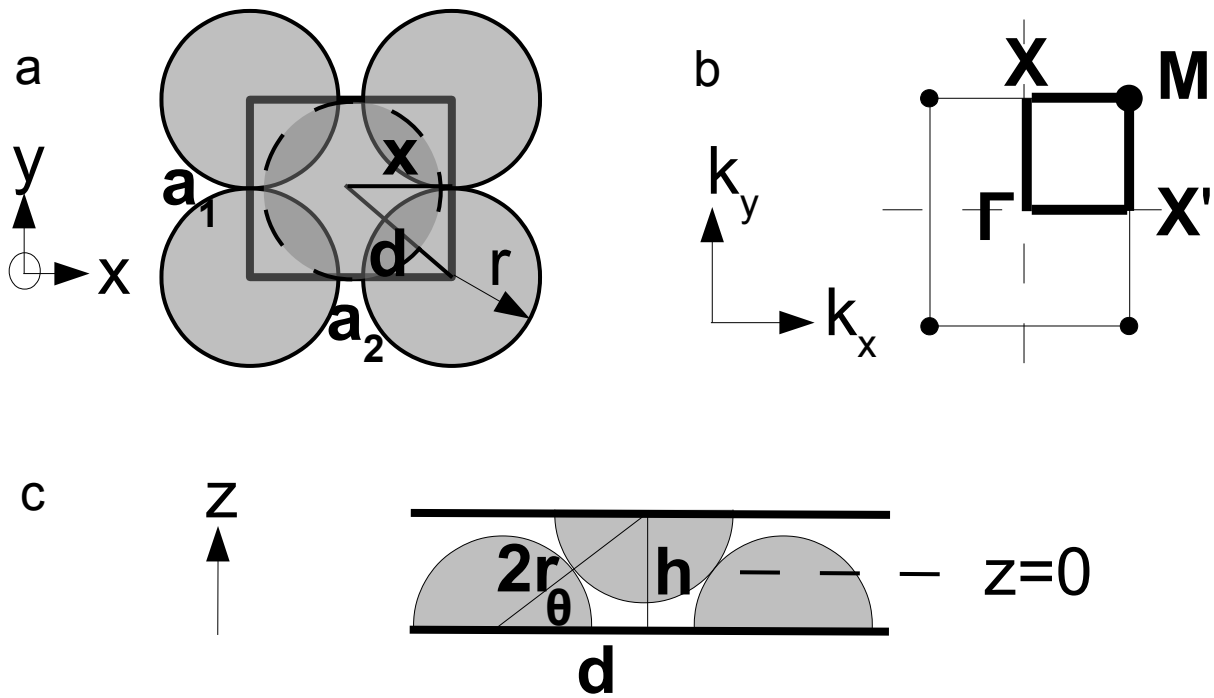


Figure 3.2: Model buckled structure.(a) Rectangular unit cell at  $z = -h/2$ ; (b) Brillouin zone of the rectangular lattice (irreducible Brillouin zone highlighted) with high symmetry points indicated; (c) cross-section of buckled hemisphere structure along  $\langle \bar{1}1 \rangle$  direction.

The quasi-two dimensional structure is related to the class of reduced symmetry configurations (compared to the sphere-based triangular lattice), which have been explored for lifting degeneracy in photonic bands. These arrangements open full 2D band gaps through lattice parameter distortion, nonspherical motif rotation, and/or introduction of

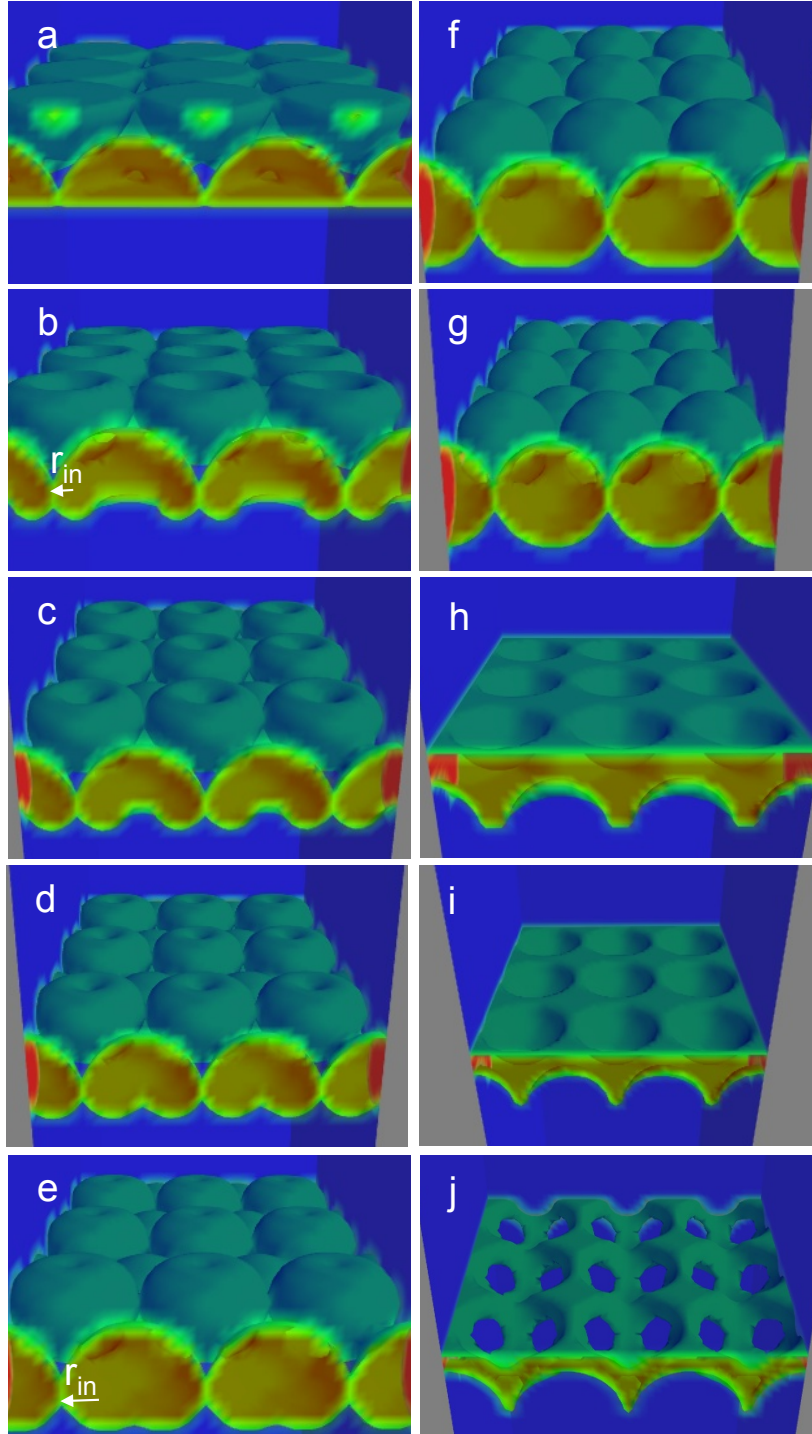


Figure 3.3: Schematics for the direct buckled structures with height of  $r_{in} + 1.40r$  and toroid shape parameter  $r_{in}$  as a fraction of the hemisphere radius,  $r$ : (a) 0% (hemisphere); (b) 30%; (c) 40%; (d) 50% ('horn mushroom cap'); (e) 60%; (f) 80%; and (g) 100% (sphere). Schematics of the inverted buckled hemisphere structures with  $w/l = 1.09$  and  $h = 1.35r$  as the filling fraction  $f$  is varied by changing the hemisphere radius: (h)  $r = 0.40$  and  $f = 63\%$ ; (i)  $r = 0.46$  and  $f = 44\%$ ; and (j)  $r = 0.50$  (tangent) and  $f = 29\%$ .

superlattice features (e.g., periodic extra or missing elements). Practical realizations are often thin dielectric slabs with planar photonic crystal patterning ‘sandwiched’ between claddings of air or low index background material. Light is confined by index guiding in the third dimension. Compared to the ideal infinite versions that are extended vertically, photonic enhancements can be much more modest in slab structures and are significantly improved using the strategies for symmetry reduction.[42] For photonic crystal slabs (PCSs) of air holes in silicon with thickness of 458 nm and 422 nm, respectively, a full band gap (midgap frequency  $\sim 1.55 \mu\text{m}$ ) in the guided modes opens to 10.2% relative width (gap-midgap ratio,  $\Delta\omega/\omega$ ) for a hexagon motif rotated  $9^\circ$  with respect to the lattice vectors of a triangular lattice and to 8.9% relative width for a square motif rotated  $30^\circ$  on a square lattice.[2] Pores shaped as trimers of ellipses (three overlapping elliptical holes with major axes inclined  $120^\circ$  to each other) on a triangular lattice silicon slab of 320 nm thickness were calculated to yield a maximum width of 11%. The gap was optimized by modifying the degree of fusion for the ellipses and the aspect ratio of their major and minor pore axes. The honeycomb structure with a basis of two dissimilar-sized circular holes per cell also promotes a full gap. The relative width value is tunable up to 10% through modifying the radius ratio.[42] Optical mode splitting at the high symmetry K-point of the band structure is induced by the elimination of a mirror operation in the reciprocal lattice in comparison to the case for a single circular pore size. In the later case, the corresponding gap between the first and second bands is closed for one polarization.

Motivated by the observed  $1B$  phase that can be self-assembled from partially collapsed colloidal building blocks (Figure 3.1) in confinement experiments,[36] the present work investigates photonic properties of quasi-2D buckled films composed of nonspherical 3D motifs. Specifically, we explore the formation of photonic band gaps as a function of toroid shape parameter. Hemispheres joined with hemi-torus features are incrementally transformed to spheres (Figure 3.2). Mushroom cap-shaped particles similar to those

in Refs. [36] and [14] lie along the continuum. The influence of corrugation height on the optical properties is also studied. This degree of buckling in the photonic crystal is directly related to the rectangular aspect ratio of the top plan projection for the slab unit cell. Dielectric or ‘air’ particle tangency is enforced in direct and inverted realizations of the films. This is consistent with basic self-assembly and backfilling (i.e., inverted structures). The restriction is removed when the effects of solid volume filling fraction are examined through varying particle size. Buckling and pore shaping in 3D impart atypical vertical variation in the slab structures. The mid-slab mirror symmetry, present for numerous slab configurations in the literature due to a uniform cross-sectional profile throughout the thickness, is substituted with a diagonal glide element here. Polarization independent gaps in the guided modes were determined for the first time in structures with bifurcation in the particle orientation (e.g., dimple up or dimple down) perpendicular to the slab plane. Notably, the necessity to engineer overlap frequencies of odd and even mode [TM-like and TE-like (electric field component in-plane)] gaps is eliminated by the change in symmetry. The lowest lying full gaps in the guided modes were found between the fourth and fifth photonic bands (4–5 gap) for the inverse buckled particulate monolayers with shape parameters clustered near those of hemispheres.

### **3.3 Model and Calculation**

Anisotropic particle shapes in the family modeled in this work can arise from evacuation of swelling solvent and unreacted monomer through the mildly crosslinked skin layer as a colloid undergoes contraction. Deformation is driven by the pressure gradient across the shell during transport through the porous surface. The isotropic shrinkage transitions to regimes where the inhomogeneous membrane shell flattens, curvature reversal occurs forming a depression, an invagination ensues, and its tip deepens until tearing connects

to a hollow or solid central core region.[34] Figure 3.1 highlights the shape transformation of 500 nm polystyrene (PS) colloids prepared by seeded emulsion polymerization. The 2 % divinylbenzene (DVB) seed particles (monomer composition of 5.880 mL styrene and 120  $\mu$ L DVB) were swelled with monomer, crosslinker, and anhydrous toluene in the presence of polyvinylalcohol stabilizer and hydroquinone inhibitor. Polymerization at an elevated temperature of 70 °C yielded increasingly collapsed morphology over the range of 5 % to 30 % DVB addition in the second stage.

To incrementally capture the morphology development, a geometric model was defined through joining at the origin a hemisphere,  $z = -\sqrt{r^2 - x^2 - y^2}$ , to a hemi-torus,  $z = +\sqrt{r_{in}^2 - [(r - r_{in}) - \sqrt{x^2 + y^2}]^2}$ , where  $r_{in}$  and  $r - r_{in}$  are the inner and outer hemi-toroid radii at the  $z = 0$  plane. The transformation from hemisphere through ‘mushroom cap’ shaped particles to spheres is illustrated in Figure 3.2 as the shape parameter  $r_{in}$  increases from 0 to  $1r$ . The so called ‘horn torus’ capping feature corresponds to toroid shape parameter of  $r_{in} = 0.5r$ .

A few buckled arrangements have been identified to satisfy geometric frustration when such particles are confined by actuated parallel plates or a wedge cell. The phase transformations for both systems of spheres and mushroom caps have been shown to take place from a hexagonal close-packed monolayer to the square bilayer structure through transitional buckling structures—(1) straight-striped (parallel alternating lines of raised adjacent particles); (2) zigzag (striped rows with directional deviations); and (3) disordered (raised particles randomly situated among lattice sites). As a first approximation for the class, the more closely packed straight-striped phase was modeled (Figure 3.3). This  $1B$  phase is represented on a rectangular lattice with a two-particle basis and  $p2mm$  plane group symmetry of the top projection. The row tangency requirement constrains the primitive planar lattice vectors to  $\vec{a}_1 = [100]$  (width  $w = |\vec{a}_1| = 2\sqrt{3r^2 - (h - 2r_{in})^2}$ )

and  $\vec{a}_2 = [010]$  (length  $l = |\vec{a}_2| = 2r$ ) and applies to the confinement heights ( $h$ ) in the range,  $1r < h < \sqrt{2}r + 2r_{in}$ . The anisotropic particles constituting the basis have the hemi-object union at coordinates given by  $(0, 0, r_{in} - \frac{h}{2})$  and  $(\frac{1}{2}, \frac{1}{2}, \frac{h}{2} - r_{in})$  with the isotropic cross-sections oriented in the  $[00\bar{1}]$  and  $[001]$  directions, respectively. As the confinement height expands, the motifs at  $1/2\vec{a}_1, 1/2\vec{a}_2$  shift further out-of-plane, and the interrow distance of oppositely oriented particles decreases.

The photonic band structures of the buckled films were calculated according to the vectorial plane wave method implemented using the MIT Photonic Bands (MPB) software package.[19] Periodic boundary conditions were imposed with large intervals between the slabs in the stack, spaced by eight times the lattice constant  $\vec{a}_1$ . The dispersion curves of light frequency versus wavevector (reciprocal lattice vector) were computed along the path between high symmetry points of the irreducible Brillouin zone for the rectangular lattice in reciprocal space (Figure 3.3(b)). Eigenfrequencies were determined for the first twenty bands within 0.001 % convergence tolerance for the computational cell of mesh size 5 and resolutions of 16 or 32. The values correspond to a typical minimum of 4096 or 32768 plane waves. A continuous opaque region (light cone) representing all bulk background radiant frequencies is overlaid (Figure 3.4, grey) having a lower limit calculated as the wavevector divided by the refractive index of the air ( $n = 1$ ) cladding. Guided modes associated with the direct and inverted photonic crystal patterning evaluated for dielectric contrasts from 6 to 16 appear below the light line. Ten wavevectors were initially interpolated between each critical symmetry point. When full band gaps were found in the sense that there were no guided modes for the frequency range of the band gap, the structures were further analyzed by 100 wavevector interpolation as was required to obtain a sufficient level of band structure detail. The simulation was performed without polarization constraints because of the absence of a mirror plane parallel to the slab.

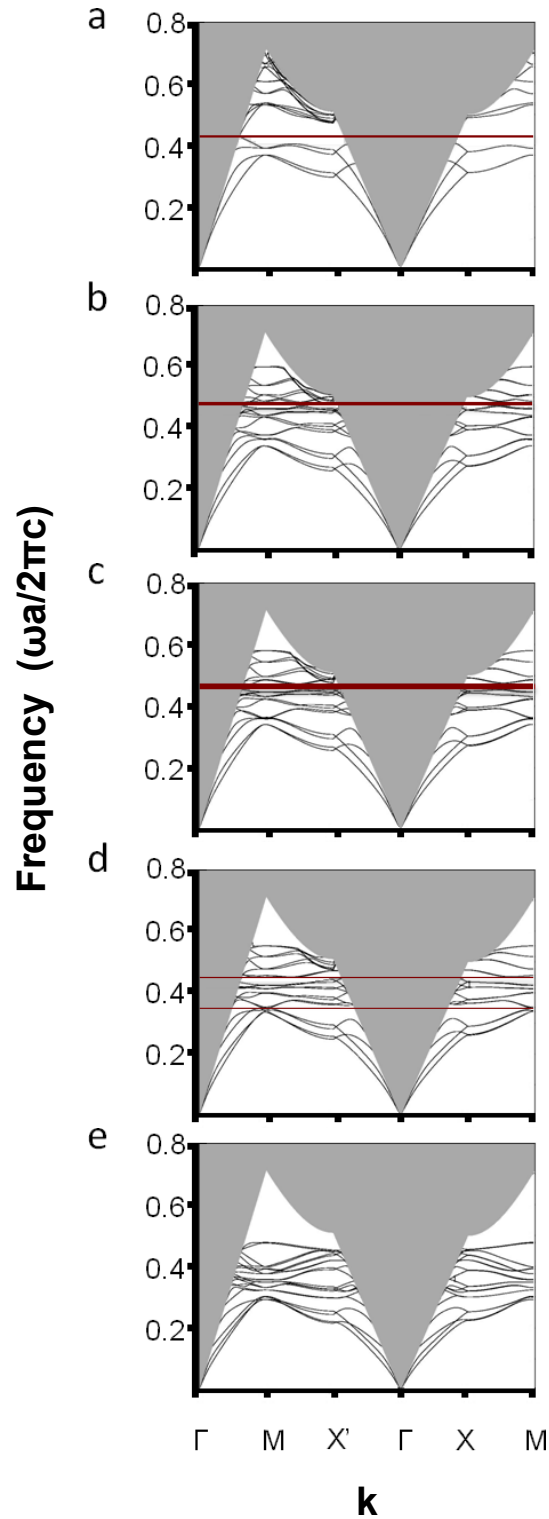


Figure 3.4: Band diagrams of inverted buckled mushroom cap ( $w/l = 1.02$  and  $\epsilon_c = 14.0$ ) as a function of toroid shape parameter: (a)  $r_{in} = 0\%$  and  $f = 26.7\%$ ; (b)  $r_{in} = 40\%$  and  $f = 32.2\%$ ; (c)  $r_{in} = 50\%$  and  $f = 32.0\%$ ; (d)  $r_{in} = 60\%$  and  $f = 33.1\%$ ; and (e)  $r_{in} = 100\%$  and  $f = 39.6\%$ . Air voids assumed tangent.

### 3.4 Results and Discussion

Full band gaps in the guided modes were determined in both direct and inverse structures at high degrees of buckling. The representative band diagram series provided in Figure 3.4 details the evolution of the inverted buckled mushroom cap system as a function of particle shape, with the particles remaining tangent. The rectangular aspect ratio ( $w/l$ ) and the dielectric contrast ratio ( $\epsilon_c$ ) are constant at 1.02 and 14.0, respectively. The lowest lying 4–5 gap (Figure 3.4(a)) opened at minimum dielectric filling for the inverted buckled hemisphere structure, but closed near the M symmetry point (M-point) in the mushroom cap systems due to the relative increase in filling fraction. As the toroid shape parameter increased, the filling fraction of the inverted structure passed through a local minimum (supplemental Figure 3.5(b)) generating the 12 – 13 band gap (Figures 3.4(b)-3.4(d)). This gap closed at higher shape parameters and filling fractions, since the bands were pulled down to lower frequencies (Figure 3.4(e)).

The gap width (gap-to-midgap ratio) as a function of dielectric contrast ( $w/l = 1.02$ ) is provided in Figure 3.6 for the 4 – 5 gap in the inverted hemisphere and the 12 – 13 gap in the inverted mushroom cap structures. The 4 – 5 gap size remained smaller than the simulation error (1 %) at the aspect ratio 1.02. The 12 – 13 gap opened in the mushroom cap systems ( $r_{in}$  from 40 % $r$  to 60 % $r$ ) when a degeneracy at the  $X'$  symmetry point ( $X'$ -point) lifted. The 12 – 13 gap in the three systems opened at lower  $\epsilon_c$  as the toroid shape parameter increased (Figure 3.6(b)), and the maximum gap was determined for the configuration with a filling fraction that corresponded to the local minimum ( $f = 32.0\%$ ). The difference in filling fractions for the 40 % $r$  and 50 % $r$  mushroom cap systems was small (0.2 %). However, the 60 % $r$  mushroom cap system promoted gap formation at a reduced dielectric contrast is consistent with the principle that to minimize mode energy, more field will concentrate in the dielectric material when the dielectric constant is lower.[19]

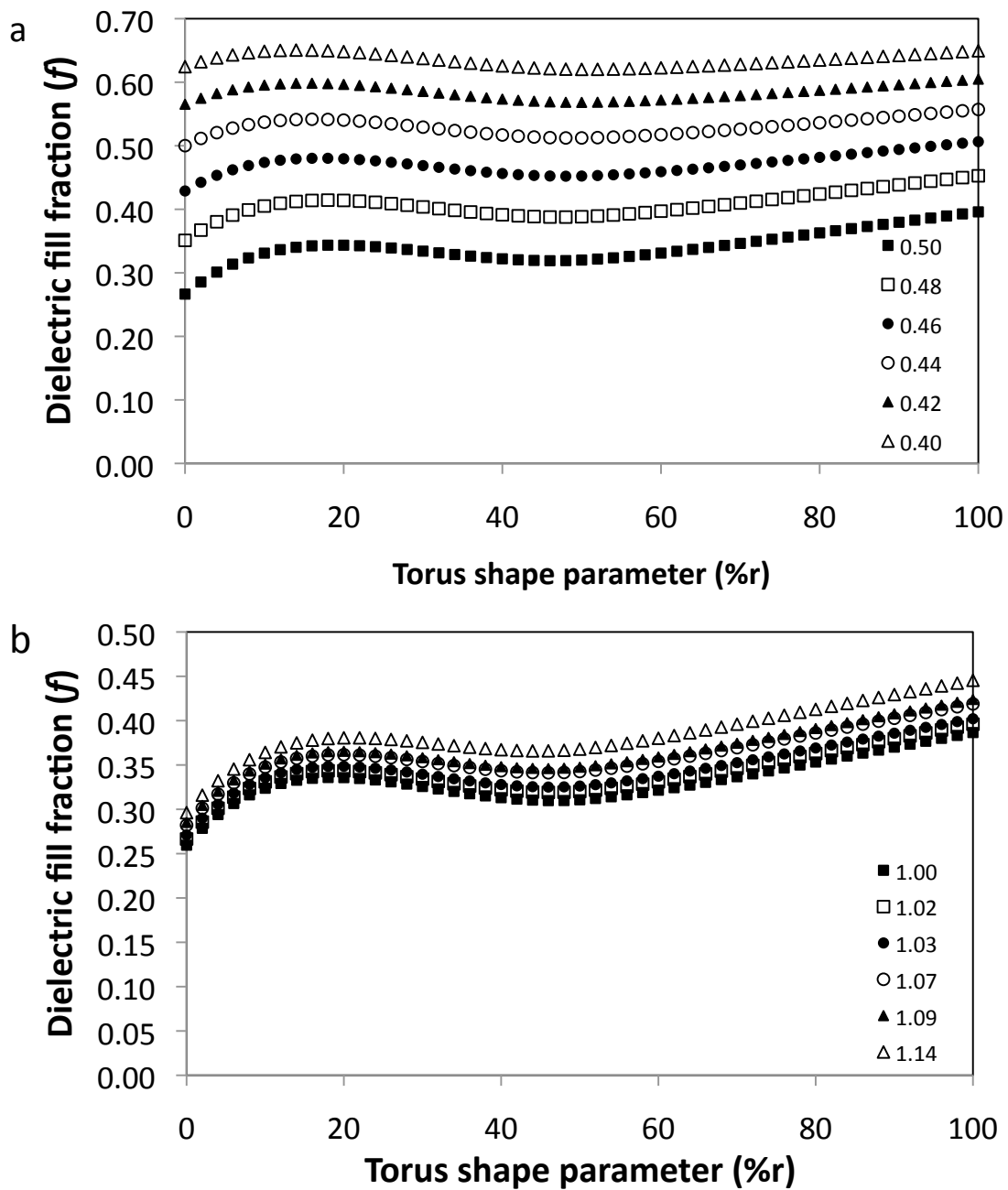


Figure 3.5: Dielectric filling fraction as a function of particle shape for inverted structures with a) particle radius ranging from tangent condition ( $r = 0.50$ ) to strongly separated particles ( $r = 0.40$ ). The rectangular aspect ratio  $w/l$  is held constant at 1.02. b) Particles are tangent and  $w/l$  varies from 1.00 to 1.14

The condition is easily satisfied for higher filling fraction structures.

The generation and closure of the photonic band gaps can be rationalized from the displacement field distribution (i.e., dielectric constant electric field) in the dielectric material as shown in Figure 3.7. Field maps associated with the 4th and 5th bands of the inverted buckled hemisphere system at the M-point indicated the modes were arranged dissimilarly. The electromagnetic field energy of the 4th band concentrated in the high dielectric material as connected paths, while the field energy of the 5th band was tightly localized. The intense field regions for the 4th and 5th bands at the M-point in the inverted mushroom cap ( $r_{in} = 50\%r$ ) system were instead distributed in equivalent patterns, resulting in a band degeneracy. No gap was found in the assembly of inverted spheres modeled, since the high percentage of the displacement (magnetic) field in the dielectric for the 4th band [94 % (40 %)] and 5th band [93 % (71 %)] at the M-point, compressed the band structure to lower frequencies. Gaps between high indexed bands in a 2D, large  $\epsilon_c$  ( $> 20$ ) system[6] have been reported between so called 'dielectric' bands representing the electromagnetic field concentrated in the high dielectric regions of the material. The gaps were formed due to the change in the mode distribution *within* the dielectric (rather than concentration in dielectric versus air) and were related strongly to the Mie resonance of the scatterers.[6] The localized photonic states were readily explained through a tight-binding model for the linear combination of Mie resonances. Such gaps have been found to be resilient to changes in periodicity, but are sensitive to variation in the scattering cross-section, i.e., shape.[25] Mie resonance dominated gaps have also been associated with amorphous diamond-, 2D hyperuniform disordered-, and quasiperiodic structures (e.g., eight-, ten-, and twelvefold-symmetric quasicrystals), where gaps survive in the presence of various types of disorder.[8, 9, 16]

To investigate the impact of the rectangular lattice symmetry on the 4 – 5 and 12 – 13

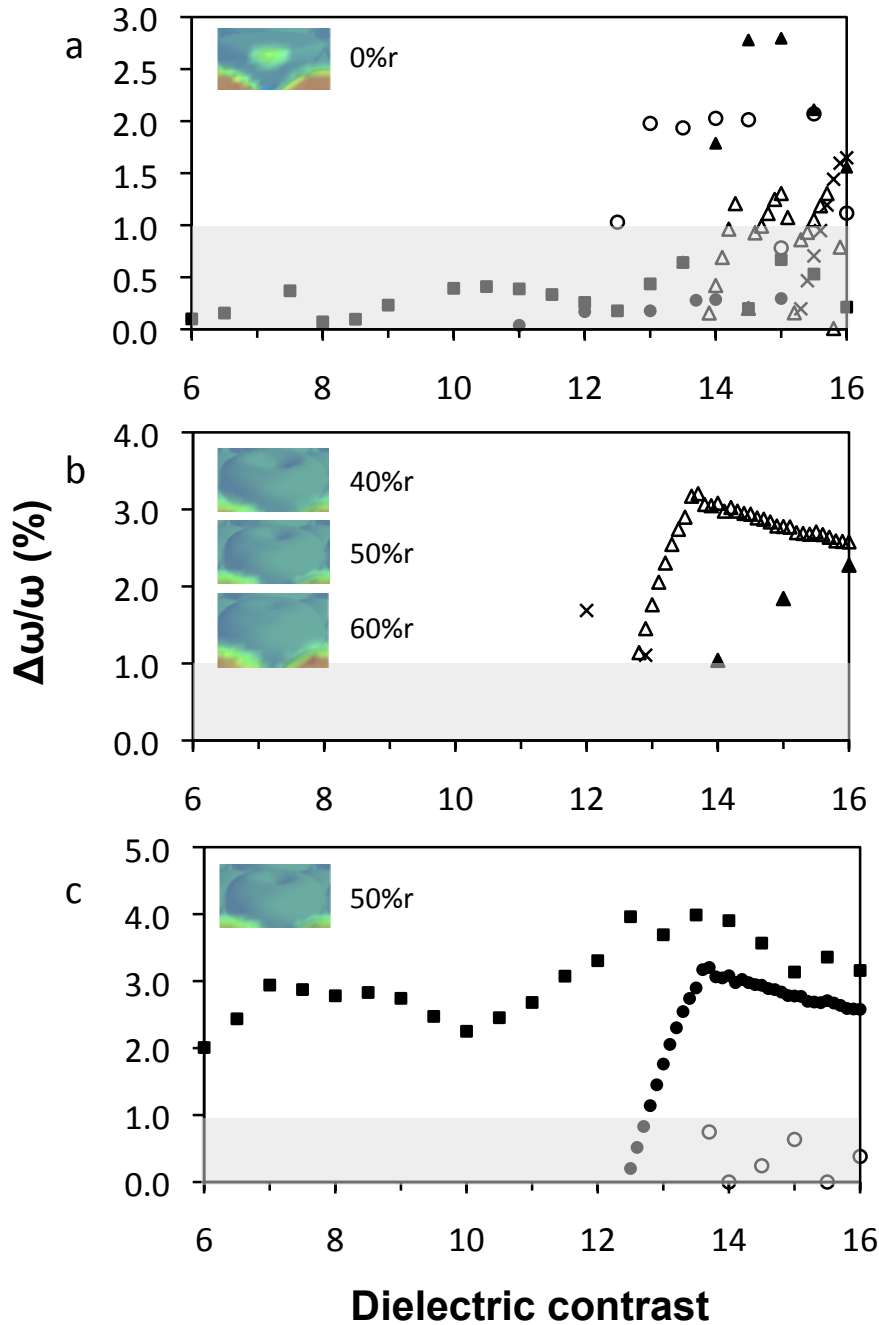


Figure 3.6: (a) 4 – 5 band gap in inverted buckled hemisphere ( $r_{in} = 0\%$ ) structures with  $w/l = 1.07$  (cross), 1.06 (open triangle), 1.05 (solid triangle), 1.03 (open circle), 1.02 (solid circle), and 1.00 (solid square). (b) 12 – 13 band gap in inverted buckled mushroom cap structures at rectangular aspect ratio 1.02 and toroid parameter  $r_{in}$  of 40%r (solid triangle), 50%r (open triangle), and 60%r (cross). (c) 12 – 13 gap in inverted buckled mushroom cap ( $r_{in} = 50\%$ ) structure as a function of aspect ratio:  $w/l = 1.00$  (solid square), 1.02 (solid circle), and 1.03 (open circle). Direct particle shapes and the corresponding toroid shape parameters are shown in insets.

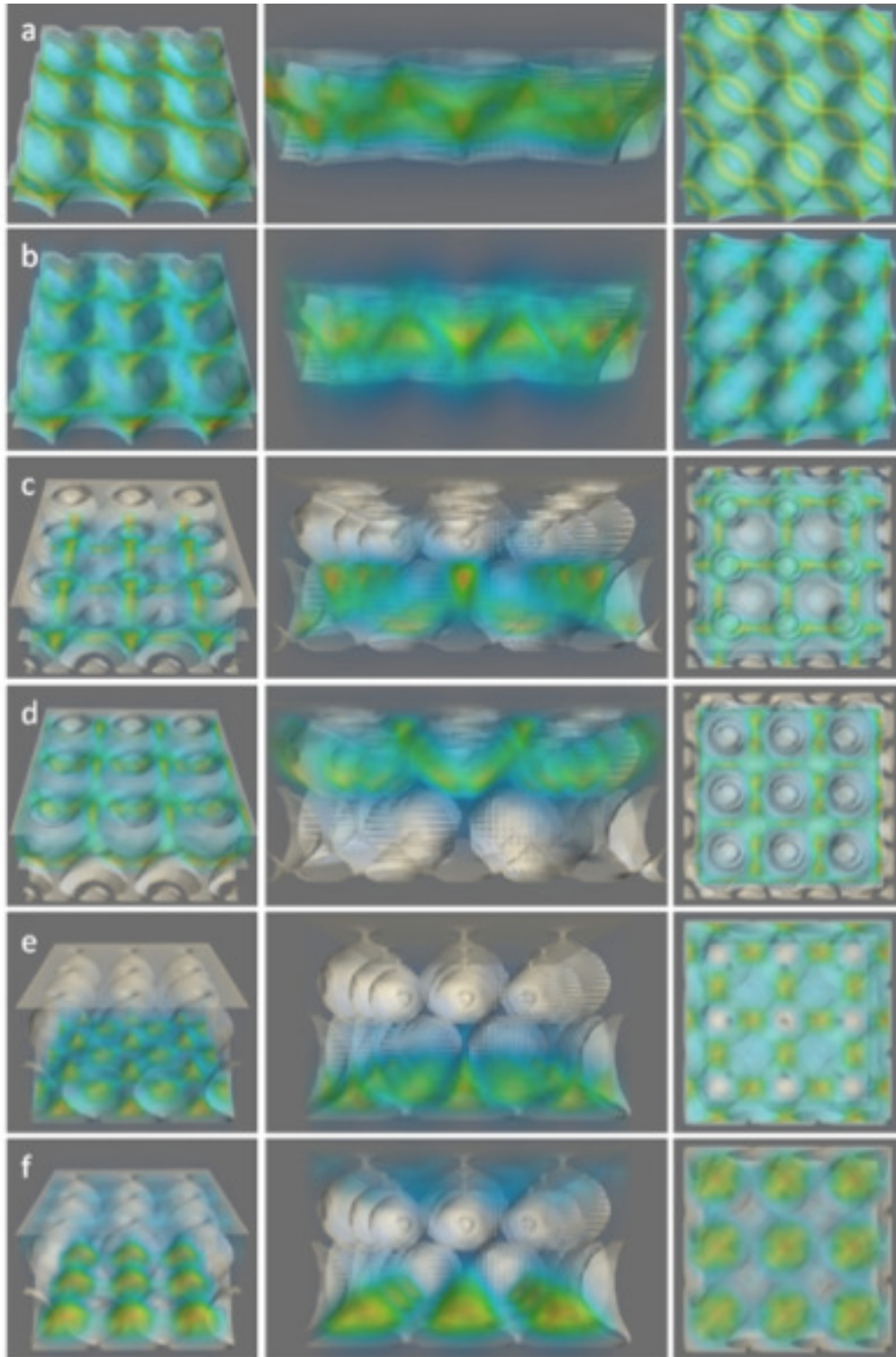


Figure 3.7: Displacement field (given by dielectric constant electric field) at the M symmetry point for inverted buckled structures at  $\epsilon_c = 14.6$ : hemisphere (a) 4th band, (b) 5th band; 50%r mushroom cap (c) 4th band, (d) 5th band; and sphere (e) 4th band, (f) 5th band.

gaps, the degree of buckling was altered to span  $w/l$  values from  $\sqrt{3r^2 - (r - r_{in})^2}/r$  (i.e., monolayer values 1.41 – 1.73) to 1.0 (square bilayer). The gap widths for the 4 – 5 gap in the inverted hemisphere system are shown in Figure 3.6(a) as a function of  $w/l$ . The error threshold was exceeded for  $w/l$  values from 1.03 to 1.07, with the maximum gap size achieved at an intermediate  $w/l$  value of 1.05. Of the arrangements investigated, this range reflects structures approaching higher lattice symmetry. The gap closed at larger rectangular aspect ratios beyond 1.07 due to the shift of band 5 to lower frequencies at the  $X'$ -point. For  $w/l$  less than 1.03, the width of the gap falls below significance due to a degeneracy between the  $\Gamma$ - and  $M$ -points. The gap opened at lower dielectric contrast values as the degree of buckling increased ( $w/l$  decreased). The 12 – 13 gap in the inverted mushroom cap structure ( $r_{in} = 50\%r$ ) occurred at an even smaller rectangular aspect ratio ( $w/l < 1.03$ ), as compared to the hemisphere case. Again, the tolerance for lattice anisotropy was limited due to a degeneracy near the  $X'$ -point. The minimum refractive index contrast to open the 12 – 13 gap increased with lattice distortion (Figure 3.6(c)). The gap widened as the rectangular aspect ratio decreased to unity. The results suggest that the basis shape collapse from mushroom cap to the even less isotropic hemisphere is better accommodated on a reduced symmetry lattice (i.e., band gaps exist over a wider range of  $w/l$  values).

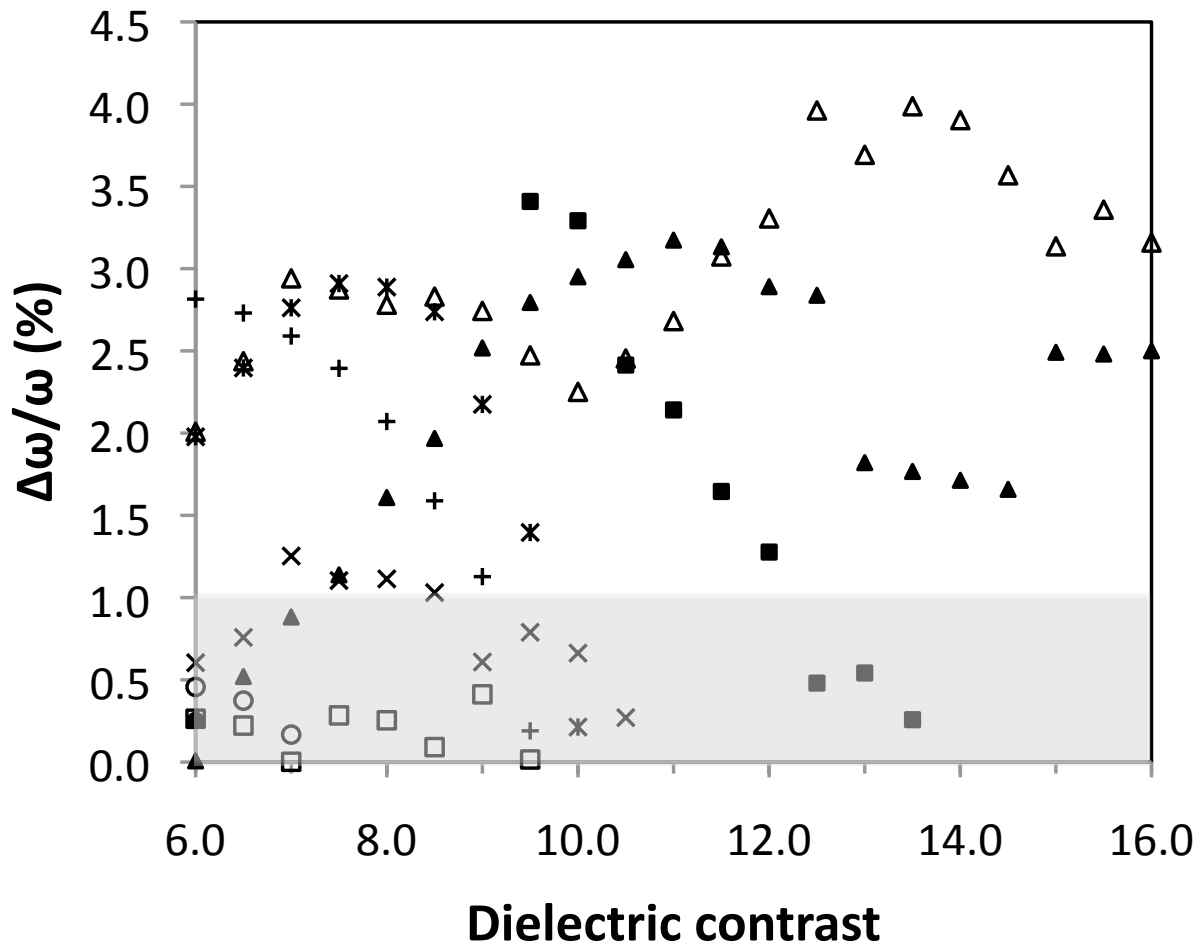


Figure 3.8: 12 – 13 band gap in square bilayer as a function of the toroid shape parameter:  $r_{in} = 0\%$ r (solid square),  $10\%$ r (open square),  $20\%$ r (solid circle),  $30\%$ r (open circle),  $40\%$ r (solid triangle),  $50\%$ r (open triangle),  $60\%$ r (cross),  $70\%$ r (asterisk), and  $90\%$ r (plus).

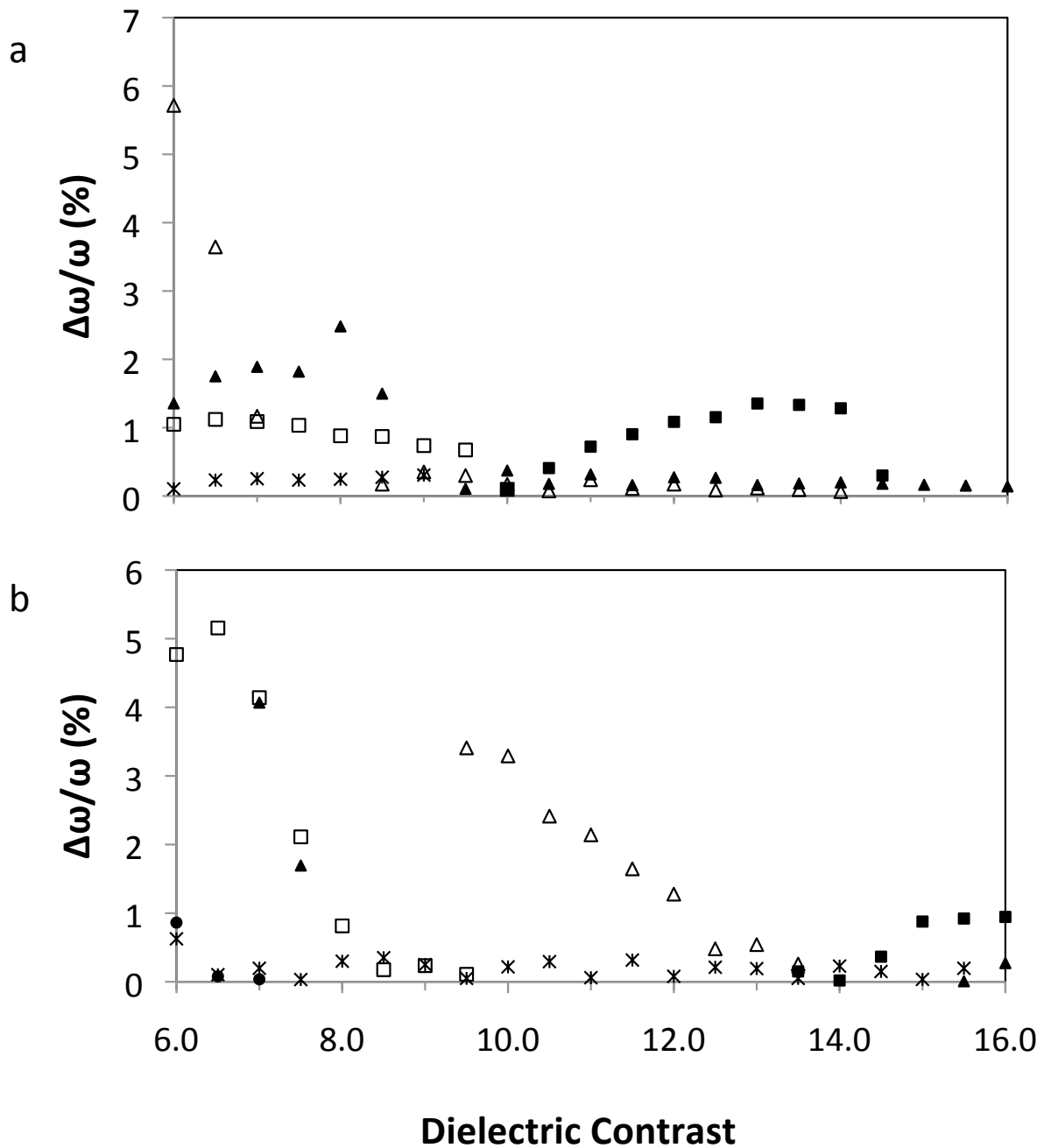


Figure 3.9: a) 14 – 15 gap and b) 16 – 17 gap in square bilayer structures as a function of toroid shape parameter:  $r_{in} = 0\%$  (solid square),  $10\%$  (open square),  $40\%$  (solid triangle),  $50\%$  (open triangle),  $70\%$  (asterisk) and  $100\%$  (solid circle).

The reduction of the rectangular aspect ratio to 1.0 (the square bilayer) affects both the lattice symmetry and the coordination number in the structures. In the square bilayer, the lattice symmetry increases to a four-fold rotational symmetry ( $p4mm$ ) and the coordination number increases from 6 to 8. The dielectric filling fraction (Figure 3.5(b)) is also minimized for all shapes. As indicated in Figure 3.6(a), the 4 – 5 gap has value less than 1% in the inverted square bilayer of hemispheres. That the lowest gap depends on the coordination number or connectivity to open agrees with findings for amorphous diamond and the A7 family of structures.[8, 4] Rectangular lattice symmetry that favors the gap opening contrasts with the opposing trend found for several circular cross-section pore structures.[35, 41] In rectangular systems of nonspherical motifs, gap formation has been promoted by scatterer shapes aligned in-plane along the direction of lattice extension.[35, 41, 32] Here, the particle anisotropy in the vertical direction makes the basis shape compatible with the lower lattice symmetry and encourages gap formation.

The square bilayer supported several additional band gaps. The evolution of the 12 – 13, 14 – 15, and 16 – 17 gaps found in the inverted square bilayer as a function of the toroid shape parameter and dielectric contrast is shown in Figures 3.8 and 3.9. The 12 – 13 gap persisted over the widest range of dielectric contrasts for the filling fraction local minimum at shape parameter 50% $r$  (Figure 3.5(b)). Examination of lower dielectric contrast values for this structure revealed that the gap opened between dielectric contrasts of 5.5 and 6.0. The 12 – 13 gap at a dielectric contrast of 10 is limited between  $\Gamma$  and  $M$  near the light cone edge for 0% $r$ , the hemisphere case. A degeneracy between  $\Gamma$  and  $M$  developed for 10% $r$  – 30% $r$  and lifted for 40% $r$  – 70% $r$ , where the gap size was often controlled by the lower band edge near  $X'$  and by the upper band near the  $\Gamma$  –  $M$  light cone edge. The particle shape contributed to modulation of the bands such that the gap opened for low filling fractions (Figure 3.5(b)). As the shape parameter increased past 70% $r$  ( $f = 33.7\%$ ) approaching a spherical basis shape, the gap closed. The structure

based on the inverted horn mushroom caps (50%*r*) exhibited the largest 14 – 15 gap at 5.72% (Figure 3.9(a)). The guided modes are restricted at higher frequency by the light cone to wavevectors not spanning the full Brillouin zone ( $X' - \Gamma - X$  region excluded). These gaps are marked with an asterisk in Table 3.5, which details the largest gaps in the structures having particle tangency enforced.

Additionally, gap competition characteristics, where gaps of certain indices are maximized at the expense of gaps having other indices, were apparent in the square bilayer structures. This is illustrated in the hemisphere (0%*r*) case considering the 6 – 7, 8 – 9, and 14 – 15 gaps in Figure 3.10(a). Whether the gaps could be formed between higher lying bands depended on lattice symmetry. However, the basis shape strongly influenced the index of the principle gaps.[28] For example, in Figure 3.10, the band indices of the principal high lying gap, 16 – 17 (Figure 3.10(b)), shifted to 14 – 15 (Figure 3.10(d)), and further to 12 – 13 (Figure 3.10(e)) as the basis shape became more isotropic. Notably, the dielectric filling in many of the structures possessing gaps was less than 34%. Only the square bilayer arrangements yielded gaps associated with filling fractions up to 37% (for basis shapes 80%*r* and 90%*r*).

The inverted structures discussed to this point have inherent differences in filling fraction due to basis shape variations. The dielectric filling was also manipulated independently of underlying particle morphology by sampling particle radii not consistent with tangency in the set configurations. An inverted buckled hemisphere structure ( $w/l = 1.02$ ) was modeled at a dielectric contrast of 13.7 with ‘air’ particle radius ranging from  $r = 0.50$  (tangent) to  $r = 0.40$  (isolated pore shapes in the matrix). The 4 – 5 gaps present in the tangent case were not found at reduced *r* values. For the inverted mushroom cap systems, 8 – 9 gaps arose at an intermediate radius of 0.46 for the 50%*r* and 60%*r* shape parameters ( $f = 45.2\%$  and  $45.9\%$ ). The structure based on the 40%*r* toroid shape pa-

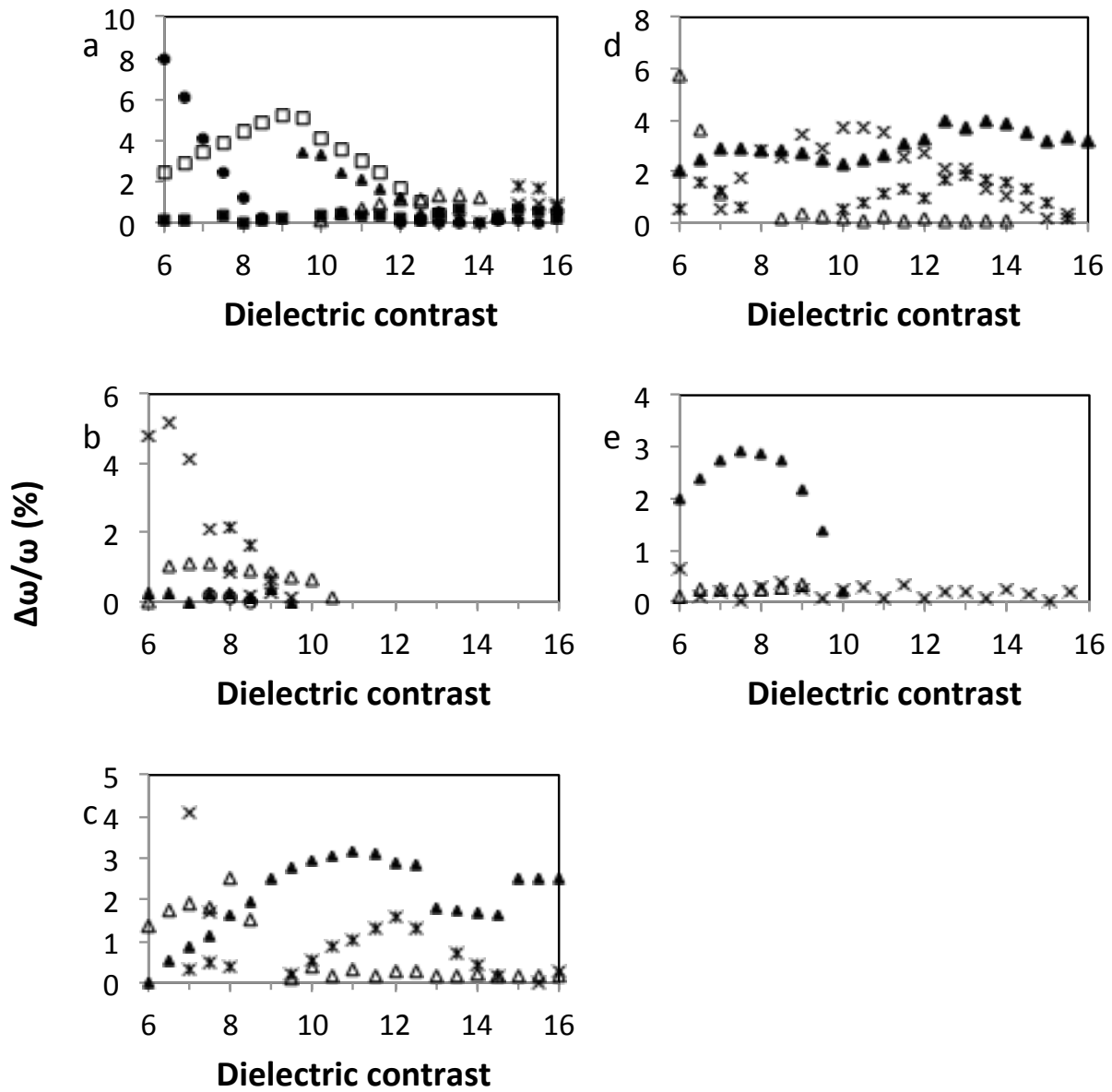


Figure 3.10: Band gaps for inverted square bilayer structures with toroid shape parameters: a) 0%r (hemisphere), b) 10%r, c) 40%r, d) 50%r and e) 70%r. Gap index values: 4 – 5 gap (closed square), 6 – 7 gap (open square), 8 – 9 gap (closed circle), 10 – 11 gap (open circle), 12 – 13 gap (closed triangle), 14 – 15 (open triangle), 16 – 17 gap (cross) and 18 – 19 gap (asterisk).

parameter exhibited a 12 – 13 gap at  $r = 0.46$  ( $f = 45.6\%$ ), but favorably required a lower dielectric contrast than in the tangent case to achieve the same gap width. The 12 – 13 gap achieved the threshold value as the ‘air’ particle radius was increased from 0.44 to 0.46. Reducing the size of the air voids thickens the matrix dielectric and raises filling fractions beyond those allowed in the gap-supporting structures having tangent voids. When the radius of the negative particle was extended beyond the tangent condition (up to  $r = 0.58$ ), significantly overlapping enlarged air voids, no gaps were produced for the 40 %r–60 %r mushroom cap systems.

The direct buckled structures at the rectangular aspect ratio 1.02 yielded a single gap index in the dielectric contrast range from 6.0 to 16.0 for the tangent condition. Gaps between the 14th and 15th bands were found in the hemisphere based structures for  $\epsilon_c$  from 13 to 15 (Figure 3.11(a)). There were no band gaps in the mushroom cap (filling fraction range 65.4% to 73.3%) or spherical ( $f = 62.0\%$ ) systems. Figures 3.11(b) and 3.11(c) shows band diagrams of the mushroom cap and sphere based structures. The higher bands are compressed to lower frequency extinguishing any gaps.

Tables 3.1 and 3.2 along with the contour map in Figure 3.12 summarize the largest gaps for the buckled and bilayer structures examined. Often, the size of band gaps in slab photonic crystals is maximized by adjusting the slab height.[18] The lattice distortion dependence on the slab height mandates a structural change in the context of the present study. The variables are not decoupled and thus no separate height optimization was performed. The full band gaps however could potentially be enlarged utilizing cladding layers surrounding the slab to modify the light cone that in several cases is the limiting feature on gap size in the band structure diagram.[18] Slab applications where full gaps rather than partial gaps would be desirable include the design of resonant cavities to suppress resonance at harmonic frequencies in the case of multiple full gaps,[29] as well

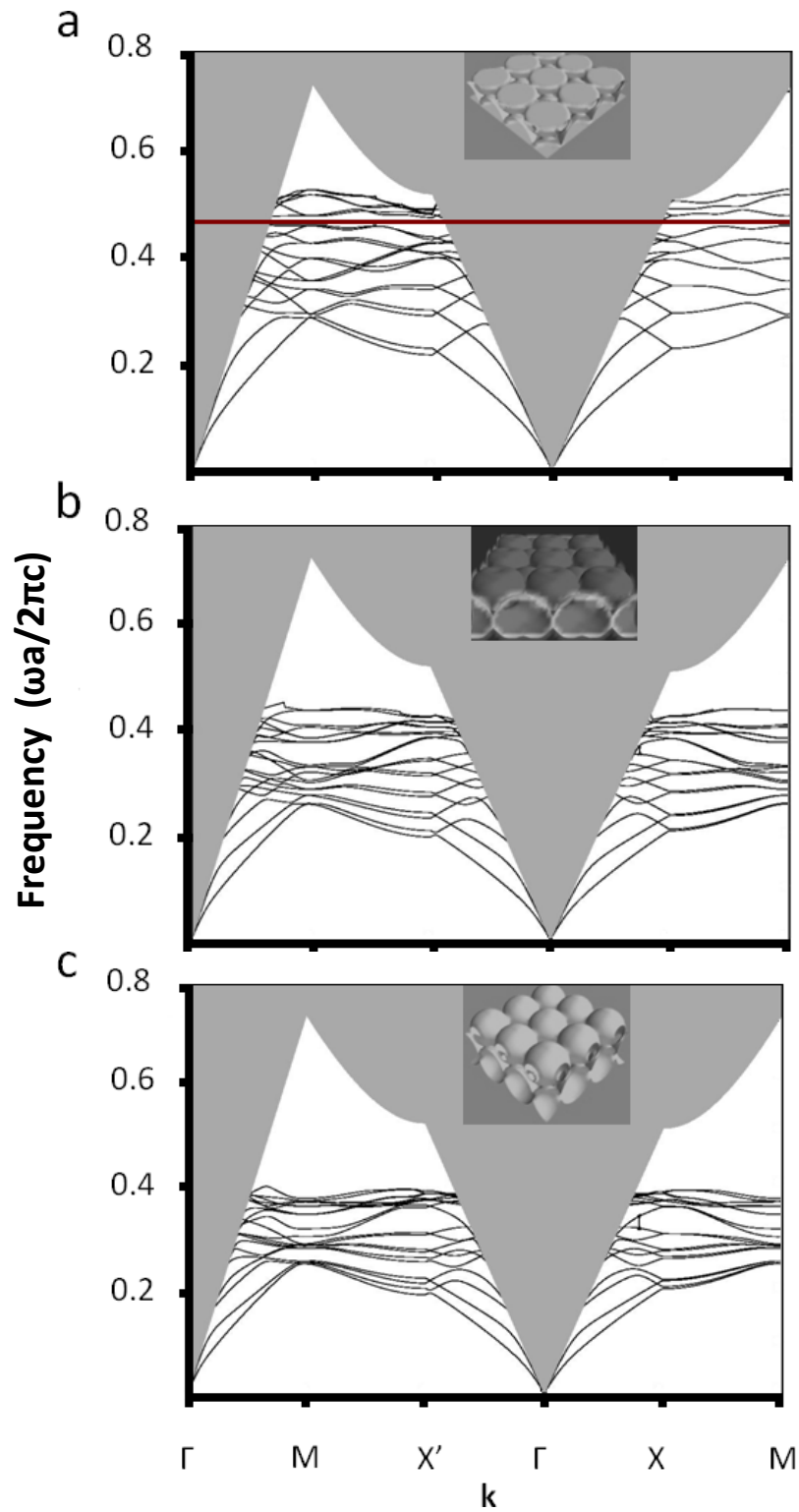


Figure 3.11: Band diagrams of direct buckled structures with  $w/l = 1.02$  and  $\epsilon_c = 14.0$ . (a) hemisphere ( $f = 73.7\%$ ); (b) mushroom cap,  $r_{in} = 50\%r$  ( $f = 68.0\%$ ); and (c) sphere ( $f = 62.0\%$ ).

Table 3.1: Largest gaps in tangent structures. Asterisks mark gaps restricted in wavevector range; e.g.,  $X' - \Gamma - X$  band structure region excluded by light cone.

Structure	Gap index	$r$	$w/l$	$r_{in}(\%r)$	$\epsilon_c$	$\Delta\omega/\omega(\%)$	$f(\%)$
Inverted	4 – 5	0.50	1.07	0	16.0	1.65	28.2
	4 – 5	0.50	1.06	0	15.0	1.30	27.9
	4 – 5	0.50	1.05	0	15.0	2.80	27.5
	4 – 5	0.50	1.03	0	14.0	2.03	27.1
	12 – 13	0.50	1.02	40	16.0	2.28	32.2
	12 – 13	0.50	1.02	50	13.7	3.20	32.0
	12 – 13	0.50	1.02	60	12.0	1.69	33.1
	6 – 7	0.50	1.00	0	9.0	5.24*	26.0
	8 – 9	0.50	1.00	0	6.0	7.93*	26.0
	12 – 13	0.50	1.00	50	13.5	3.99	31.1
	14 – 15	0.50	1.00	50	6.0	5.72*	31.1
	16 – 17	0.50	1.00	10	6.5	5.16*	32.4
	18 – 19	0.50	1.00	10	8.0	2.19*	32.4
Direct	14 – 15	0.50	1.02	0	13.7	2.07	73.3

Table 3.2: Largest gaps in non-tangent structures when particle radius was reduced from 0.50 (tangent) to 0.40.

Structure	Gap index	$r$	$w/l$	$r_{in}(\%r)$	$\epsilon_c$	$\Delta\omega/\omega(\%)$	$f(\%)$
Inverted	8 – 9	0.46	1.02	50	13.7	1.41	45.2
	8 – 9	0.46	1.05	50	13.7	2.07	46.2
	8 – 9	0.46	1.02	60	13.7	1.57	45.9
	12 – 13	0.46	1.07	40	13.7	1.63	47.3

as multilayer solar cell designs for energy harvesting and nonlinear optics application,[1, 17] where light intensity would be significantly diminished when limited to applying polarized light. Also, use in light extraction from slabs with internal sources that emit in both polarizations would be advantageous for out-coupling.[42]

Materials structured as modeled in this work could be realized via a number of routes—confinement self-assembly using suspensions of PS colloids in hydrolyzed metalalkoxide precursor that deposit ceramic material from gel upon drying,[11] adding semiconductor nanoparticles to PS particle suspensions for co-assembly under confinement,[21] or more traditionally backfilling preformed buckled films by chemical (physical) vapor deposition and atomic layer deposition.[22, 37] Considering other related systems for perspective, we note a full band gap in the wavelength range from 1280 nm to 1325 nm was identified for a Si PC slab with thickness of 320 nm, prepared by electron-beam lithography and reactive reactive ion etching of triangular cross-section air holes on a triangular lattice.[38] Calculations indicated adjusting lattice aspect ratio from the triangular lattice setting (1.732) to 2.3 and the pore ellipticity (major-to-minor axis radius ratio) to 1.78 in a 320 nm thick Si slab embodiment for elliptical cross-section holes produced an optimum gap of 5.2% as compared to 3.1% for elliptical motifs on the triangular lattice.[32] Moreover, slab structures where scatter shape was modified in directions out-of-plane with respect to the substrate, yielded only even mode gaps for rutile  $TiO_2$  colloidal spheres ( $r = 165$  nm and  $\epsilon_c = 8.41$ ) in a honeycomb lattice and also for dumbbell pores on a triangular lattice made by photo-electrochemical etch.[40, 15]

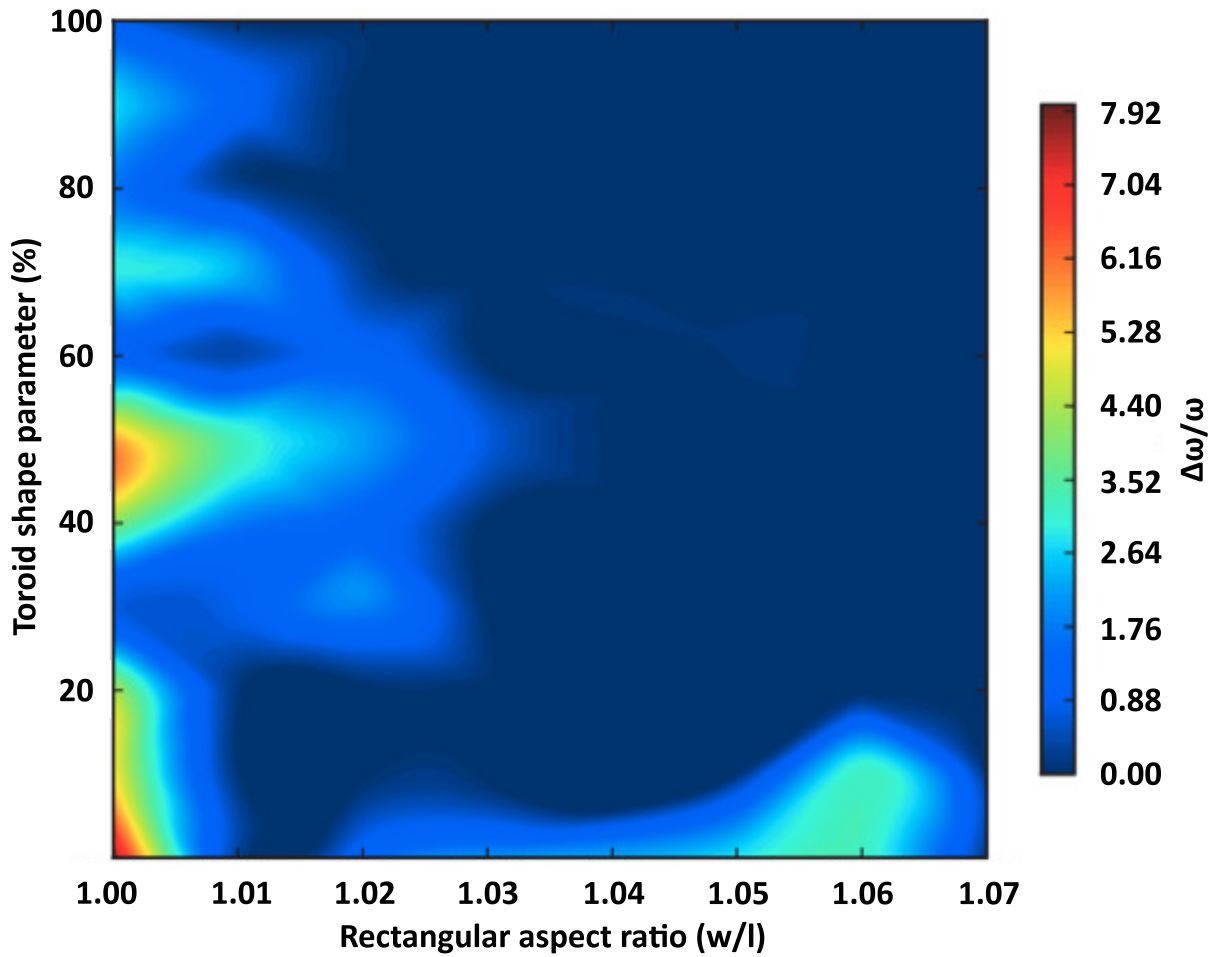


Figure 3.12: Contour map of the largest gaps for inverted structures with toroid shape parameter varied from hemisphere ( $r_{in} = 0\%r$ ) to sphere ( $r_{in} = 100\%r$ ) and aspect ratio adjusted from rectangular ( $w/l = 1.07$ ) to square ( $w/l = 1.00$ ).

### 3.5 Conclusions

There has been a recent concentration on the fabrication of diverse self-assembled structures beyond closepacked spheres and much mention of application in photonics.[7, 5, 10, 24, 23] The present study addresses the relative void in actual prediction of properties in particle-based slab photonic systems. The guided modes of a photonic slab with structural variation out-of-plane were studied in light of experimental observations of buckled photonic crystals and envisioning their use as PC slab templates. The particle toroid shape parameter and the degree of buckling were independently varied to promote gaps between the 4th and 5th bands and the 12th and 13th bands in the inverted system. The influence of dielectric filling fraction generated gaps between the 8th and 9th bands for inverted structures relaxed from tangency. Gaps that arose for the direct structures formed between the 14th and 15th bands. The most symmetric lattice, square bilayer arrangement, promoted gaps in even higher lying bands. Particles of nontrivial shape were preferred in buckled structures where lattice distortion could be compensated with increasing particle anisotropy (shape distortion). The band indices of the principle photonic band gaps strong correlation to specific particle morphologies.

### 3.6 Acknowledgments

We gratefully acknowledge funding of this work by the National Science Foundation (Career Award Nos. DMR- 0547976 and DMR-1105243). E.K.R. thanks the National Science Foundation and the Department of Defense for fellowship awards.

### 3.7 Appendix: Synthesis Procedures

PS spheres were synthesized via emulsion polymerization. 100 mL of absolute ethanol and 40 mL of deionized water were combined in a 250 mL glass media bottle. 146.6 mg of electrophoresis grade sodium dodecyl sulfate (SDS) and 133.4 mg 99.99 % potassium persulfate (KPS) were added and the solution was stirred via magnetic stir bar until dissolution was complete. The bottle was placed in a glycerol bath at 70 °C with continuous stirring and 6 mL of monomer [ $\geq$  99 % styrene and 55 % DVB (Aldrich)] were injected. The mixture was left to stir at temperature for 24 h after which the product was cooled under running water and refrigerated. A 2 % DVB batch was prepared with monomer composition of 5.880 mL styrene and 120  $\mu$ L DVB. SDS was purchased from Fisher and all other reagents were purchased from Sigma-Aldrich.

To obtain the non-spherical morphology of the final particles, seed particles were swelled with monomer and polymerized at elevated temperatures in a shaker bath. 0.5 mg of seed particle suspension was pipetted into a 50 mL centrifuge tube and the solid polymer seeds were removed from suspension via centrifugation. The seeds were resuspended via sonication in 2 mL of poly(vinylalcohol) (PVA, 87 %–89 % hydrolyzed, Sigma-Aldrich) solution [1 g PVA ( $MW = 85000$ – $124000$ )/9 mL deionized water] along with 5 mg of hydroquinone (99 %, Acros). A second solution was made by dissolving 75 mg V65B initiator [2,2'-Azobis(2.4-dimethyl valeronitrile), Wako] in 2.5 mL of monomer and adding 1 mL 99.8 % toluene anhydrous (Sigma-Aldrich) along with 4 mL PVA solution before homogenization for 1 min. The monomer composition of styrene and DVB ranged from 0.125 mL DVB with 2.375 mL styrene for 5 % DVB particles to 0.75 mL DVB with 1.75 mL styrene for 30 % DVB particles. The second solution was rinsed into the centrifuge tube containing the seeds using 5 mL of PVA solution. The tube was subsequently set on a tumbling rack for 24 h. The mixture was transferred to a 25 mL reaction vial and

purged for 1 min with nitrogen gas and sealed with a cap and teflon tape. The reaction vial was clipped into the shaker bath and polymerization occurred at 70 °C and 120 rpm for 24 h. The vessel was cooled under running water.

## REFERENCES

- [1] Shrestha Basu Mallick, Nicholas P. Sergeant, Mukul Agrawal, Jung-Yong Lee, and Peter Peumans. Coherent light trapping in thin-film photovoltaics. *MRS Bull.*, 36(06):453–460, June 2011.
- [2] C. G. Bostan and R. M. de Ridder. Design of photonic crystal slab structures with absolute gaps in guided modes. *J. Opt. Adv. Mat.*, 4:921–928, 2002.
- [3] Julie A. Champion, Yogesh K. Katare, and Samir Mitragotri. Particle shape: A new design parameter for micro- and nanoscale drug delivery carriers. *J. Controlled Release*, 121(1-2):3–9, August 2007.
- [4] C.T. Chan, S. Datta, K.M. Ho, and C.M. Soukoulis. A7 structure: A family of photonic crystals. *Phys. Rev. B*, 50(3):1988–1991, July 1994.
- [5] Qian Chen, Sung Chul Bae, and Steve Granick. Directed self-assembly of a colloidal kagome lattice. *Nature*, 469(7330):381–384, January 2011.
- [6] Ruey-Lin Chern and Sheng D. Chao. Optimal higher-lying band gaps for photonic crystals with large dielectric contrast. *Opt. Express*, 16(21):16600–16608, October 2008.
- [7] Tao Ding, Kai Song, Koen Clays, and Chen-Ho Tung. Fabrication of 3D photonic crystals of ellipsoids: Convective self-assembly in magnetic field. *Adv. Mater.*, 21(19):1936–1940, 2009.
- [8] Keiichi Edagawa, Satoshi Kanoko, and Masaya Notomi. Photonic amorphous diamond structure with a 3D photonic band gap. *Phys. Rev. Lett.*, 100(1):013901, January 2008.
- [9] Marian Florescu, Salvatore Torquato, and Paul J. Steinhardt. Designer disordered materials with large, complete photonic band gaps. *Proc. Natl. Acad. Sci. U.S.A.*, 106(49):20658–20663, 2009.
- [10] Sumit Gangwal, Olivier J. Cayre, and Orlin D. Velev. Dielectrophoretic assembly of metallodielectric janus particles in AC electric fields. *Langmuir*, 24(23):13312–13320, December 2008.
- [11] Benjamin Hatton, Lidiya Mishchenko, Stan Davis, Kenneth H. Sandhage, and Joanna Aizenberg. Assembly of large-area, highly ordered, crack-free inverse opal films. *Proc. Natl. Acad. Sci. U.S.A.*, 107(23):10354–10359, 2010.

- [12] Kevin P. Herlihy, Janine Nunes, and Joseph M. DeSimone. Electrically driven alignment and crystallization of unique anisotropic polymer particles. *Langmuir*, 24(16):8421–8426, August 2008.
- [13] C.J. Hernandez and T.G. Mason. Colloidal alphabet soup: Monodisperse dispersions of shape-designed LithoParticles. *J. Phys. Chem. C*, 111(12):4477–4480, March 2007.
- [14] I. D. Hosein and C. M. Liddell. Convectively assembled nonspherical mushroom cap-based colloidal crystals. *Langmuir*, 23(17):8810–8814, 2007.
- [15] C. Jamois, R.B. Wehrspohn, J. Schilling, F. Muller, R. Hillebrand, and W. Hergert. Silicon-based photonic crystal slabs: two concepts. *IEEE J. Quant. Electron.*, 38(7):805–810, 2002.
- [16] Lin Jia, Ion Bitá, and Edwin L. Thomas. Photonic density of states of two-dimensional quasicrystalline photonic structures. *Phys. Rev. A*, 84(2):023831, August 2011.
- [17] Sajeev John and Neşet AközbeK. Nonlinear optical solitary waves in a photonic band gap. *Phys. Rev. Lett.*, 71(8):1168–1171, August 1993.
- [18] Steven G. Johnson, Shanhui Fan, Pierre R. Villeneuve, J. D. Joannopoulos, and L. A. Kolodziejski. Guided modes in photonic crystal slabs. *Phys. Rev. B*, 60(8):5751–5758, August 1999.
- [19] Steven G. Johnson and John D. Joannopoulos. Block-iterative frequency-domain methods for maxwell’s equations in a planewave basis. *Opt. Express*, 8(3):173–190, 2001.
- [20] Jin-Woong Kim and Kyung-Do Suh. Monodisperse polymer particles synthesized by seeded polymerization techniques. *J. Ind. Eng. Chem.*, 14(1):1 – 9, 2008.
- [21] Vladimir Kitaev and Geoffrey A. Ozin. Self-assembled surface patterns of binary colloidal crystals. *Adv. Mater.*, 15(1):75–78, 2003.
- [22] M. Knez, K. Nielsch, and L. Niinistö. Synthesis and surface engineering of complex nanostructures by atomic layer deposition. *Adv. Mater.*, 19(21):3425–3438, November 2007.
- [23] Fan Li, David P. Josephson, and Andreas Stein. Colloidal assembly: The road from particles to colloidal molecules and crystals. *Angew. Chem., Int. Ed.*, 50(2):360–388, January 2011.

- [24] Xiaofeng Li, Liang Zhang, Yongxin Wang, Xiaoli Yang, Ning Zhao, Xiaoli Zhang, and Jian Xu. A bottom-up approach to fabricate patterned surfaces with asymmetrical TiO<sub>2</sub> microparticles trapped in the holes of honeycomblike polymer film. *J. Am. Chem. Soc.*, 133(11):3736–3739, March 2011.
- [25] E. Lidorikis, M. M. Sigalas, E. N. Economou, and C. M. Soukoulis. Gap deformation and classical wave localization in disordered two-dimensional photonic-band-gap materials. *Phys. Rev. B*, 61(20):13458, 2000.
- [26] C. López. Materials aspects of photonic crystals. *Adv. Mater.*, 15(20):1679–1704, 2003.
- [27] Martin Maldovan. *Periodic materials and interference lithography: for photonics, phononics and mechanics*. Wiley-VCH, Weinheim, October 2008.
- [28] Martin Maldovan, Chaitanya K. Ullal, W. Craig Carter, and Edwin L. Thomas. Exploring for 3D photonic bandgap structures in the 11 f.c.c. space groups. *Nature Mater.*, 2(10):664–667, September 2003.
- [29] H. Men, N. C. Nguyen, R. M. Freund, K. M. Lim, P. A. Parrilo, and J. Peraire. Design of photonic crystals with multiple and combined band gaps. *Phys. Rev. E*, 83(4):046703, April 2011.
- [30] Eric B. Mock and Charles F. Zukoski. Determination of static microstructure of dilute and concentrated suspensions of anisotropic particles by ultra-small-angle x-ray scattering. *Langmuir*, 23(17):8760–8771, August 2007.
- [31] Ali Mohraz and Michael J. Solomon. Direct visualization of colloidal rod assembly by confocal microscopy. *Langmuir*, 21(12):5298–5306, June 2005.
- [32] Kris Ohlinger, Yuankun Lin, and Jeremy S. Qualls. Maximum and overlapped photonic band gaps in both transverse electric and transverse magnetic polarizations in two-dimensional photonic crystals with low symmetry. *J. Appl. Phys.*, 106(6):063520, 2009.
- [33] Masayoshi Okubo and Hideto Minami. Production of micron-sized monodispersed anomalous polymer particles having red blood corpuscle shape. *Macromol. Symp.*, 150(1):201–210, February 2000.
- [34] L Pauchard and Y Couder. Invagination during the collapse of an inhomogeneous spheroidal shell. *Europhys. Lett.*, 66(5):667–673, June 2004.

- [35] Min Qiu and Sailing He. Large complete band gap in two-dimensional photonic crystals with elliptic air holes. *Phys. Rev. B*, 60(15):10610–10612, October 1999.
- [36] E. K. Riley and C. M. Liddell. Confinement-controlled self assembly of colloids with simultaneous isotropic and anisotropic cross-section. *Langmuir*, 26(14):11648–11656, 2010.
- [37] Andreas Stein, Fan Li, and Nicholas R. Denny. Morphological control in colloidal crystal templating of inverse opals, hierarchical structures, and shaped particles †. *Chem. Mater.*, 20(3):649–666, February 2008.
- [38] Sei-ichi Takayama, Hitoshi Kitagawa, Yoshinori Tanaka, Takashi Asano, and Susumu Noda. Experimental demonstration of complete photonic band gap in two-dimensional photonic crystal slabs. *Appl. Phys. Lett.*, 87(6):061107, 2005.
- [39] Zhenquan Tan, Akito Masuhara, Hitoshi Kasai, Hachiro Nakanishi, and Hidetoshi Oikawa. Multibranched c 60 Micro/Nanocrystals fabricated by reprecipitation method. *Jpn. J. Appl. Phys.*, 47(2):1426–1428, February 2008.
- [40] Kevin Vynck, David Cassagne, and Emmanuel Centeno. Superlattice for photonic band gap opening in monolayers of dielectric spheres. *Opt. Express*, 14:6668–6674, 2006.
- [41] Rongzhou Wang, Xue-Hua Wang, Ben-Yuan Gu, and Guo-Zhen Yang. Effects of shapes and orientations of scatterers and lattice symmetries on the photonic band gap in two-dimensional photonic crystals. *J. Appl. Phys.*, 90(9):4307, 2001.
- [42] Feng Wen, Sylvain David, Xavier Checoury, Moustafa El Kurdi, and Philippe Boucaud. Two-dimensional photonic crystals with large complete photonic band gaps in both TE and TM polarizations. *Opt. Express*, 16(16):12278–12289, 2008.
- [43] Seung-Man Yang, Shin-Hyun Kim, Jong-Min Lim, and Gi-Ra Yi. Synthesis and assembly of structured colloidal particles. *J. Mater. Chem.*, 18(19):2177, 2008.
- [44] Y. Yin and Y. Xia. Self-assembly of monodispersed spherical colloids into complex aggregates with well-defined sizes, shapes, and structures. *Adv. Mater.*, 13(4):267–271, February 2001.
- [45] Xuelian Zhu, Ying Zhang, Dinesh Chandra, Shih-Chieh Cheng, James M. Kikkawa, and Shu Yang. Two-dimensional photonic crystals with anisotropic unit cells imprinted from poly(dimethylsiloxane) membranes under elastic deformation. *Appl. Phys. Lett.*, 93(16):161911, 2008.

## CHAPTER 4

### SLAB PHOTONIC CRYSTALS WITH DIMER COLLOID BASES\*

#### 4.1 Abstract

The photonic band gap properties for centered rectangular monolayers of asymmetric dimers is reported. Colloids in suspension have been organized into the phase under confinement. The theoretical model is inspired by the range of asymmetric dimers synthesized via seeded emulsion polymerization and explores, in particular, the band structures as a function of degree of lobe symmetry and degree of lobe fusion. These parameters are varied incrementally from spheres to lobe-tangent dimers over morphologies yielding physically realizable particles. The work addresses the relative scarcity of theoretical studies on photonic crystal slabs with vertical variation that is consistent with colloidal self-assembly. Odd, even and polarization independent gaps in the guided modes are determined for direct slab structures. A wide range of lobe symmetry and degree of lobe fusion combinations having Brillouin zones with moderate to high isotropy support gaps between odd mode band indices 2-3 and even mode band indices 1-2 and 2-3.

---

\*To be published as: Erin K. Riley and Chekesha M. Liddell Watson. "Slab Photonic Crystals with Dimer Colloid Bases", *J Appl Phys*, recommended for publication (2014).

## 4.2 Introduction

Photonic crystals provide an approach to design structures with unusual dispersion properties such as band gaps, slow light and negative refraction.[18, 32] The properties have been applied in integrated optical chips; filters; waveguides and resonators; sub-diffraction limit planar lenses; and biological sensors. Applications were conceptualized requiring dielectric periodicity in three dimensions (3D). However, 3D light confinement can be more readily attained in experiment using planar waveguide techniques such as microlithography. In these structures the electromagnetic fields are controlled in-plane through the photonic crystal patterning and out-of-plane via index guiding.[18] Characterizing the photonic properties is well understood from an analytical perspective, but the inverse problem of designing a material from a property template remains.

Both an appropriate periodic structure and a fabrication method consistent with the scale and feature complexity must be available to construct a slab photonic crystal. Empirical rules and geometric considerations have established circular cross-section pores on triangular and square lattices as structures promoting photonic band gaps.[20] Recent theoretical work suggests that more complex photonic designs encourage gap creation.[48, 5, 30] For example, a tri-ellipse motif (i.e., 3-overlapping elliptical cross-section holes, mutually at  $120^\circ$ ) on a triangular lattice lifted degeneracy at the K-symmetry point and led to a polarization independent gap size of 11 % (gap-to-midgap ratio,  $\Delta\omega/\omega$ ). [46]

Lowering the photonic crystal symmetry can increase the design challenge for fabrication approaches. As the feature complexity increases, holographic lithography requires a more involved optical set up of the interference pattern. Methods for reduced feature size also require costly instrumentation and time consuming serial writing of elements using

electron beam lithography, direct laser writing, or micromachining by focused ion beams. Stitching errors and imprecise vertical alignment in large area ( $150\ \mu\text{m} \times 150\ \mu\text{m}$ ) fabrication using electron beam lithography can occur. Tapered sidewall asymmetry breaks the out-of-plane dielectric uniformity enabling coupling between even and odd modes and propagation losses up to  $0.5\ \text{dB mm}^{-1}$ . [41] Large area and parallel processed features can be formed through elastic deformation and wrinkling of solvent swollen polydimethylsiloxane membranes. Square, centered rectangular and rectangular lattices with an elliptical basis or combined circle and ellipse lattice features have been produced. [53] The structures required a delicate balance of external and internal stress and volume expansion to tailor the arrangement.

Colloidal self-assembly offers a large scale, low cost approach where the particles dimensions are determined by synthesis and the basis complexity can be controlled using particle morphology. High yield, monodisperse particle suspensions of many anisotropic shapes have become available (i.e., cubes; blood cell shapes; cylinders; hex nuts; hexagonal-, square-, triangular- and pentagonal prisms; spherocylinders; dumbbells; and asymmetric dimers.) [12, 34, 50, 7] Methods have produced large area, crack free monolayer and bulk colloidal crystals. [11, 2] Structural diversity and more open lattices have been achieved through physical templating, [51] binary co-assembly (size and charge), [6, 25] field-directed assembly [29, 8] and confinement assembly [23, 39, 24, 15]. Furthermore, thermodynamic simulations of asymmetric dimer and cut sphere particles demonstrate a range of self-organization. Translationally regular center-of-mass structures with uniform or random orientation (i.e., plastic crystal phases) as well as aperiodic crystals (i.e, degenerate crystals, DC) are stable in Monte Carlo simulations. [4, 47, 1] Such photonic solid phase structures including monolayer oblique, plastic crystal and DC phases have been experimentally realized by self-assembly of dimers and ‘mushroom caps’ under constrained height. [24, 16, 13, 39, 35] While synthesis and self-organization

techniques are maturing, the exploration of photonic properties for a rich variety of structures is still being pioneered.

Optical property characterization of reduced symmetry colloidal crystals has revealed complete 3D and slab band gaps, although studies have been limited.[13, 38] Few reports have addressed the effect of feature structuring in the third dimension for finite height slabs. For instance, calculations for rutile  $\text{TiO}_2$  colloidal spheres (dielectric contrast,  $\epsilon_c = 8.41$ ) in a honeycomb pattern (i.e.,  $6^3$  Schläfli symbol) predicted a 12.4% even mode gap.[43] Hour glass-shaped pores on a triangular lattice made by photoelectrochemical etch promoted a 10% even mode gap.[17] Moreover, a polarization independent gap of 7.9% was achieved for a mushroom cap-shaped basis on a rectangular lattice with out-of-plane buckling.[38]

The present work explores the photonic properties of an arrangement inspired by colloidal dimer self-assembly. Symmetry reduction through lattice distortion (i.e., centered rectangular) and basis shape led to large even and odd mode band gaps up to 14.7% and 19.3%, respectively. Multiple gaps (i.e., gaps exist at multiple sets of band indices) are promoted by the variation in lobe symmetry and degree of lobe fusion, dielectric contrast and fill fraction. A polarization independent gap size of 6.2% was found.

### 4.3 Computational Method

Asymmetric dimer particles have been synthesized by several groups using seeded emulsion polymerization of crosslinked polystyrene.[50, 31] Hydrophilic surface modification of the seeds encourages second stage monomer to dewet. The daughter lobes phase separate from the seed at elevated temperature.[24] Figure 4.1a illustrates several of the morphologies. The degree of lobe fusion and lobe symmetry are controlled through the

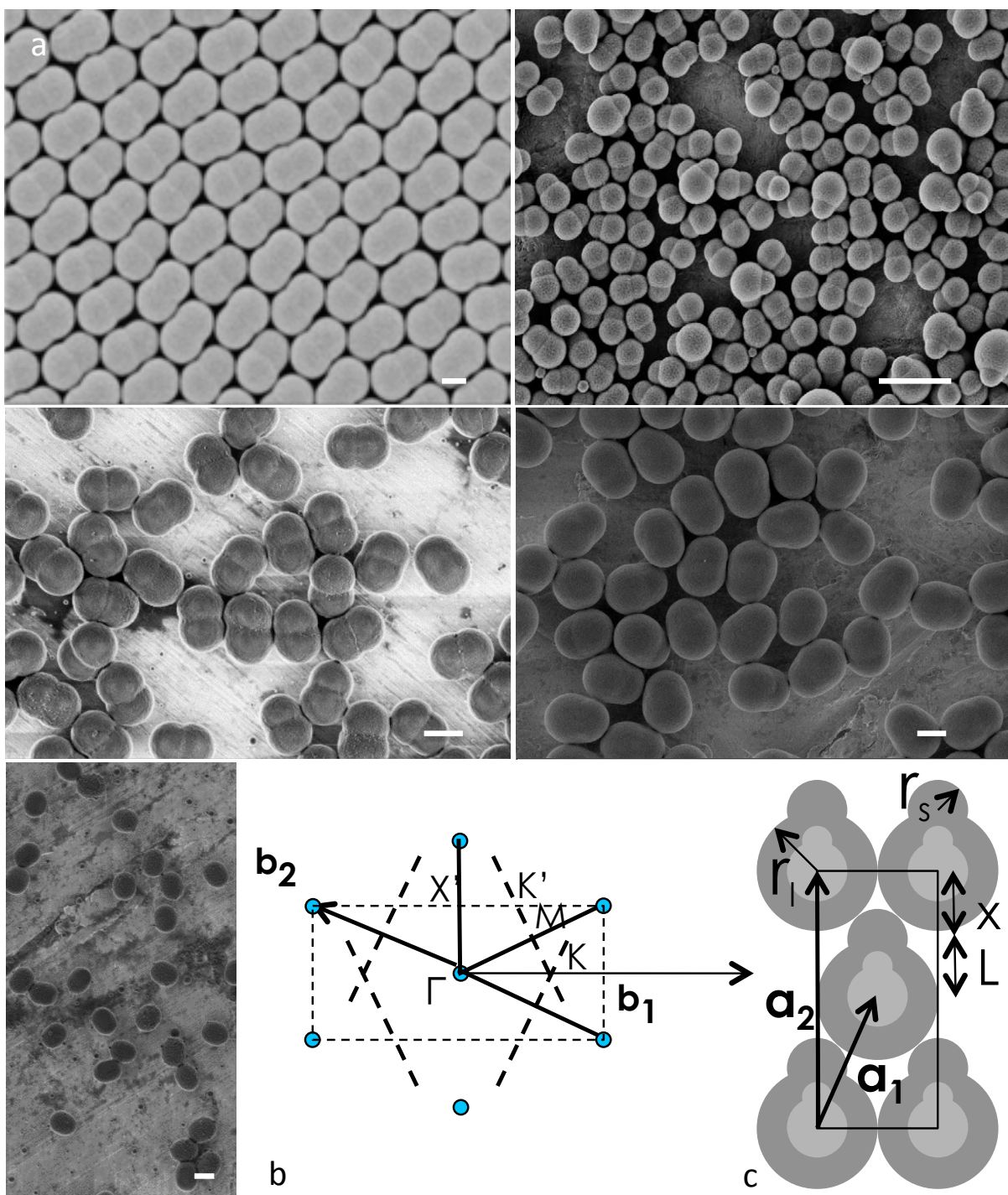


Figure 4.1: a) Scanning electron microscopy (SEM) images of asymmetric dimers. Scale bars are 1  $\mu\text{m}$ . b) Brillouin zone of the centered rectangular lattice with high symmetry points of irreducible Brillouin zone indicated. c) Schematic of modeled centered rectangular lattice with tangent asymmetric dimer basis (dark grey) and reduced filling fraction basis (light grey).

density of surface coverage, monomer-to-polymer swelling ratio and seed crosslinking density.

The asymmetric dimer shape was modeled as two overlapping spheres. Characteristic dimer shape parameters are quantified by the lobe symmetry parameter ( $S = r_s/r_l$ ) and the normalized bond length ( $L^* = L/2r_l$ , where  $L$  is the length between the lobe center,  $r_l$  is the large lobe radius, and  $r_s$  is the small lobe radius). The boundaries of the shape parameter space explored were limited to model shapes that have physical relevance.[15] The following  $L^*$  and  $S$  combinations were excluded— dimers with the small lobe completely inside the large lobe for  $S \leq 1 - 2L^*$ , lobes disconnected for  $S > 2L^* - 1$ , smaller lobe fitting inside interstitial spaces for  $S \leq 2(1 - \sqrt{3}L^* + L^{*2})^{1/2} - 1$ .

We focus on the in-plane oblique crystal (c1m1) modeled as high dielectric asymmetric dimers oriented along  $\langle 010 \rangle$  on a centered rectangular lattice (c2mm) in air (Figure 4.1c). The centered rectangular structure of dimer particles [ $S = 0.86$  and  $L^* = 0.33$  (pear-shaped);  $S = 1.00$ ,  $L^* = 0.28$  (spherocylinder)] by convective assembly has been reported.[15] Furthermore, the control of refractive index by physical vapor deposition to obtain an inverted Ge centered rectangular dimer structure from the polystyrene templates was demonstrated.[14] The centered rectangular structure was also determined as the lowest height monolayer phase in the sequence in-plane crystal, rotator, out-of-plane hexagonal crystal under wedge cell confinement for dimers with shape parameters  $S = 0.89$  and  $L^* = 0.49$ .[24] The corresponding Brillouin zone with high symmetry points indicated is provided in Figure 4.1b. The primitive lattice vectors of the centered rectangular crystal structure are  $\vec{a}_1 = \begin{bmatrix} 1 & 0 & 0 \end{bmatrix}$ ,  $[|\vec{a}_1| = \sqrt{r_l^2 + (L + x)^2}]$  and  $\vec{a}_2 = \begin{bmatrix} 0 & 1 & 0 \end{bmatrix}$ ,  $[|\vec{a}_2| = 2(L + x)]$  where  $x = \sqrt{r_s^2 - 2r_s r_l}$ . The dimer particle model positions a lobe of radius  $r_l$  at  $\begin{bmatrix} 0 & 0 & 0 \end{bmatrix}$  and a lobe of radius  $r_s$  at  $\begin{bmatrix} 0 & L & 0 \end{bmatrix}$ .

Photonic band structures were calculated with the fully vectorial plane wave method

using the MIT Photonic Bands software package.[21] Periodic boundaries were imposed at a vertical spacing of eight times the diameter of the large lobe. Dispersion curves of light frequency versus wavevector were generated by numerically solving the eigenfrequencies for the first ten bands (i.e., resolution 16, mesh size 5, and convergence tolerance 0.001 %). One hundred wavevector points were interpolated between the high symmetry points in the irreducible Brillouin zone. Radiation outside the plane of the slab is represented by an opaque grey region overlaying the band diagram. The lower limit or light cone is the wavevector magnitude divided by the refractive index of the air cladding ( $\epsilon = 1$ ). The dielectric contrast ratio,  $\epsilon_c$ , between high (i.e., particle) and low (i.e., matrix) dielectric regions was varied from 6 (ZnS) to 16 (Ge). Complete band gaps were determined in the sense that no guided modes existed for the frequency range. The dielectric volume filling fraction ( $f$ ) was varied by reducing the large asymmetric dimer lobe radius from the tangent value of 0.5 (Figure 4.1c, dark grey) to 0.25 (Figure 4.1c, light grey). The smaller lobe was adjusted accordingly to maintain the lobe symmetry and degree of fusion.

#### 4.4 Results and Discussion

The band diagrams in Figure 4.2a-f detail the evolution of odd mode band gaps as a function of filling fraction in a moderately lobe-fused, highly asymmetric dimer structure ( $L^* = 0.5, S = 0.24$ ) at a dielectric contrast of 11 (InP). The particles are tangent at a filling fraction of 60.9 % (Figure 4.2f) and are widely spaced at a filling fraction of 7.6 % (Figure 4.2a). A gap between the 3rd and 4th bands (3 – 4 gap) dominates at moderate filling fractions ( $r_l = 0.35, f = 20.9\%$ ) and opens to 19.3 %. A smaller gap of 4.9 % between the 6th and 7th bands (6 – 7 gap) opens at higher filling fractions ( $r_l = 0.45, f = 44.4\%$ ) in Figure 4.2e. In the tangent particle case, the bands are compressed to lower frequency

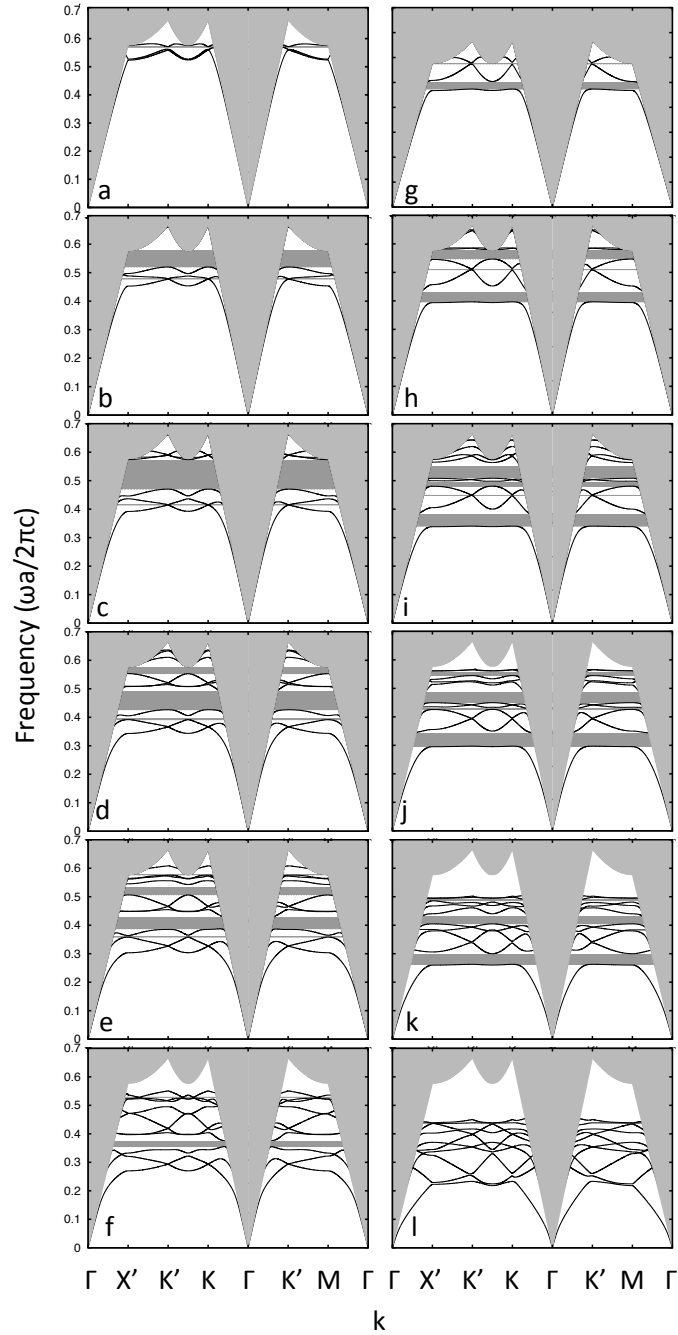


Figure 4.2: Band diagrams for direct asymmetric dimer structure ( $L^* = 0.5$ ,  $S = 0.239$ ,  $\epsilon_c = 11$ ) odd modes as a function of filling fraction a)  $f = 7.6\%$ ,  $r_l = 0.25$ ; b)  $f = 13.2\%$ ,  $r_l = 0.30$ ; c)  $f = 20.9\%$ ,  $r_l = 0.35$ ; d)  $f = 31.2\%$ ,  $r_l = 0.40$ ; e)  $f = 44.4\%$ ,  $r_l = 0.45$ ; f)  $f = 60.9\%$ ,  $r_l = 0.50$  (tangent). Band diagrams for direct asymmetric dimer structure ( $L^* = 0.2$ ,  $S = 0.666$ ,  $\epsilon_c = 16$ ) even modes as a function of filling fraction g)  $f = 7.6\%$ ,  $r_l = 0.25$ ; h)  $f = 13.1\%$ ,  $r_l = 0.30$ ; i)  $f = 20.8\%$ ,  $r_l = 0.35$ ; j)  $f = 31.1\%$ ,  $r_l = 0.40$ ; k)  $f = 44.3\%$ ,  $r_l = 0.45$ ; l)  $f = 60.8\%$ ,  $r_l = 0.50$  (tangent).

and only a 3 – 4 gap of 11.9 % remains.

The even mode band gaps as a function of filling fraction for a highly lobe-fused, moderately asymmetric dimer structure ( $L^* = 0.2, S = 0.67$ ) at a dielectric contrast of 16 are presented in Figure 4.2g-l. The 1 – 2 gap is maximized to 14.3 % for separated dimers at a filling fraction of  $f = 31.1$  % (Figure 4.2j). Bands with higher indices shift to higher frequency and 2 – 3, 3 – 4 and 5 – 6 gaps open at lower filling fractions (Figure 4.2g-i). The closest-packed, tangent arrangement closed the 1 – 2 gap due to degeneracy at the M high symmetry point.

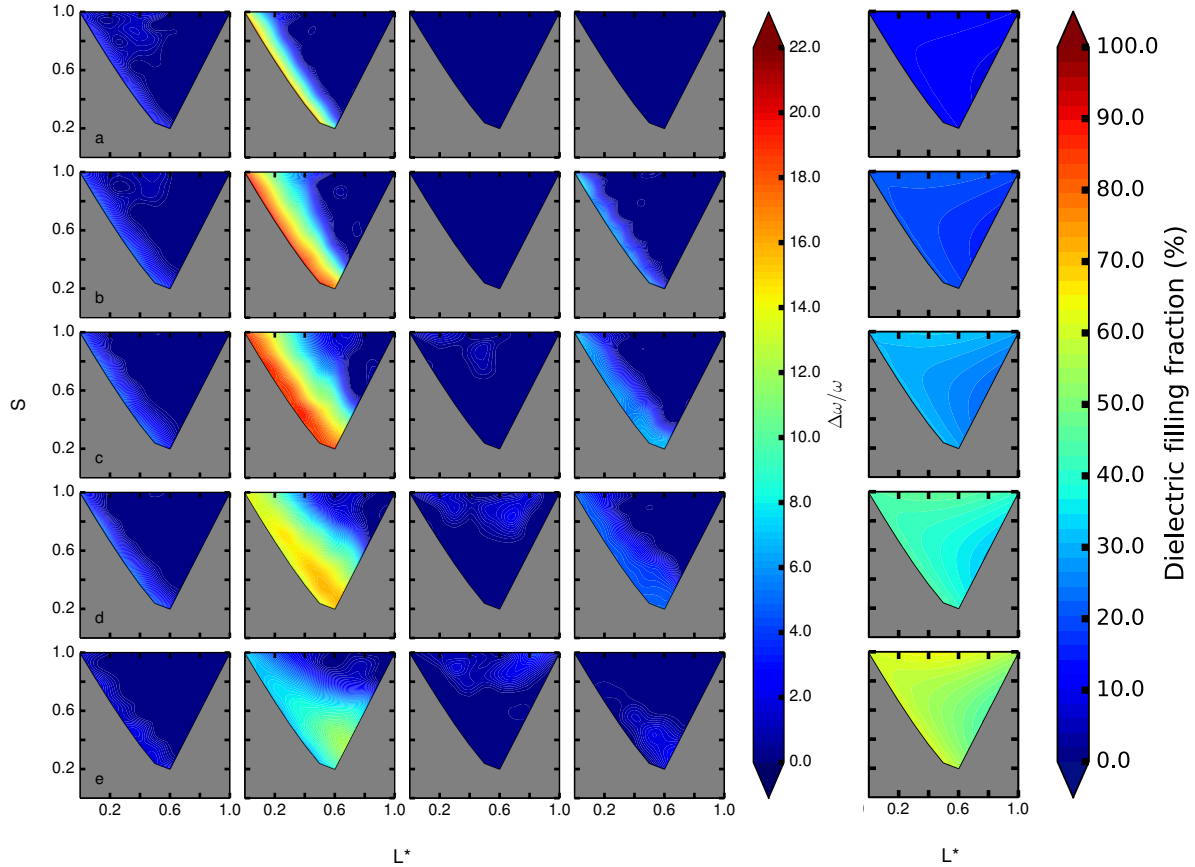


Figure 4.3: Left) Contour plots of largest odd mode 2 – 3 gap (left), 3 – 4 gap (center left), 4 – 5 gap (center right), 6 – 7 gap (right) in direct asymmetric dimer structures ( $6 \leq \epsilon_c \leq 16$ ). Right) contour plots of dielectric filling fraction as a function of  $L^*$  and  $S$  shape parameters at  $r_l$  values of a) 0.30, b) 0.35, c) 0.40, d) 0.45, e) 0.50 (tangent).

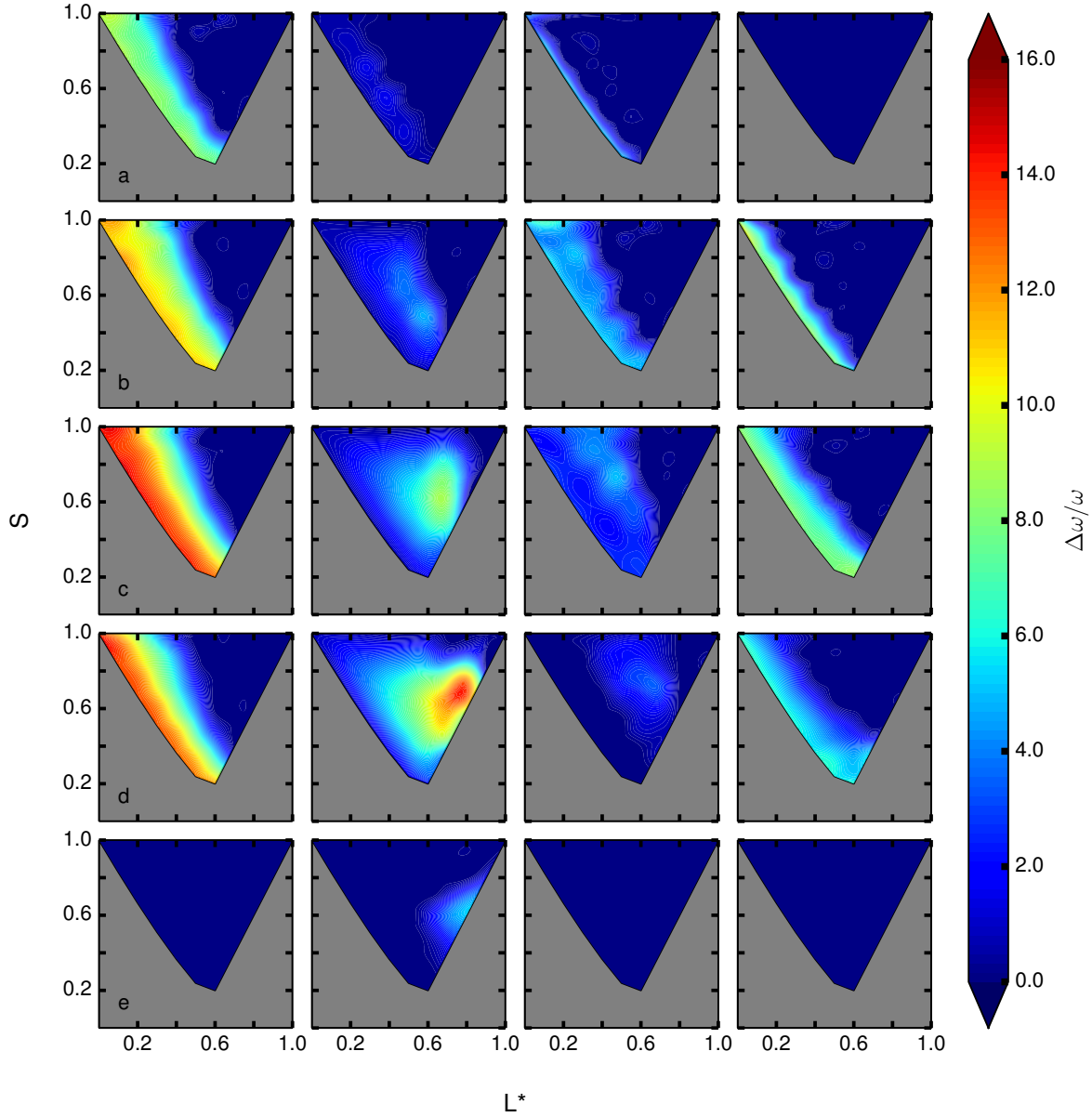


Figure 4.4: Contour plots of largest even mode 1-2 gap (left), 2-3 gap (center left), 3-4 gap (center right), 5-6 gap (right) in direct asymmetric dimer structures ( $6 \leq \epsilon_c \leq 16$ ) as a function of  $L^*$  and  $S$  shape parameters at  $r_l$  values of a) 0.30, b) 0.35, c) 0.40, d) 0.45, e) 0.50 (tangent).

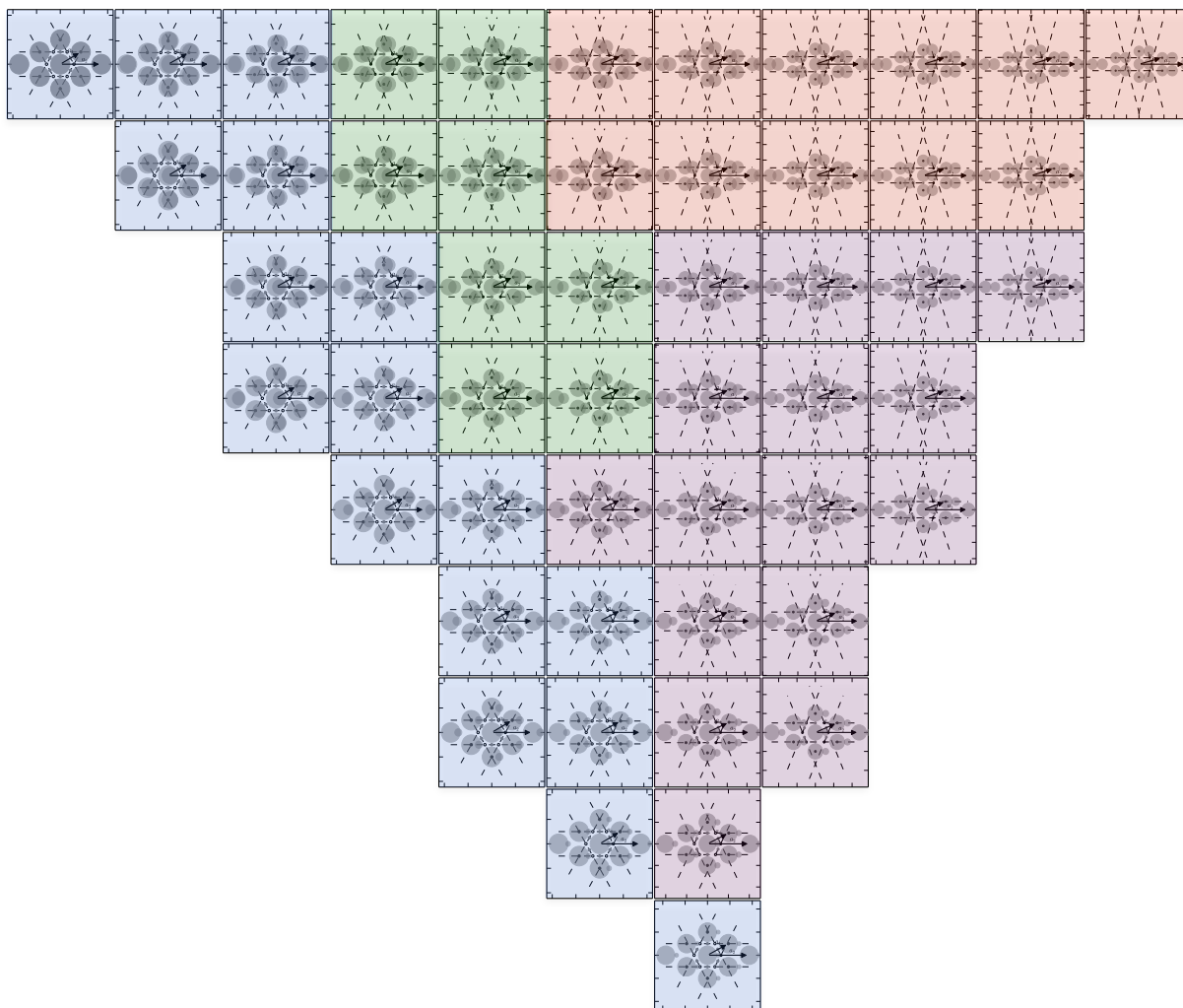


Figure 4.5: Schematics of representative asymmetric dimer structures at  $r_l$  value of 0.40. Ordinate values are  $S$  and abscissa values are  $L^*$  shape parameters. Placement tiles parameter space corresponding to contour plots in Figures 4.3, 4.4 and 4.6.

Contour plots of odd (Figure 4.3) and even (Figure 4.4) mode band gap size are shown as a function of shape parameters and filling fraction. Figure 4.5 highlights the common morphology features of structures at  $r_l = 0.40$  supporting similar band gap widths for the largest gaps. In shape parameter region I (blue), dimers have minor distortions from spherical shapes— i.e., highly asymmetric secondary lobe protrusion or highly fused spherocylinder. The degree of lobe fusion is high to moderate for the entire range of lobe symmetry. The exact spherical particle shape is given by  $L^* = 0.0, S = 1.00$  in the class. The adjacent shape parameter region (region II, green) is composed of dimers with substantially extended second lobes (moderate fusion, moderately high symmetry). The particle bases in shape parameter region III (purple) have moderate lobe fusion and low to moderate lobe symmetry. Shape parameter region IV (red) includes dimers with high lobe symmetry and moderately to mildly fused lobes. Morphologies with shape parameters in regions I-III favor band gap formation. The shapes in region IV surrounding the condition where lobes within a dimer just touch ( $L^* = 1.0, S = 1.00$ ) did not support significant band gaps.

The odd mode band gaps presented in Figure 4.3 indicate strong light matter interactions for region I shapes, particularly for the 3 – 4 bands. Reduced dielectric filling fractions supported the widest gaps (Figure 4.3b,c). The contour maps show 10% interval decreases in large lobe radius from Figure 4.3e to 4.3a that indicate greater particle separation and lower filling fractions. The filling fractions are presented explicitly in the right inset of Figure 4.3. Region III shapes exhibit large 3 – 4 gaps up to 15% at lower filling of the dielectric compared to region I shapes at similar particle separations. The extended range of shape parameters with wide band gaps is highlighted by Figure 4.3d and Figure 4.3e.

Figure 4.4 summarizes the parameters supporting even mode band gaps. Region I

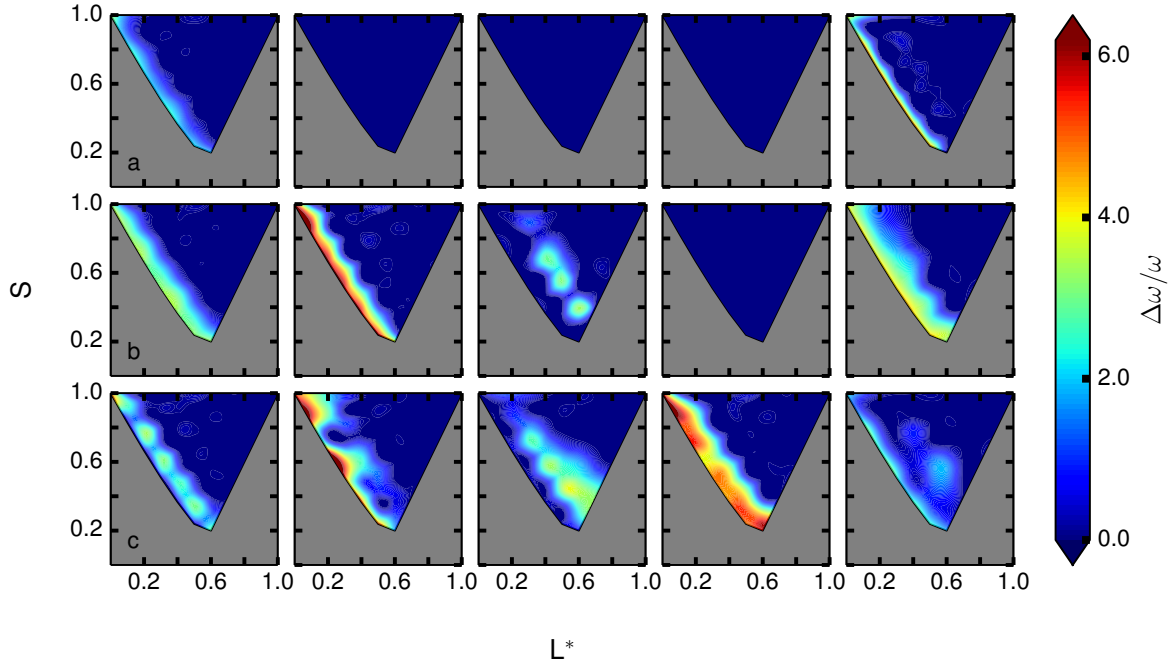


Figure 4.6: Contour plots of maximum polarization independent odd 2-odd 3 gap from (left) overlapped 1 – 2 even and 2 – 3 odd gaps, odd 6-odd 7 gap from (center left) overlapped 5 – 6 even and 6 – 7 odd gaps, odd 3-even 3 from (center) overlapped 3 – 4 odd and 2 – 3 even, odd 6-even 6 gap from (center right) overlapped 5 – 6 even gap and 6 – 7 odd gap, even 3-odd 4 gap from (right) overlapped 3 – 4 even and odd gaps in direct asymmetric dimer structures ( $6 \leq \epsilon_c \leq 16$ ) as a function of  $L^*$  and  $S$  shape parameters at  $r_l$  values of a) 0.30, b) 0.35, c) 0.40.

shapes gave rise to the largest 1 – 2 gap widths for 10 – 20 % decrease in large lobe radius from the tangent particle case. Moderate 5 – 6 band gaps for region I shapes were also determined with most significance at 20 % decrease in  $r_l$  from tangency. Region III shapes supported 2 – 3 band gaps up to 13.6 % for particle separations characterized by 0 – 20 % decrease from closest packing. Lower filling fractions yielded significant 1 – 2 band gaps and also 2 – 3 band gaps for region III shapes at moderate particle spacing.

Specific particle arrangements in regions I-IV belong to the plane symmetry groups p6mm (region I), c2mm (regions II, IV;  $S = 1.00$ ), and c1m1 (regions I-IV). Region I spheroidal morphologies lead to point group m ( $C_s$ ) and lack a mirror symmetry element perpendicular to the lattice vector  $\vec{a}_2$  (Figure 4.1) compared to spheres on a hexagonal lattice with point group 6mm ( $L^* = 0.0$ ,  $S = 1.00$ , plane group p6mm). The symmetry reduction to mildly anisotropic shapes still maintains a similarly high degree of Brillouin zone isotropy. Minor variance from the hexagonal mesh ( $< 1^\circ$ ) generated larger gaps with low gap indices. In addition, the 3 – 4 odd and 1 – 2 even gaps remained sizable at lattice distortions up to 16.7 % from hexagonal (i.e., interior angle value of  $50^\circ$ ) for structures belonging to the c1m1 plane group. The basis shapes that generate c2mm plane group symmetry in region IV correspond to the most anisotropic Brillouin zones and the highest filling fractions at any given particle spacing. Therefore, the structures are poor band gap formers for either polarization.

The polarization independent gaps (i.e., complete gaps for the guided modes) are represented in the contour plots of Figure 4.6 at the dielectric contrasts from 6 to 16 that determined the largest gaps. The crystals with basis elements in shape parameter region I supported overlaps between the frequencies of the 1 – 2 even and 2 – 3 odd gaps, the 3 – 4 even and 3 – 4 odd gaps and the 5 – 6 even and 6 – 7 odd gaps. The last overlap gap is the largest polarization independent gap,  $\Delta\omega/\omega = 6.2\%$  (i.e., parameters  $r_l = 0.35$ ,  $L^* = 0.2$ ,

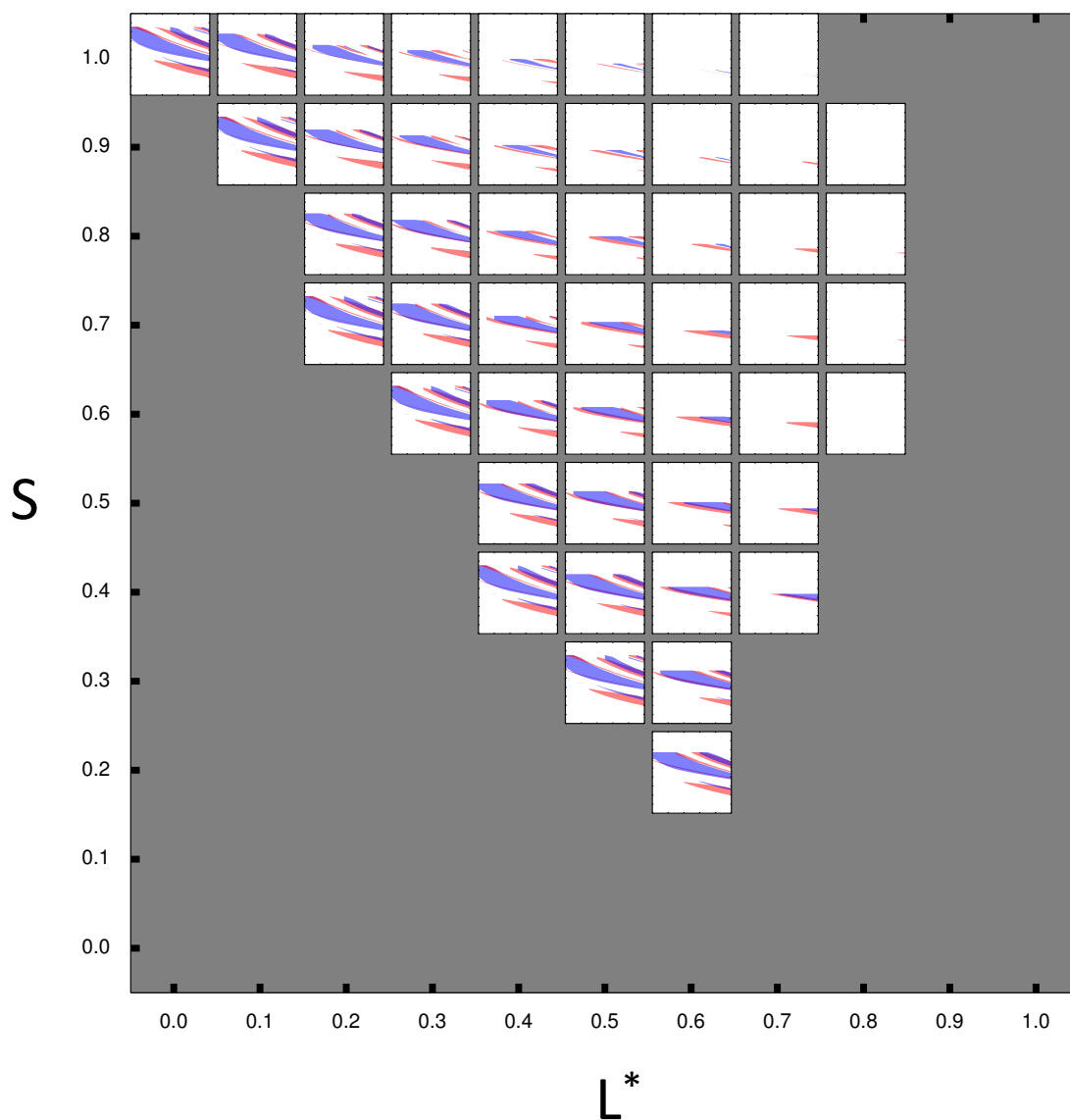


Figure 4.7: Representative gap maps with odd mode gaps (blue), even mode gaps (red) and overlapped gaps (purple) for  $r_l = 0.40$  asymmetric dimer arrangements.

$S = 0.67$ , and  $\epsilon_c = 15$ ). In comparison, an ellipse cross-section basis on a centered rectangular lattice yielded a 5.2% polarization independent gap for the inverted photonic crystals.[33] Structures with lattice decoration belonging to shape parameter regions II and III supported overlap between the 2 – 3 even and 3 – 4 odd gaps.

Figure 4.7 tiles the gap maps of frequency versus dielectric contrast for  $r_l = 0.40$  dimer morphologies. The odd, even and polarization independent band gaps are labeled in blue, red and purple, respectively. Slab reports often restrict the dielectric contrast values investigated to those that correspond with silicon or gallium arsenide i.e., substrates common in industrial microelectronic fabrication. However, a wide variety of materials (i.e., semiconductors and other ceramics) can be used in the dimer bases as is shown by the range of dielectric contrasts supporting polarization independent and dependent gaps. Across each row of gap maps in Figure 4.7, odd and even gaps open at higher dielectric contrasts and at lower frequency as the degree of lobe fusion decreases. The more anisotropic Brillouin zone causes band intersections with the light cone presenting the frequency limitation. The shape anisotropy reduces filling fraction (Figure 3) and necessitates higher optical density (i.e., higher dielectric contrast). Similarly, the trend is also apparent in filling fraction variation through basis separation. Supplemental Figure 4.8 displays the gap maps at  $r_l = 0.35$  and  $0.45$ . Numerous studies have established that isolated high dielectric regions favor odd mode gap size and that connectivity of the high dielectric regions preferentially enlarges even mode gaps.[18, 37, 3] The direct photonic slab structures here thus support large odd mode gaps and only moderate even mode gap widths. Moreover, the values of dielectric contrast to maximize the gap for each polarization do not coincide. This leads to relatively limited polarization independent gap sizes. Polarization independent gaps would be particularly useful for [1] cavities to suppress resonance at harmonic frequencies in the case of multiple full gaps, [2] multilayer solar cell designs for energy harvesting, [3] nonlinear optics applications, where light in-

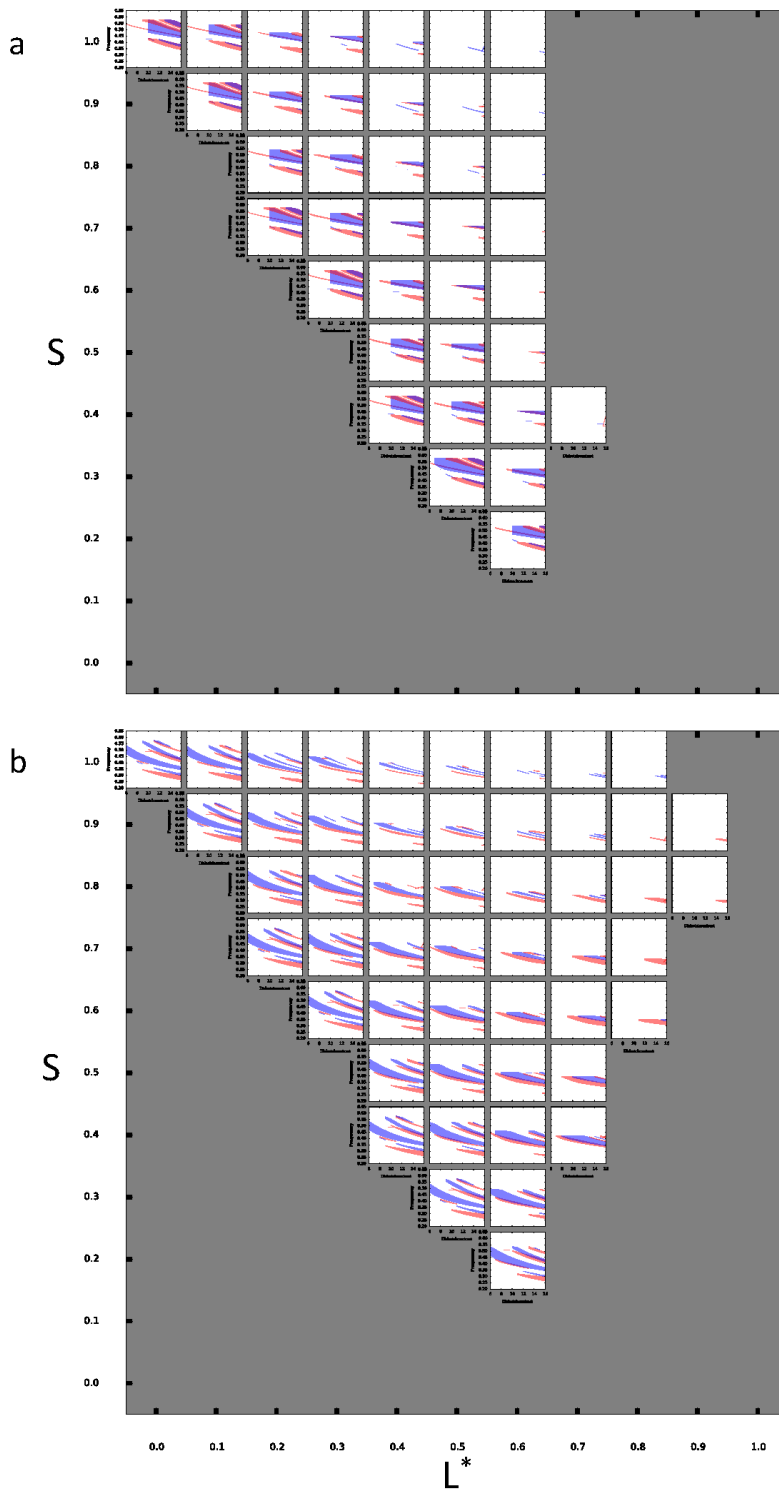


Figure 4.8: Gap maps with odd mode gaps (blue), even mode gaps (red) and overlapped gaps (purple) for asymmetric dimer structures with  $r_1$  values of a) 0.35 and b) 0.45.

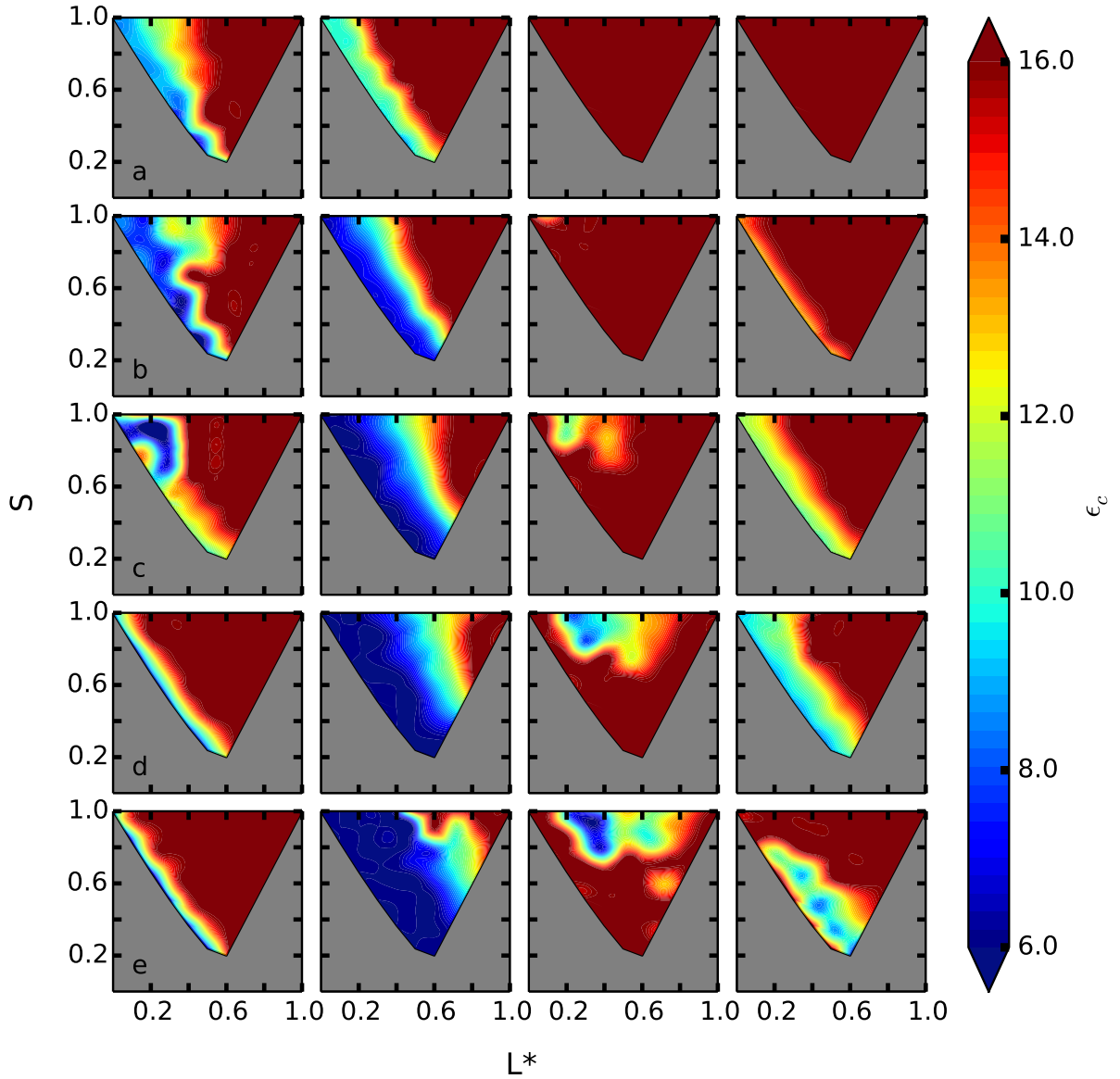


Figure 4.9: Contour plots of the minimum dielectric contrasts of odd mode 2-3 gap (left), 3-4 gap (center left), 4-5 gap (center right), 6-7 gap (right) in direct asymmetric dimer structures ( $6 \leq \epsilon_c \leq 16$ ) as a function of  $L^*$  and  $S$  shape parameters at  $r_l$  values of a) 0.30, b) 0.35, c) 0.40, d) 0.45 and e) 0.50 (tangent).

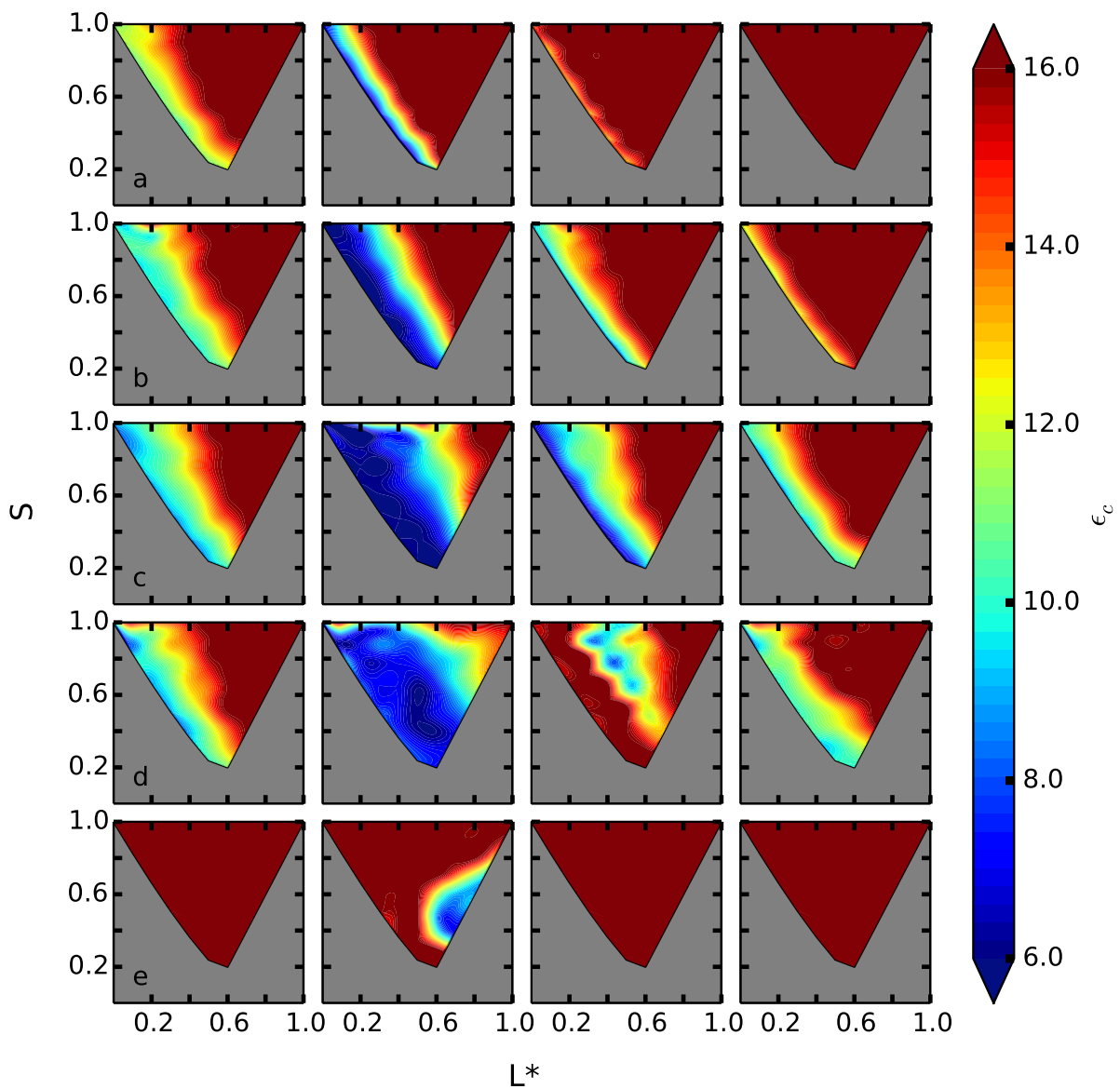


Figure 4.10: Contour plots of minimum dielectric contrasts at which even mode 1-2 gap (left), 2-3 gap (center left), 3-4 gap (center right), 5-6 gap (right) in direct asymmetric dimer structures ( $6 \leq \epsilon_c \leq 16$ ) as a function of  $L^*$  and  $S$  shape parameters at  $r_l$  values of a) 0.30, b) 0.35, c) 0.40, d) 0.45 and e) 0.50 (tangent).

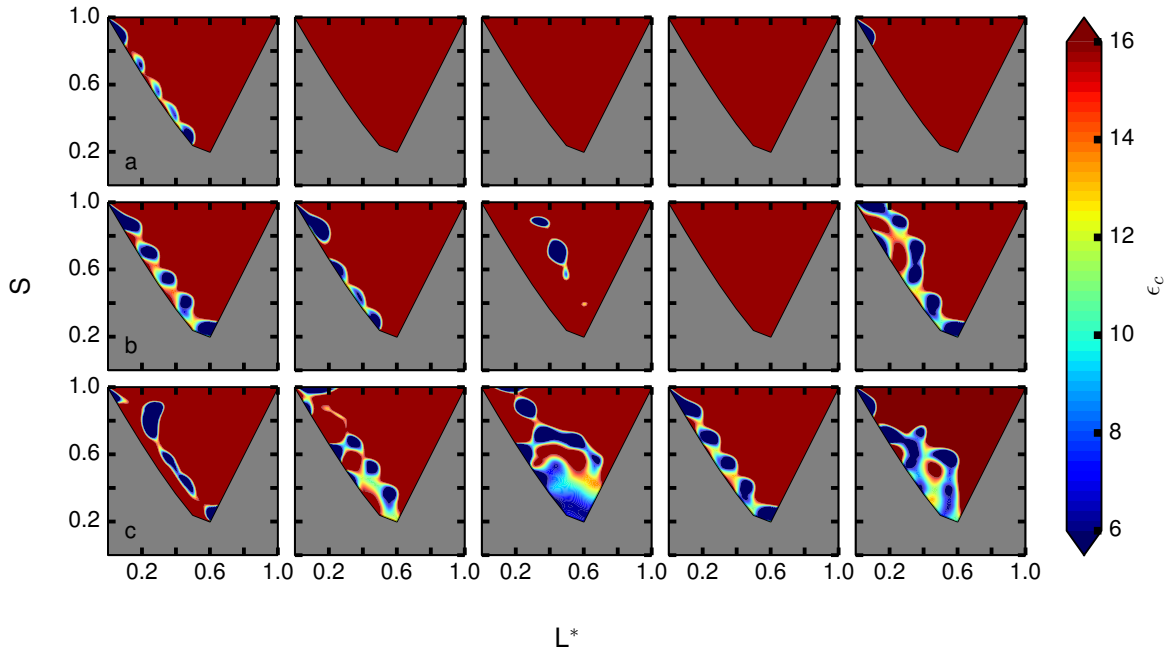


Figure 4.11: Contour plots of minimum dielectric contrast for polarization independent odd 2-odd 3 gap from (left) overlapped 1 – 2 even and 2 – 3 odd gaps, odd 6-odd 7 gap from (center left) overlapped 5 – 6 even and 6 – 7 odd gaps, odd 3-even 3 from (center) overlapped 3 – 4 odd and 2 – 3 even, odd 6-even 6 gap from (center right) overlapped 5 – 6 even gap and 6 – 7 odd gap, even 3-odd 4 gap from (right) overlapped 3 – 4 even and odd gaps in direct asymmetric dimer structures ( $6 \leq \epsilon_c \leq 16$ ) as a function of  $L^*$  and  $S$  shape parameters at  $r_l$  values of a) 0.30, b) 0.35, c) 0.40.

Table 4.1: Shape and structural parameters yielding maximum gap sizes. The corresponding dielectric contrasts for maximum gap widths and minimum dielectric contrasts opening the gaps are provided.

Polarization	Gap index	$L^*$	$S$	$r_l$	$f$ (%)	Max $\Delta\omega/\omega_m$ (%)	$\epsilon_c$	Min $\epsilon_c$
Odd	3-4	0.1	0.83	13.1	0.30	15.9	16	10
Odd	3-4	0.5	0.24	20.9	0.35	19.3	11	7
Odd	3-4	0.6	0.20	29.0	0.40	19.1	9	6
Odd	3-4	0.6	0.30	38.5	0.45	15.6	8	6
Odd	3-4	0.7	0.40	46.8	0.50	11.9	9	7
Odd	6-7	0.2	0.67	20.8	0.35	6.2	15	14
Odd	6-7	0.0	1.00	31.0	0.40	6.7	12	11
Odd	6-7	0.6	0.20	41.3	0.45	5.1	11	10
Even	1-2	0.1	0.83	13.1	0.30	8.9	16	11
Even	1-2	0.1	0.83	20.8	0.35	11.7	16	10
Even	1-2	0.2	0.67	31.1	0.40	14.3	16	9
Even	1-2	0.1	0.93	43.7	0.45	13.3	16	10
Even	2-3	0.7	0.60	24.4	0.40	8.3	16	12
Even	2-3	0.8	0.70	34.4	0.45	13.6	16	12
Even	2-3	0.8	0.60	44.7	0.50	5.2	15	9
Even	3-4	0.2	0.67	13.1	0.30	5.4	16	14
Even	3-4	0.4	0.37	20.9	0.35	5.4	11	9
Even	5-6	0.2	0.67	20.8	0.35	8.3	15	13
Even	5-6	0.0	1.00	31.0	0.40	8.3	14	10
Even	5-6	0.1	0.83	31.0	0.40	8.3	14	10
Even	5-6	0.1	0.83	44.2	0.45	6.3	16	11
Both	1 even-2 even	0.2	0.67	20.8	0.35	6.2	15	10
Both	1 even-2 even	0.1	0.83	31.0	0.40	5.5	14	6

tensity would be significantly diminished by the limitation to polarized light sources and [4] light extraction (i.e., out coupling) from slabs with internal sources that emit in both polarizations.

The minimum dielectric contrast to open the gaps is presented as contour plots for the shape parameter range in the supplementary material— Figure 4.9 (odd modes), Figure 4.10 (even modes) and Figure 4.11 (polarization independent). Excluding the region IV shapes, a wide range of the closest-packed dimer to moderate dimer separation structures open the sizable 2 – 3 odd mode gaps and 3 – 4 even mode gaps at a dielectric contrast value of 6 (ZnS). Table 4.1 lists shape and structural parameters as well as the dielectric contrast to open and maximize gaps with sizes greater than 5 %.

The context of this report lies in the field of colloidal self-assembly, particularly, informed by the burgeoning interest in dimer synthetic systems.[36, 19, 22] However, variations could be explored to further enhance gap width such as anisotropic dielectric constants (i.e., liquid crystals, tellurium), high refractive index cladding layers, veins connecting motifs and slab height optimization. As a comparison, a polarization independent gap width of 12.8 % was determined for a structure with patterned cladding layers of  $\epsilon = 3.24$ , a wavelength normalized GaAs thickness of 0.112 and basis clusters of circular holes with 3m point symmetry rotated not to coincide with the hexagonal lattice mirror plane symmetry.[45] We also found a polarization independent gap width of 9.9 % when the slab height ( $h$ ) was varied to half the value for the tangent symmetric dimer and the parameters were  $L^* = 0.1$ ,  $S = 0.83$ ,  $r_l = 0.35$ ,  $\epsilon_c = 14$  for dimer cylinders (Figure 4.12).

With regard to fabrication, colloidal monolayers in arrangements fitting those modeled here have been prepared by controlled drying or evaporation-assisted assembly.[35, 15, 13] Building block separations can be achieved using soft core potentials,[52] electric field,[10] co-assembly with nanoparticles[51] or mechanically through transferring

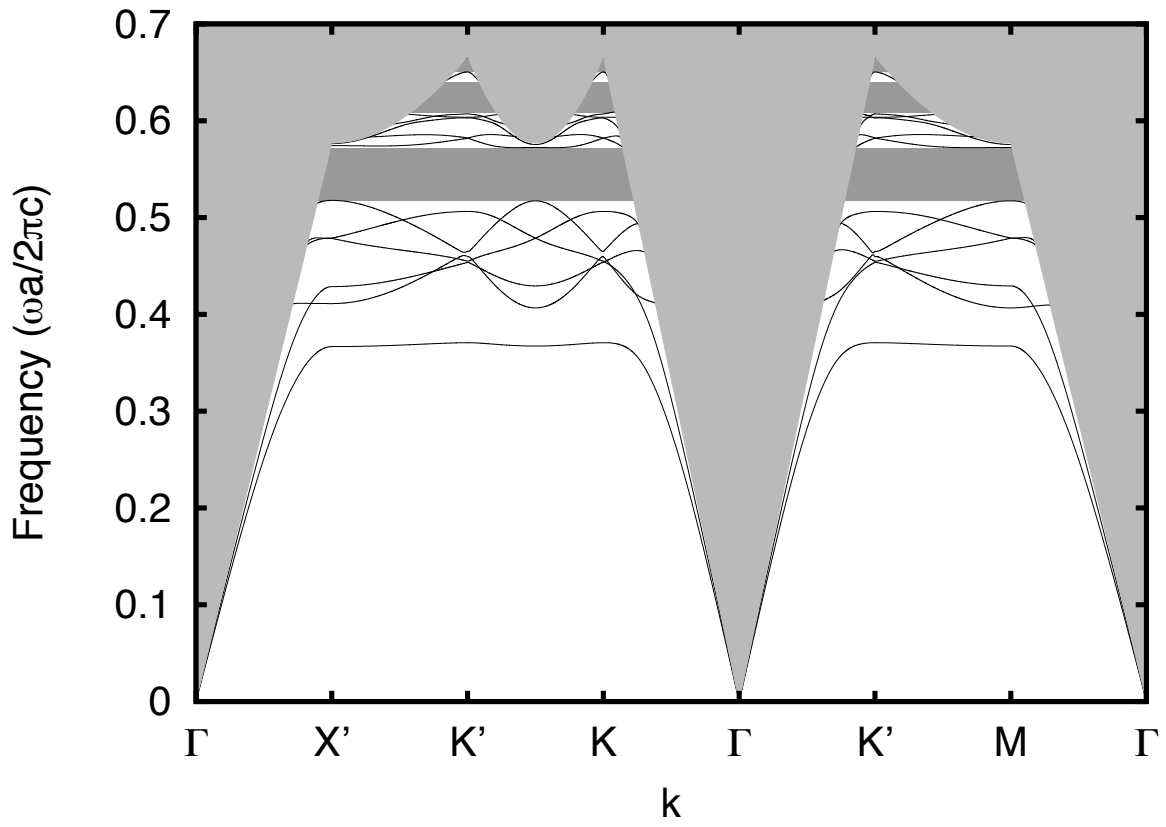


Figure 4.12: Band diagram at slab height  $h = 0.5$ ,  $r_l = 0.35$ ,  $L^* = 0.1$ ,  $S = 0.83$ ,  $\epsilon_c = 14$  for a dimer cylinder-based photonic crystal.

closepacked particles to a polymer film with subsequent swelling.[49] Double inversion infiltration techniques using sol-gel, atomic layer deposition and chemical- or physical vapor deposition can provide refractive index contrast for direct structures.[9, 28, 40, 44, 42, 27]

## 4.5 Conclusions

In summary, dimer shape-based photonic crystal slabs having Brillouin zones with high isotropy as well as moderate distortions allowed a wide range of lobe-symmetry and degree of lobe fusion combinations that supported odd and even polarization band gaps. Vertical variation of cross-section is implemented here giving the contoured 3D shape consistent with dimer self-assembly rather than photolithography realization. The building blocks have been cited for potential in photonics since bulk diamond analog dimer structures exhibit large, low indices band gaps.[26] However, the properties of dimers in slab photonic crystal configuration have not been previously calculated. This work adheres to the notion of developing theory contemporary with experimental realizations in contrast to disconnection where theory far out paces fabrication, as has been a paradigm in photonic band gap materials research. This work suggests, as specific insights for experiment, that self-assembly techniques which allow non-closepacked arrangements are needed to generate gaps. Also, templating on inverse structures or preparing high index colloidal clusters is a promising route to reduced symmetry photonic slabs.

## REFERENCES

- [1] Carlos Avendaño, Chekesha M. Liddell Watson, and Fernando A. Escobedo. Directed self-assembly of spherical caps via confinement. *Soft Matter*, 9(38):9153, 2013.
- [2] Zhongyu Cai, Jinghua Teng, Deying Xia, and X. S. Zhao. Self-assembly of crack-free silica colloidal crystals on patterned silicon substrates. *J. Phys. Chem. C*, 115(20):9970–9976, May 2011.
- [3] Yuan-Fong Chau. Intersecting veins effects of a two-dimensional photonic crystal with a large two-dimensional complete bandgap. *Opt. Commun.*, 282(21):4296–4298, November 2009.
- [4] Matthew Dennison, Kristina Milinković, and Marjolein Dijkstra. Phase diagram of hard snowman-shaped particles. *J. Chem. Phys.*, 137(4):044507, 2012.
- [5] Keiichi Edagawa, Satoshi Kanoko, and Masaya Notomi. Photonic amorphous diamond structure with a 3D photonic band gap. *Phys. Rev. Lett.*, 100(1):013901, January 2008.
- [6] Akira Emoto, Emi Uchida, and Takashi Fukuda. Fabrication and optical properties of binary colloidal crystal monolayers consisting of micro- and nano-polystyrene spheres. *Colloids Surf., A*, 396:189–194, February 2012.
- [7] E. Y. K. Fung, K. Muangnapoh, and C. M. L. Watson. Anisotropic photonic crystal building blocks: colloids tuned from mushroom-caps to dimers. *J. Mater. Chem.*, 22:10507–10513, 2012.
- [8] Eric M. Furst. Directed self-assembly. *Soft Matter*, 9(38):9039, 2013.
- [9] Juan F. Galisteo-López, Marta Ibisate, Riccardo Sapienza, Luis S. Froufe-Pérez, Álvaro Blanco, and Cefe López. Self-assembled photonic structures. *Adv. Mater.*, 23(1):30–69, January 2011.
- [10] T. Gong and D. W. M. Marr. Electrically switchable colloidal ordering in confined geometries. *Langmuir*, 17(8):2301–2304, 2001.
- [11] Benjamin Hatton, Lidiya Mishchenko, Stan Davis, Kenneth H. Sandhage, and Joanna Aizenberg. Assembly of large-area, highly ordered, crack-free inverse opal films. *Proc. Natl. Acad. Sci. U.S.A.*, 107(23):10354–10359, 2010.

- [12] Kevin P. Herlihy, Janine Nunes, and Joseph M. DeSimone. Electrically driven alignment and crystallization of unique anisotropic polymer particles. *Langmuir*, 24(16):8421–8426, August 2008.
- [13] I. D. Hosein, M. Ghebrebrhan, J. D. Joannopoulos, and C. M. Liddell. Dimer shape anisotropy: a nonspherical colloidal approach to omnidirectional photonic band gaps. *Langmuir*, 26(3):2151–2159, 2009.
- [14] I. D. Hosein, B. S. John, S. H. Lee, F. A. Escobedo, and C. M. Liddell. Rotator and crystalline films via self-assembly of short-bond-length colloidal dimers. *J. Mater. Chem.*, 19(3):344–349, 2009.
- [15] I. D. Hosein and C. M. Liddell. Convectively assembled asymmetric dimer-based colloidal crystals. *Langmuir*, 23(21):10479–10485, 2007.
- [16] I. D. Hosein and C. M. Liddell. Convectively assembled nonspherical mushroom cap-based colloidal crystals. *Langmuir*, 23(17):8810–8814, 2007.
- [17] C. Jamois, R.B. Wehrspohn, J. Schilling, F. Muller, R. Hillebrand, and W. Hergert. Silicon-based photonic crystal slabs: two concepts. *IEEE J. Quant. Electron.*, 38(7):805–810, 2002.
- [18] J. D. Joannopoulos, Steven G. Johnson, Joshua N. Winn, and Robert D. Meade. *Photonic Crystals: Molding the Flow of Light*. Princeton University Press, Princeton, 2nd edition, 2008.
- [19] Patrick M. Johnson, Carlos M. van Kats, and Alfons van Blaaderen. Synthesis of colloidal silica dumbbells. *Langmuir*, 21(24):11510–11517, November 2005.
- [20] Steven G. Johnson, Shanhui Fan, Pierre R. Villeneuve, J. D. Joannopoulos, and L. A. Kolodziejski. Guided modes in photonic crystal slabs. *Phys. Rev. B*, 60(8):5751–5758, August 1999.
- [21] Steven G. Johnson and John D. Joannopoulos. Block-iterative frequency-domain methods for maxwell’s equations in a planewave basis. *Opt. Express*, 8(3):173–190, 2001.
- [22] Jin-Woong Kim, Ryan J. Larsen, and David A. Weitz. Synthesis of nonspherical colloidal particles with anisotropic properties. *J. Am. Chem. Soc.*, 128(44):14374–14377, November 2006.
- [23] S. H. Lee, S. J. Gerbode, B. S. John, A. K. Wolfgang, F. A. Escobedo, I. Cohen, and

- C. M. Liddell. Synthesis and assembly of nonspherical hollow silica colloids under confinement. *J. Mater. Chem.*, 18(41):4912–4916, 2008.
- [24] Stephanie H Lee, Esther Y. Fung, E. K. Riley, and C. M. Liddell. Asymmetric colloidal dimers under quasi-2D confinement. *Langmuir*, 25(13):7193–7195, 2009.
- [25] Mirjam E. Leunissen, Christina G. Christova, Antti-Pekka Hynninen, C. Patrick Royall, Andrew I. Campbell, Arnout Imhof, Marjolein Dijkstra, René van Roij, and Alfons van Blaaderen. Ionic colloidal crystals of oppositely charged particles. *Nature*, 437(7056):235–240, September 2005.
- [26] Zhi-Yuan Li, Jian Wang, and Ben-Yuan Gu. Full band gap in fcc and bcc photonic band gaps structure: Non-Spherical atom. *J. Phys. Soc. Jpn.*, 67(9):3288–3291, 1998.
- [27] Luis M. Liz-Marz'an and Prashant V. Kamat, editors. *Nanoscale materials*. Kluwer Academic Publishers, Boston, 2003.
- [28] C. López. Materials aspects of photonic crystals. *Adv. Mater.*, 15(20):1679–1704, 2003.
- [29] Simon O. Lumsdon, Eric W. Kaler, and Orlin D. Velev. Two-dimensional crystallization of microspheres by a coplanar AC electric field. *Langmuir*, 20(6):2108–2116, March 2004.
- [30] H. Men, N. C. Nguyen, R. M. Freund, K. M. Lim, P. A. Parrilo, and J. Peraire. Design of photonic crystals with multiple and combined band gaps. *Phys. Rev. E*, 83(4):046703, April 2011.
- [31] Eric B. Mock and Charles F. Zukoski. Determination of static microstructure of dilute and concentrated suspensions of anisotropic particles by ultra-small-angle x-ray scattering. *Langmuir*, 23(17):8760–8771, August 2007.
- [32] Mikhail A. Noginov, Graeme Dewar, Martin W. McCall, and Nikolay I. Zheludev, editors. *Tutorials in Complex Photonic Media*, volume PM194. SPIE Press, Bellingham, Wash, 2009.
- [33] Kris Ohlinger, Yuankun Lin, and Jeremy S. Qualls. Maximum and overlapped photonic band gaps in both transverse electric and transverse magnetic polarizations in two-dimensional photonic crystals with low symmetry. *J. Appl. Phys.*, 106(6):063520, 2009.
- [34] Priyadarshi Panda, Kai P. Yuet, T. Alan Hatton, and Patrick S. Doyle. Tuning cur-

- vature in flow lithography: A new class of Concave/Convex particles. *Langmuir*, 25(10):5986–5992, May 2009.
- [35] Jin-Gyu Park, Jason D. Forster, and Eric R. Dufresne. High-yield synthesis of monodisperse dumbbell-shaped polymer nanoparticles. *J. Am. Chem. Soc.*, 132(17):5960–5961, May 2010.
- [36] Bo Peng, Hanumantha Rao Vutukuri, Alfons van Blaaderen, and Arnout Imhof. Synthesis of fluorescent monodisperse non-spherical dumbbell-like model colloids. *J. Mater. Chem.*, 22(41):21893, 2012.
- [37] M. Qiu and S. He. Optimal design of a two-dimensional photonic crystal of square lattice with a large complete two-dimensional bandgap. *J. Opt. Soc. Am. B*, 17(6):1027–1030, 2000.
- [38] E. K. Riley, E. Y. Fung, and C. M. Watson. Buckled colloidal crystals with nonspherical bases for two-dimensional slab photonic band gaps. *J. Appl. Phys.*, 111(9):093504–093504, 2012.
- [39] E. K. Riley and C. M. Liddell. Confinement-controlled self assembly of colloids with simultaneous isotropic and anisotropic cross-section. *Langmuir*, 26(14):11648–11656, 2010.
- [40] Andreas Stein. Sphere templating methods for periodic porous solids. *Microporous Mesoporous Mater.*, 44:227–239, 2001.
- [41] Yoshinori Tanaka, Takashi Asano, Yoshihiro Akahane, Bong-Shik Song, and Susumu Noda. Theoretical investigation of a two-dimensional photonic crystal slab with truncated cone air holes. *Appl. Phys. Lett.*, 82(11):1661, 2003.
- [42] Krassimir P. Velikov, Alexander Moroz, and Alfons van Blaaderen. Photonic crystals of core-shell colloidal particles. *Appl. Phys. Lett.*, 80(1):49, 2002.
- [43] Kevin Vynck, David Cassagne, and Emmanuel Centeno. Superlattice for photonic band gap opening in monolayers of dielectric spheres. *Opt. Express*, 14:6668–6674, 2006.
- [44] Dayang Wang and Frank Caruso. Lithium niobate inverse opals prepared by templating colloidal crystals of polyelectrolyte-coated spheres. *Adv. Mater.*, 15(3):205–210, 2003.
- [45] Matthew D. Weed, Hubert P. Seigneur, and Winston V. Schoenfeld. Optimization

of complete band gaps for photonic crystal slabs through use of symmetry breaking hole shapes. *Proc. SPIE*, 7223:72230Q–72230Q–9, February 2009.

- [46] Feng Wen, Sylvain David, Xavier Checoury, Moustafa El Kurdi, and Philippe Boucaud. Two-dimensional photonic crystals with large complete photonic band gaps in both TE and TM polarizations. *Opt. Express*, 16(16):12278–12289, 2008.
- [47] K. Wojciechowski. Monte carlo simulations of highly anisotropic two-dimensional hard dumbbell-shaped molecules: Nonperiodic phase between fluid and dense solid. *Phys. Rev. B*, 46(1):26–39, July 1992.
- [48] Y. Xia, B. Gates, and Z.-Y. Li. Self-assembly approaches to three-dimensional photonic crystals. *Adv. Mater.*, 13(6):409–413, March 2001.
- [49] Xin Yan, Jimin Yao, Guang Lu, Xiao Li, Junhu Zhang, Kun Han, and Bai Yang. Fabrication of non-close-packed arrays of colloidal spheres by soft lithography. *J. Am. Chem. Soc.*, 127(21):7688–7689, June 2005.
- [50] Seung-Man Yang, Shin-Hyun Kim, Jong-Min Lim, and Gi-Ra Yi. Synthesis and assembly of structured colloidal particles. *J. Mater. Chem.*, 18(19):2177, 2008.
- [51] Xiaozhou Ye and Limin Qi. Two-dimensionally patterned nanostructures based on monolayer colloidal crystals: Controllable fabrication, assembly, and applications. *Nano Today*, 6(6):608–631, December 2011.
- [52] Anand Yethiraj. Tunable colloids: control of colloidal phase transitions with tunable interactions. *Soft Matter*, 3(9):1099, 2007.
- [53] Xuelian Zhu, Ying Zhang, Dinesh Chandra, Shih-Chieh Cheng, James M. Kikkawa, and Shu Yang. Two-dimensional photonic crystals with anisotropic unit cells imprinted from poly(dimethylsiloxane) membranes under elastic deformation. *Appl. Phys. Lett.*, 93(16):161911, 2008.

## CHAPTER 5

### SLAB PHOTONIC CRYSTALS WITH DIMER CYLINDER BASES\*

#### 5.1 Abstract

The photonic band gap properties of centered rectangular dimer cylinder structures are reported. The theoretical model is inspired by a crystalline phase found for colloidal self-assembly of asymmetric dimers. The band structures as a function of degree of lobe fusion and degree of lobe symmetry are calculated in accordance with the tunable features resulting from seeded emulsion polymerization synthesis. The parameters are varied incrementally from single circular cross-section cylinders to lobe-tangent dimer cylinders. Odd, even and polarization independent gaps in the guided modes are found for direct and inverted slab structures. A wide range of shape parameter combinations in structures having low to moderate Brillouin zone distortion from hexagonal supported relative gap widths up to 19.1 % (3 – 4 odd gap) and 14.6 % (1 – 2 even gap) for direct structures. Slab thickness was tuned to overlap even and odd mode gap frequency ranges generating a 9.9% polarization independent gap. The results are compared with those from model centered rectangular slabs having dimer particle bases that limit the slab height. Inverted slab structures yielded a large maximum 40.4% 1 – 2 even mode gap and for up to 25 % Brillouin zone distortion still supported significant gaps (> 32 %).

---

\*To be published as: Erin K. Riley and Chekesha M. Liddell Watson. "Slab Photonic Crystals with Dimer Cylinder Bases", *J Opt Soc Am B*, submitted (2014).

## 5.2 Introduction

Photonic crystals provide control over the propagation of electromagnetic radiation via dispersion engineering.[19] Band gaps for photons have been used to modify spontaneous emission and confine radiation. The materials promise dramatic improvement in efficiency or low loss for technologies such as solid state light, lasing, waveguides and optical switches. In addition, the dispersion relations can give rise to negative refraction for planar lenses with subwavelength resolution.

Many devices, as originally envisioned, were based on three dimensional (3D) dielectric periodicity to provide 3D light confinement. However, a slab waveguide with photonic crystal patterning satisfies 3D radiation control, i.e., in-plane using the two dimensional arrangement and out-of-plane through index-guiding.[11] The experimental counterpart has been achieved by modern lithographic fabrication methods. To date it has been challenging to analytically determine a priori the dielectric patterns possessing photonic band gaps. Relatively few slab photonic crystal structures have been examined in experiments or calculations. For example, line-defect waveguiding was demonstrated in a square lattice slab structure of GaAs rods on periodic  $Al_{0.9}Ga_{0.1}$  background with a band gap for TM-polarized light at 1448 – 1482 nm.[1] Empirical guidelines have established circular cross-section rods (on square lattices) and holes (on hexagonal lattices) as geometries generating band gaps.

Theoretical studies suggest more complex structures such as Archimedean tilings (i.e.,  $3^2 \cdot 4 \cdot 3 \cdot 4$  and  $4 \cdot 8^2$ , Schläfli symbols for ‘lady bug’ and ‘bathroom tile’), five-fold and eight-fold symmetric quasicrystals and honeycomb lattices of binary sized circular-pores promote gap formation.[27, 5, 28, 24, 16, 7] Symmetry reduction strategies have been employed to lift degeneracy in band structures. The lattice, basis scattering shapes and their

orientation can be modified.[14, 15, 25] For example, rotating a rounded triangular or trigonal cluster of circular cross-section pores in a GaAs (dielectric contrast  $\epsilon_c = 12.25$ ) slab  $9^\circ$  from a lattice vector led to a 12.8 % polarization independent band gap ( $\Delta\omega/\omega$ , gap-to-midgap ratio).[26] Mushroom cap-shaped colloids in buckled crystal arrangements exhibited multiple polarization independent band gaps between band indices 4 – 5, 8 – 9, and 12 – 13 for the inverted case depending on the specific shape parameters.[22]

The latter study was inspired by particle self-assembly and the expanding range of colloidal building block shapes including ellipsoids; cubes; cylinders; hex nuts; hexagonal-, square-, triangular-, trapezoidal- and pentagonal prisms; spherocylinders; dumbbells; asymmetric dimers; and sphere clusters with tetrahedral, octahedral, and square-bipyramidal, etc. geometry.[8, 21, 29, 4, 3, 33, 17, 32] Oblique and centered rectangular arrangements of asymmetric dimer particles have been prepared by evaporation assisted- and confinement self-assembly techniques.[9, 13] The realization of photonic slabs consistent with particle geometry leads to vertical variation in the cross-section throughout the slab. The structural diversity arising from the thermodynamics of self-assembly also provides arrangements that are unimagined in traditional lithographic studies. However, band gap size cannot be optimized efficiently through slab height without modifying the structure.

Here, we explore a cylinder realization that incorporates a wide range of structural variants inspired by self-assembly and is consistent with lithographic fabrication, where cross-section profile is fixed. The height of the cylinders in the present study was set to the height of the particle basis in the previous work so that the properties of the two types of realizations can be compared. For specific structures, slab height was used as an optimization parameter for the band gap size. Moderate symmetry reduction through lattice distortion and basis shape led to simultaneous, multiple gaps. Odd mode gaps up

to 19.1% and even mode gaps up to 14.6% for direct structures, as well as, even mode gaps up to 40.4% for inverted structures were determined. Polarization independent gaps up to 9.9% were achieved by varying slab height.

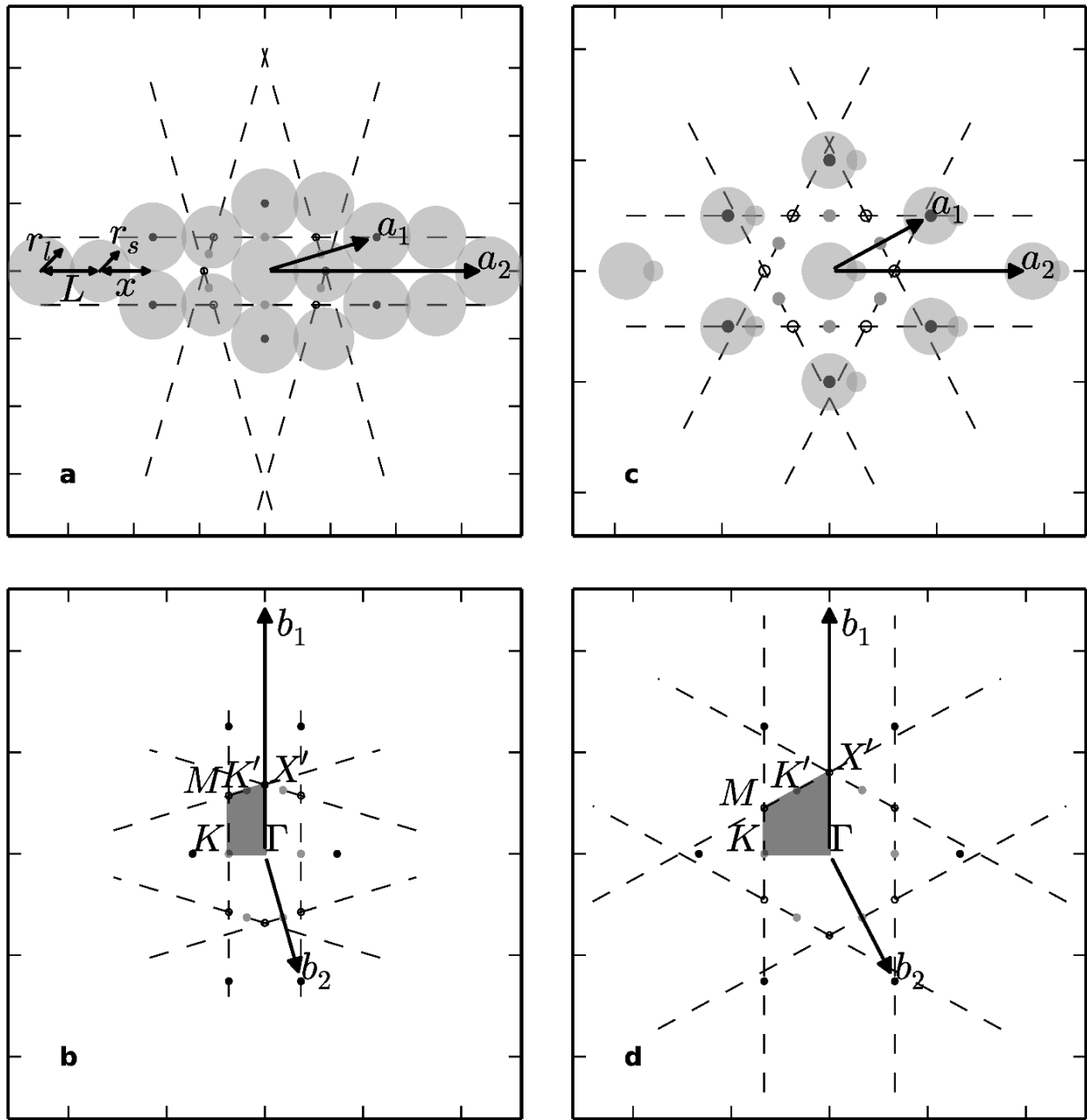


Figure 5.1: Schematics depicting top) unit cells and bottom) corresponding Brillouin zones for structure parameters a)  $r_l = 0.5$  (tangent),  $L = 0.9$ ,  $S = 0.90$  and c)  $r_l = 0.25$ ,  $L^* = 0.5$ ,  $S = 0.34$ . The high symmetry points are labeled and the irreducible Brillouin zone is highlighted in grey.

### 5.3 Computational Method

The asymmetric dimer shape was modeled as two overlapping cylinders as shown in Figure 5.1. Characteristic dimer shape parameters are quantified by the lobe symmetry parameter ( $S = r_s/r_l$ ) and the normalized bond length ( $L^* = L/2r_l$ , where  $L$  is the length between the lobe center,  $r_l$  is the large lobe radius, and  $r_s$  is the small lobe radius). The boundaries of the shape parameter space explored were limited to model shapes that have physical relevance.[9] The following  $L^*$  and  $S$  combinations were excluded— dimers with the small lobe completely inside the large lobe for  $S \leq 1 - 2L^*$ , lobes disconnected for  $S > 2L^* - 1$ , smaller lobe fitting inside interstitial spaces for  $S \leq 2(1 - \sqrt{3}L^* + L^{*2})^{1/2} - 1$ . The slab height was defined by the cylinder height  $h$ .

The centered rectangular crystal was modeled as a dielectric system with dimer particles oriented along  $\langle 0 \ 1 \ 0 \rangle$  on a centered rectangular lattice in air as shown in Figure 5.1a, c. The corresponding Brillouin zones with the high symmetry points indicated are shown in Figure 5.1b, d. The primitive lattice vectors are  $\vec{a}_1 = \begin{bmatrix} 1 & 0 & 0 \end{bmatrix}$ ,  $[\|\vec{a}_1\| = \sqrt{r_l^2 + (L + x)^2}]$  and  $\vec{a}_2 = \begin{bmatrix} 0 & 1 & 0 \end{bmatrix}$ ,  $[\|\vec{a}_2\| = 2(L + x)]$  where  $x = \sqrt{r_s^2 - 2r_s r_l}$ . The dimer cylinder model correlates the cylinder (radius  $r_l$ ) at  $\begin{bmatrix} 0 & 0 & 0 \end{bmatrix}$  with the cylinder (radius  $r_s$ ) at  $\begin{bmatrix} 0 & L & 0 \end{bmatrix}$  (Figure 5.1a).

Photonic band structures were calculated via the fully vectorial plane wave method using the MIT Photonic Bands software package.[12] Periodic boundaries were imposed with a vertical spacing of eight times the diameter of the larger dimer cylinder lobe. Dispersion curves of light frequency versus wavevector (reciprocal lattice vector) were generated by numerically solving the eigenfrequencies propagating in the crystal for the first ten bands with 100 wavevector points interpolated between the high symmetry points of the irreducible Brillouin zone (resolution 16, mesh size 5, and convergence tolerance

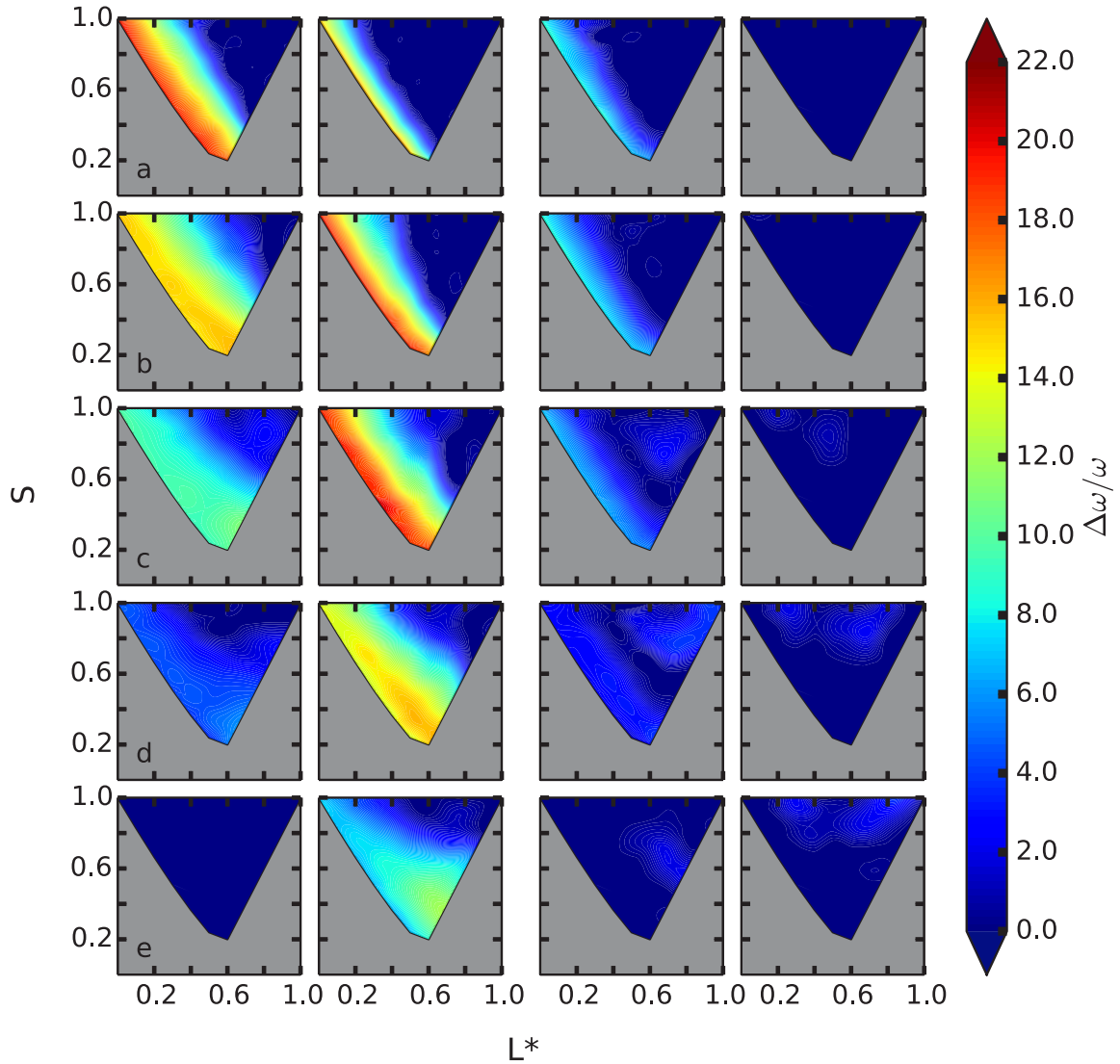


Figure 5.2: Maximum odd mode gaps in dimer cylinder and dimer particle bases for  $r_l$  values of a) 0.30, b) 0.35, c) 0.40, d) 0.45, e) 0.50 (tangent). The left column pair corresponds to the 3 – 4 band gap and the right column pair corresponds to the 4 – 5 band gap. Within column pairs the cylinder motif is modeled on the left and dimer bases on the right.

0.001 %). Radiation outside the plane of the slab is represented by an opaque grey region overlaying the band diagram. The lower limit, or light cone, is the wavevector magnitude divided by the refractive index of the air cladding ( $\epsilon = 1$ ). The dielectric contrast ratio,  $\epsilon_c$ , was varied from 6 to 16 for direct and inverted photonic crystal slabs. Complete band gaps were found in the sense that no guided modes existed for the frequency range. The dielectric volume filling fraction ( $f$ ) was varied by reducing the large cylinder lobe radius from tangency ( $r_l = 0.5$ , Figure 5.1a) to high dimer cylinder separations ( $r_l = 0.25$ , Figure 5.1c) in increments of 10% for reduced slab height  $h^* = h/2r_l = 1.0$ . The smaller lobe was adjusted accordingly to maintain the lobe symmetry and degree of fusion. Slab height variation  $h^* = 0.2$  to 6.5 was investigated for select structures.

## 5.4 Results and Discussion

A comparison between contour plots of odd mode band gap widths for dimer cylinder and dimer particle bases as a function of shape parameters  $S$  and  $L^*$  is shown in Figure 5.2. The maximum gap width supported over the dielectric range examined ( $6 \leq \epsilon_c \leq 16$ ) is given on the contour plots for each basis shape parameter pair. The cross-sectional morphologies represented in the shape parameter field are provided in Figure 5.3 for  $r_l = 0.30$ . Region I dimers (blue) show small distortions from circular cross-section cylinders featuring either highly fused symmetric lobes or small protrusion of a highly asymmetric cylinder lobe. The degree of fusion is high to moderate over all degrees of lobe symmetry in this class and includes the single circular cross-section cylinder shape (i.e.,  $L^* = 0.0$ ,  $S = 1.00$ ). Shape parameter region II (green) encompasses moderately high cylinder lobe symmetry and moderate lobe fusion. Lower symmetry cylinder dimers are grouped in region III (purple) spanning moderate to mildly fused lobes. Region IV includes cylinder pairs with high lobe symmetry and moderate to low lobe fusion. Symmetric cylinders

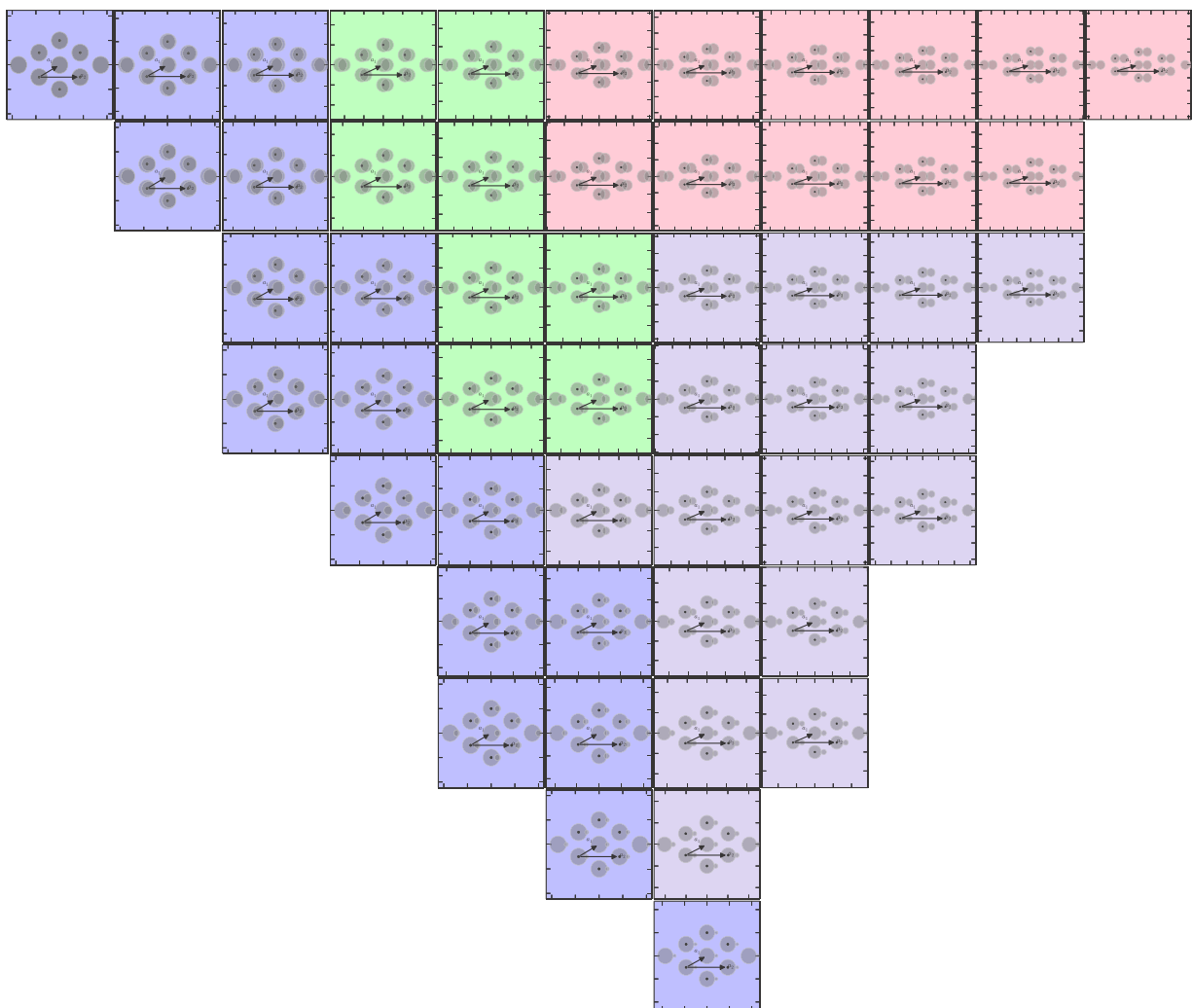


Figure 5.3: Schematics of dimer structures at  $r_l$  value of 0.35. Ordinate values are  $S$  and abscissa values are  $L^*$  shape parameters. The parameter space corresponding to contour plots and gap maps in Figures 5.2-5.8 and 5.17 is tiled.

with tangent lobes are included in this class at shape parameter values  $L^* = 1.0$  and  $S = 1.00$ .

A gap between the 3rd and 4th odd band indices (3 – 4 odd gap) in the cylinder dimer basis was significant for moderate dimer separations  $r_l = 0.30 - 0.40$ ,  $f = 27.5 - 70.0\%$  (Figure 5.2b-e, left column pair, left column). Large gap sizes extended over shape parameter regions I-III where the widest gap occurred in region I for  $r_l = 0.30$  ( $\Delta\omega/\omega = 19.1\%$ ,  $L^* = 0.1$ ,  $S = 0.83$ ,  $\epsilon_c = 10$ ). In comparison, the dimer particle realization supported significant gaps at particle tangency down to high particle separations (i.e.,  $r_l = 0.30$ ). Thus, a wider range of combined feature separation and shape parameter diversity allowed the 3 – 4 band gap in the particle case. A gap of 19.3% at  $r_l = 0.35$  was found for the particle dimer at a dielectric contrast of 11. For perspective, the maximum odd mode gap size was 22% for a single cylinder basis on a square lattice.[11] For both dimer cylinders and particle dimers, gaps formed at moderate to low filling fractions. Figure 5.4e,f indicates the dielectric filling fraction values are too high ( $f = 60.5 - 93.5\%$ ) to support the 3 – 4 odd mode gap in dimer cylinders at or near tangency (Figure 5.2e,f). At the highest basis separations the filling fraction was generally insufficient to shift the band frequencies below the light line. The basis separations associated with the maximum gap sizes shifted by  $0.2r_l$  (i.e., 20% decrease) for cylinders compared to particles with variation in vertical cross-section. The weaker 4 – 5 band gap widths were more pronounced for the dimer cylinder based structures than for the particle based arrangements. Values up to  $\Delta\omega/\omega = 8.6\%$  were determined for crystals with basis shape parameters in region I at separations 20 – 25% decreased from tangency. Additional gaps were found between the 2nd and 3rd, 6th and 7th and 9th and 10th odd band indices with gap sizes less than 5%.

Figure 5.5 shows a comparison between contour plots of even mode band gap sizes for dimer cylinder and dimer particle bases as a function of shape parameters. Significant

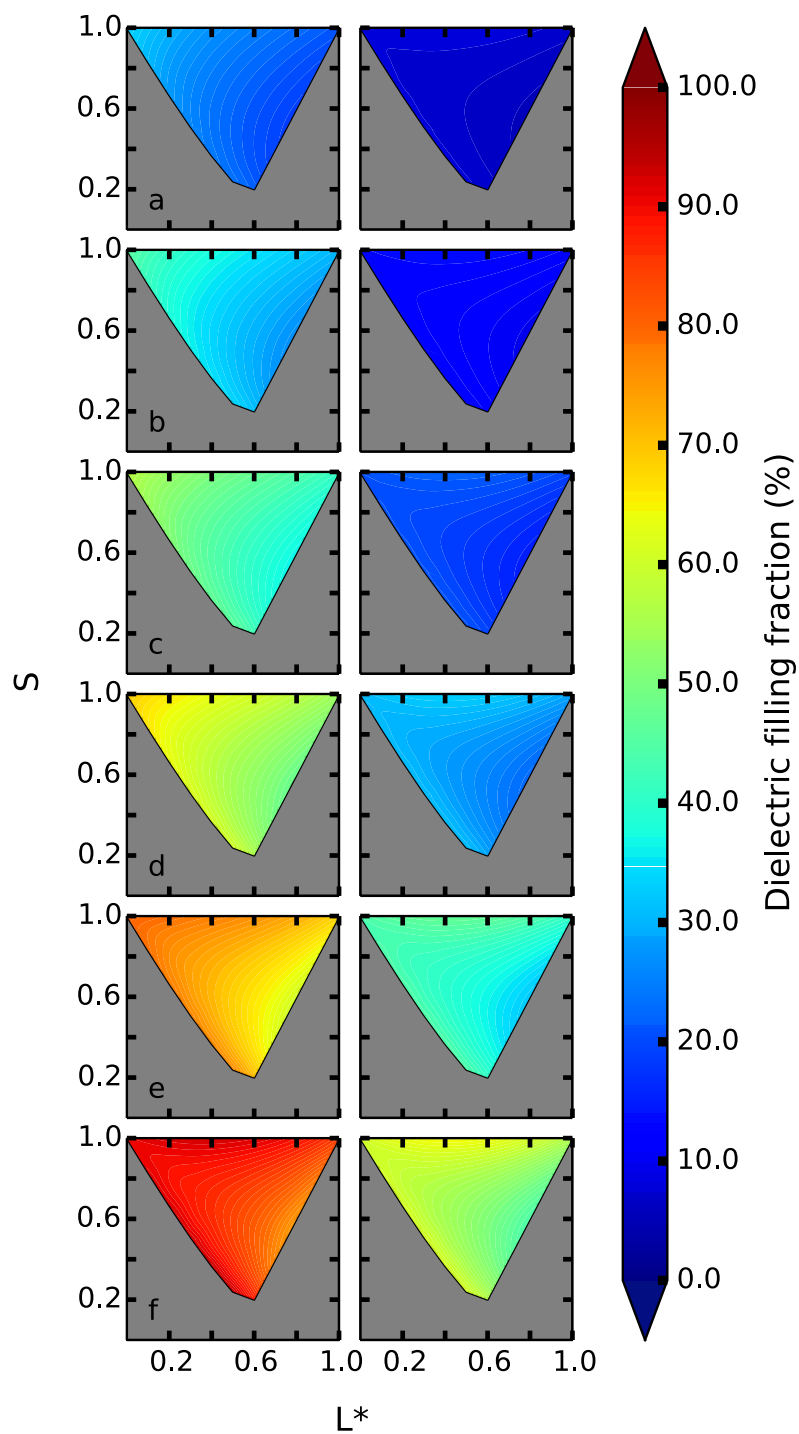


Figure 5.4: Dielectric filling fraction comparison for cylinder morphology (left) and dimer morphology (right) for  $r_l$  values of a) 0.25, b) 0.30, c) 0.35, d) 0.40, e) 0.45, f) 0.50.

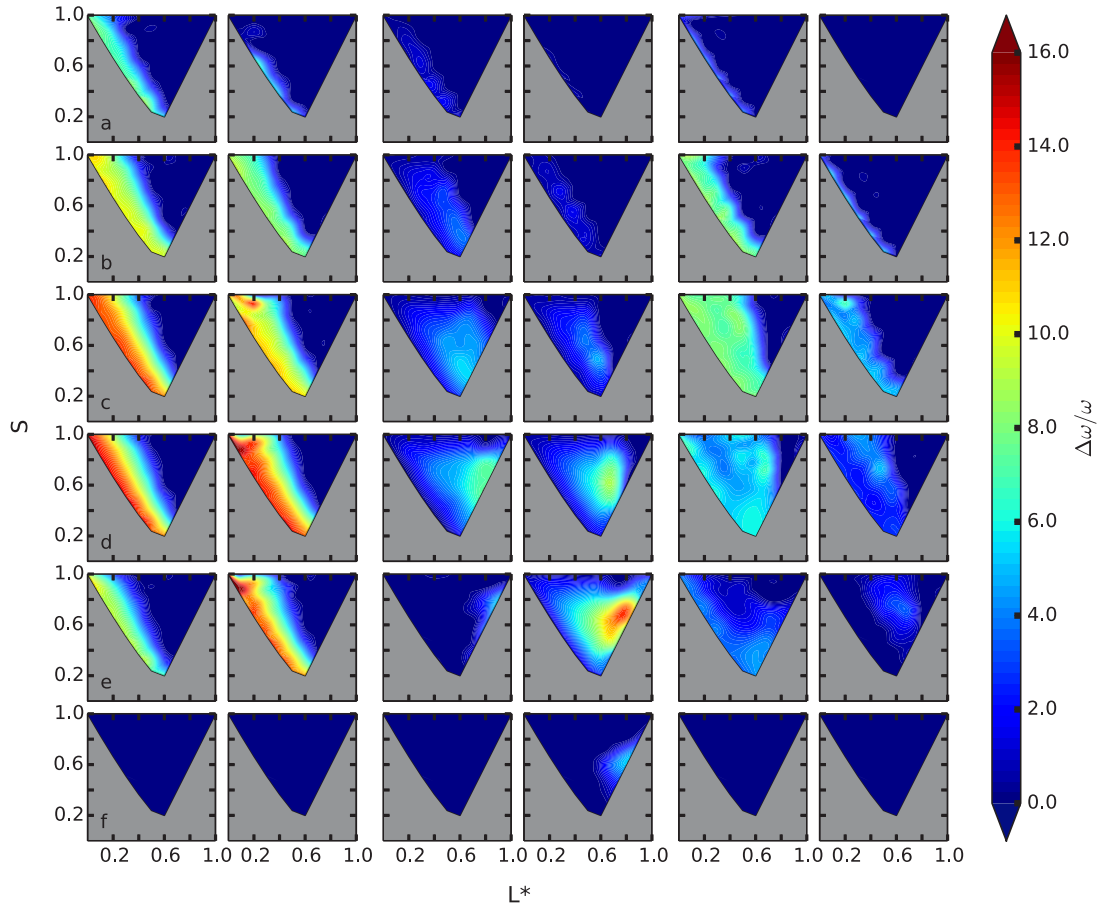


Figure 5.5: Maximum even mode gaps in dimer cylinder and dimer particle bases for  $r_l$  values of a) 0.25, b) 0.30, c) 0.35, d) 0.40, e) 0.45, f) 0.50 (tangent). The left column pair corresponds to the 1 – 2 band gap, the center column pair corresponds to the 2 – 3 band gap and the right column pair corresponds to the 3 – 4 band gap. Within column pairs the cylinder motif is modeled on the left and dimer bases on the right.

1 – 2 gaps occurred in regions I and II for cylinders at all basis separations beyond the tangent dimer cylinder arrangement. The even mode 1 – 2 band gap tolerated higher filling fraction ( $f = 27.0 – 80.8\%$ ) than the odd mode gaps (Figure 5.4). Similar features in the contour plots for dimer cylinders (Figure 5.5a-d) were apparent in Figure 5.5b-e for dimer particles, corresponding to a 10% decrease in basis separation. The 2 – 3 even mode gaps exhibited moderate gap sizes up to  $\Delta\omega/\omega = 7.3\%$  for region III dimer cylinder shapes at  $r_l = 0.40$ ,  $f = 48.0 – 55.0\%$ . Region IV dimer cylinders only yielded a 5.3% even mode gap and no odd mode gaps. Similar even gap size and shape parameter ranges in the contour plots were found shifted by a 10% decrease in basis separation between dimer cylinder and dimer particle. However, sizable gaps up to 13.6% were found in dimer particles at  $r_l = 0.45$  due to the relatively low filling fraction in region III (Figure 5.4e, right). A wide range of shape parameters (regions I-III) corresponding to moderately sized 3 – 4 even gaps were supported in dimer cylinders at  $r_l = 0.35$ ,  $f = 36.7 – 57.8\%$ . Higher lying 5 – 6 even mode gaps were found for shape parameter region I in dimer cylinder crystals, as well (Supplemental Figure 5.6). More modest gap sizes for the even mode gaps (i.e.,  $\Delta\omega/\omega_{max} = 14.6\%$ ) reflect the lack of dielectric continuity for isolated dimer cylinders. Even mode gaps tend to be optimized in the case of high connectivity of the dielectric regions. [10]

The cylinder arrangements mapped in the contour plots belong to the plane symmetry groups  $p6mm$  ( $L^* = 0.0$ ,  $S = 1.00$ ),  $c2mm$  ( $L^* \neq 0.0$ ,  $S = 1.00$ ) and  $c1m1$  ( $L^* > 0.0$ ,  $S < 1.00$ ). Hexagonal distortions up to 13% (region I) yielded the largest gaps and up to 37.5% (regions I-III) still supported significant gaps. The point group for region I shapes was reduced to  $m$  ( $C_s$ ) compared to circular cross-section holes on a hexagonal lattice with point group  $6mm$ . However, the Brillouin zone remained highly isotropic. The 2 – 3 and 3–4 even gaps and 3–4 odd gaps for shape parameter regions II and III maintained sizable gap widths despite moderate lattice anisotropy. Region IV based crystals associated with

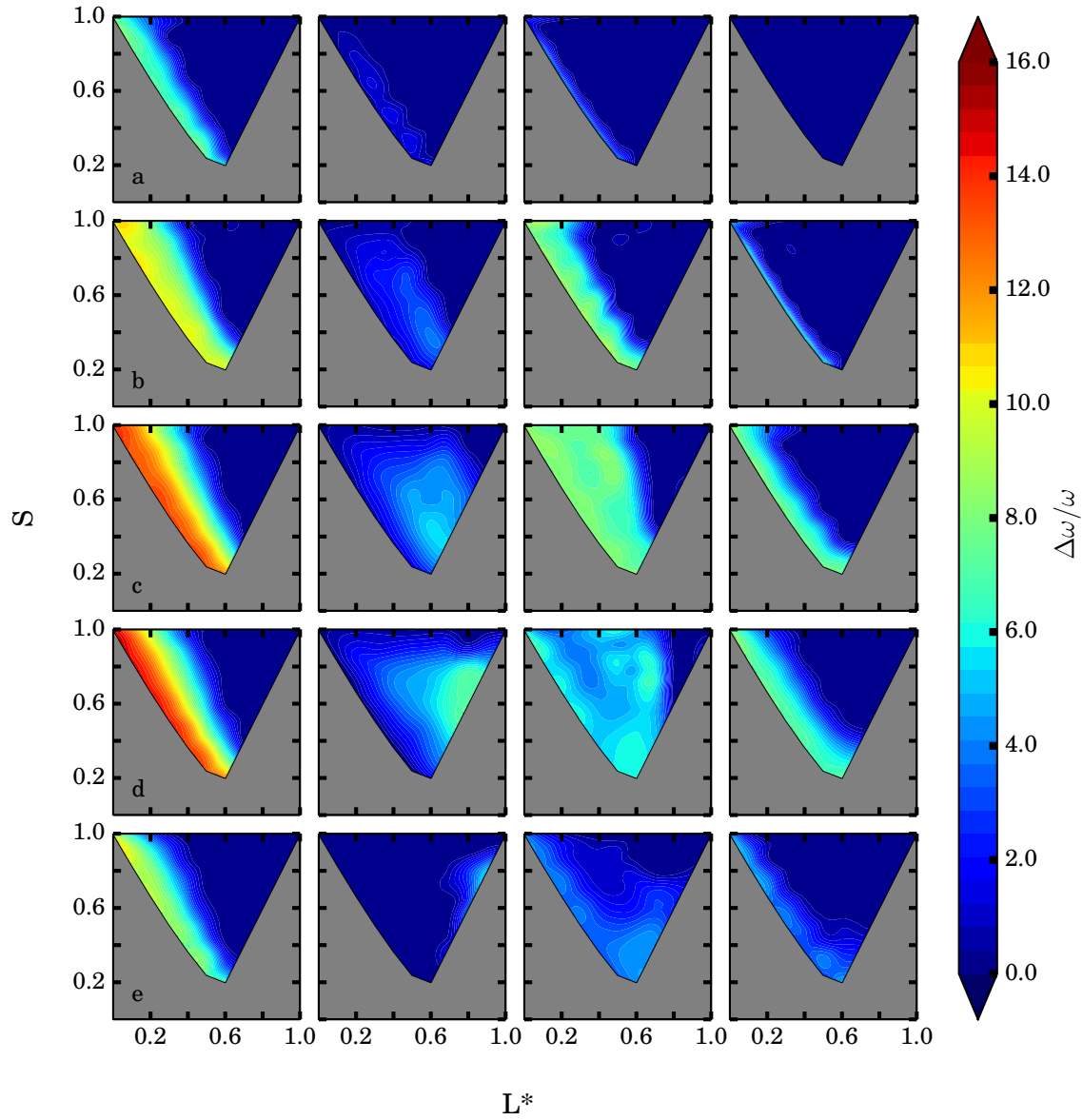


Figure 5.6: Contour plots of largest even gaps for gap indices 1 – 2 (left), 2 – 3 (left center), 3 – 4 (right center) and 5 – 6 (right) at a)  $r_l = 0.25$ , b)  $r_l = 0.30$ , c)  $r_l = 0.35$ , d)  $r_l = 0.40$ , e)  $r_l = 0.45$ .

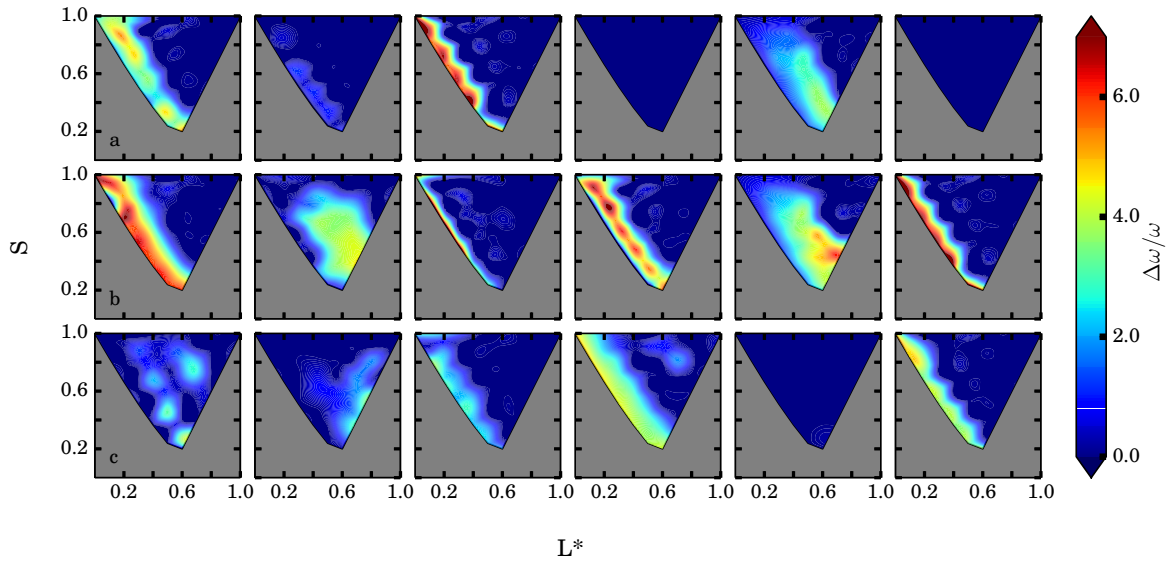


Figure 5.7: (left to right) Contour plots of maximum polarization independent gap indices 4 odd–5 odd from overlapping 4 – 5 odd and 3 – 4 even gaps, 3 odd–3 even from overlapping 3 – 4 odd and 2 – 3 even gaps, 4 odd–4 even from overlapping 4 – 5 odd and 3 – 4 even gaps, 3 even–5 odd from overlapping 4 – 5 odd and 3 – 4 even gaps, 2 even–3 even from overlapping 3 – 4 odd and 2 – 3 even gaps, and 3 even–4 even from overlapping 3 – 4 even and odd gaps for  $r_l$  values of a) 0.30, b) 0.35, c) 0.40.

lattice distortions beyond 37.5 % had the most anisotropic Brillouin zones. Thus, the high lobe symmetry, low lobe fusion structures supported limited gap sizes, most less than 5 %.

The polarization independent gaps are given in the contour plots of Figure 5.7 at the dielectric contrasts from 6 to 16 that determined the largest gaps. Basis separations with  $r_l = 0.30 - 0.35$  for shape parameter region I supported overlaps having gap widths ( $\Delta\omega/\omega = 5-6.8\%$ ) between the frequencies of the 4-5 odd and 3-4 even gaps and the 3-4 even and 3-4 odd gaps. Region III cylinder dimers promoted overlaps ( $\Delta\omega/\omega = 4-6.3\%$ ) between the frequencies of the 3-4 odd and 2-3 even gaps. Gap maps of frequency versus dielectric contrast for odd (blue), even (red) and polarization independent (purple) band gaps are provided in Figure 5.8 at basis separation  $r_l = 0.35$  for the range of shape parameters. At  $L^* = 0.0$  and  $S = 1.00$ , the 3-4 odd and 3-4 even mode gaps opened at low dielectric contrasts; the 4-5 odd, 1-2 and 5-6 even gaps opened at moderate dielectric contrasts; and the 2-3 and 5-6 odd mode gaps opened at high dielectric contrasts. The band gaps shifted to higher dielectric contrast and lower frequency as the degree of lobe fusion decreased. A higher optical density was coupled with lower filling fractions due to the change in shape parameter and the bands were pulled under the light cone. As the Brillouin zone became more anisotropic, the light cone frequency bounding the bands decreased. Limitations on polarization independent gap sizes varied, i.e., the 3-4 odd and even gaps developed large gap widths at non-overlapping frequency ranges; the 3-4 even and 4-5 odd band gaps displayed significant frequency overlap and achieved similar but moderate gap sizes; and the small odd mode gap sizes limited the polarization independent gap widths in the cases of overlapping the 1-2 even and 2-3 odd and the 5-6 even and 6-7 odd mode gaps. Supplemental Figures 5.9 and 5.10 provide the gap maps at  $r_l = 0.30$  and  $0.40$ . Decreasing the filling fraction through basis separation opened the gaps at higher dielectric contrasts.

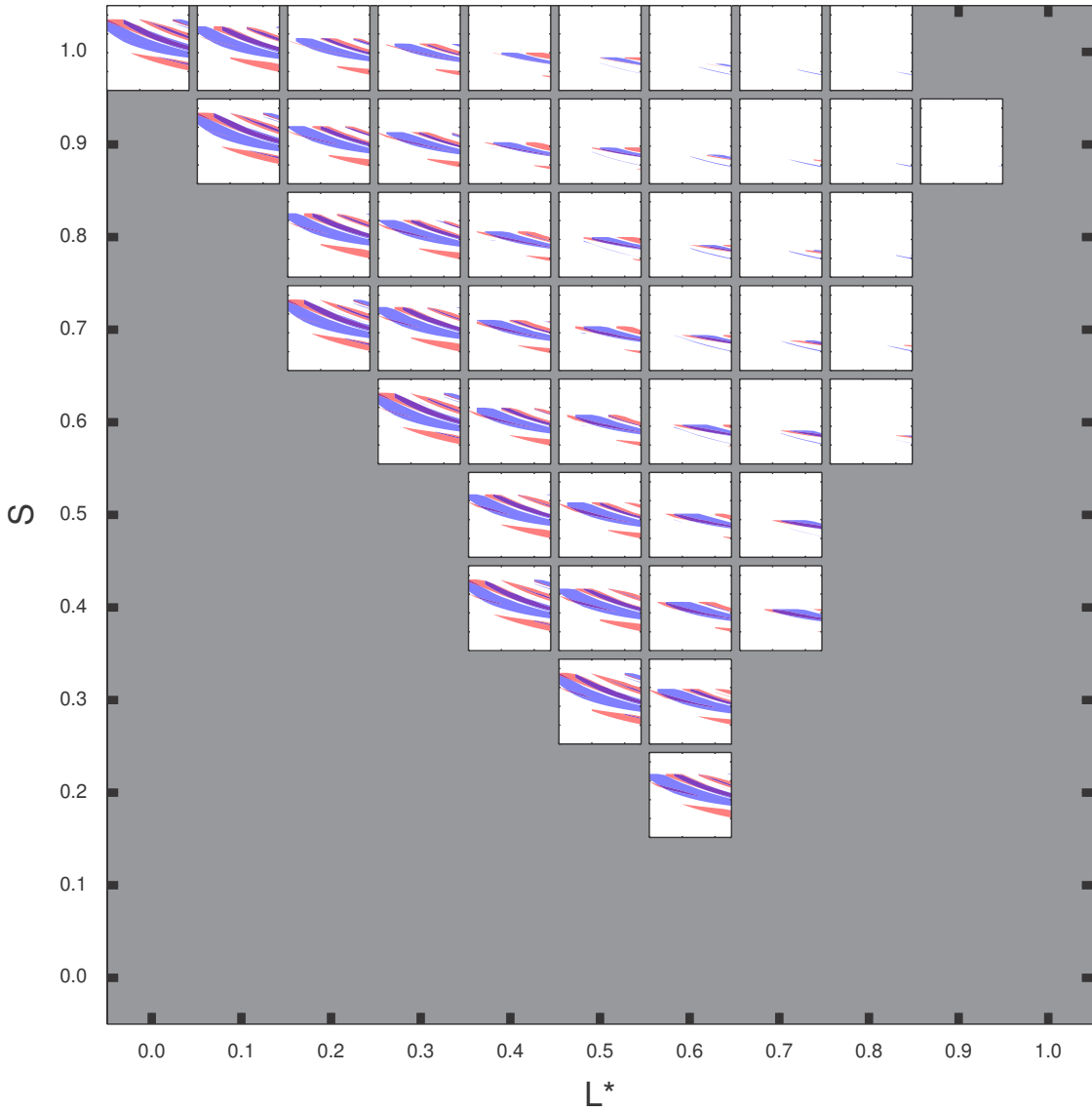


Figure 5.8: Gap maps with odd mode gaps (blue), even mode gaps (red) and overlapped gaps (purple) for asymmetric dimer cylinder structures with  $r_l$  values of 0.35.

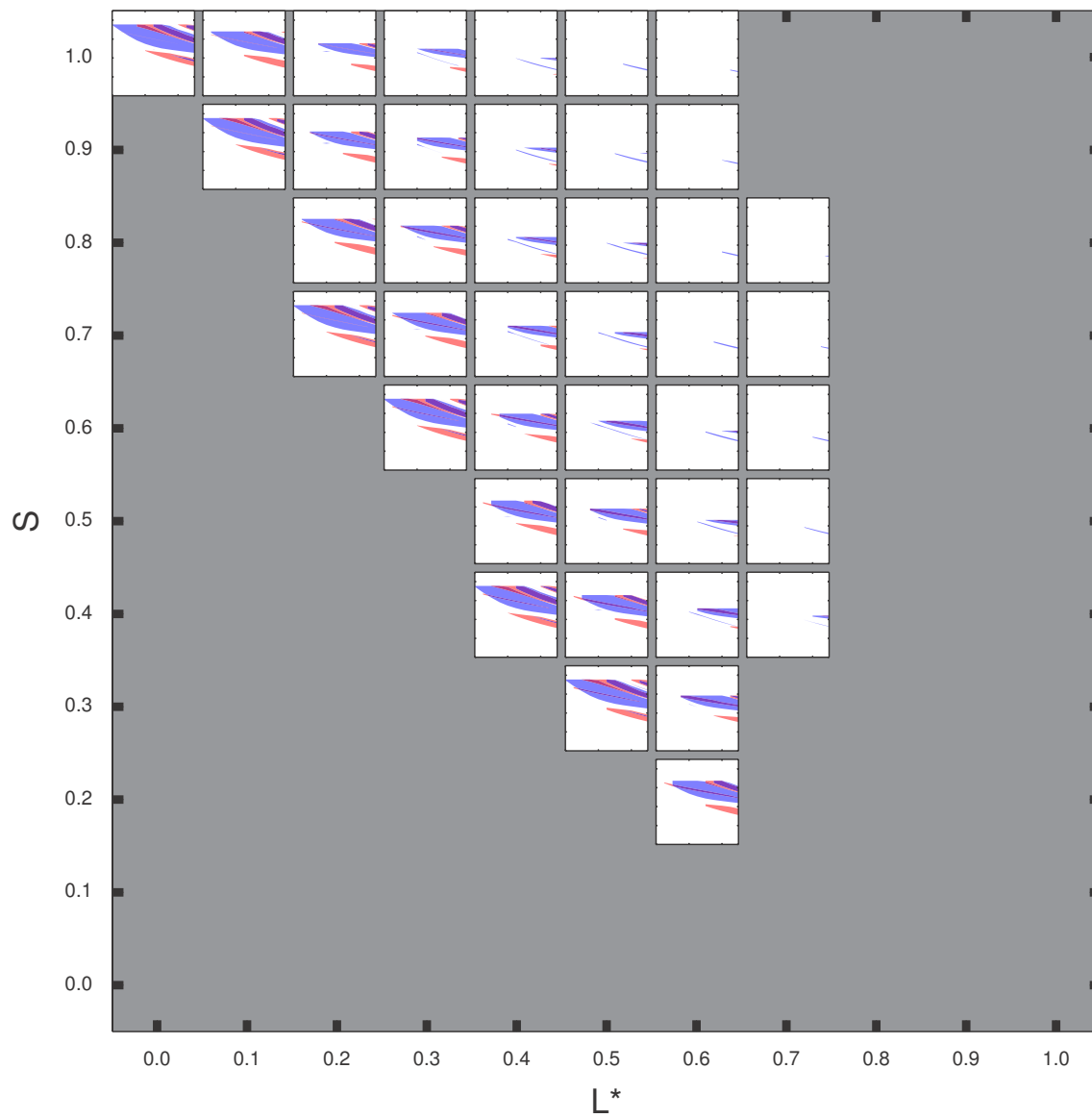


Figure 5.9: Gap maps with odd mode gaps (blue), even mode gaps (red) and overlapped gaps (purple) for dimer cylinder structures with  $r_l$  value of 0.30.

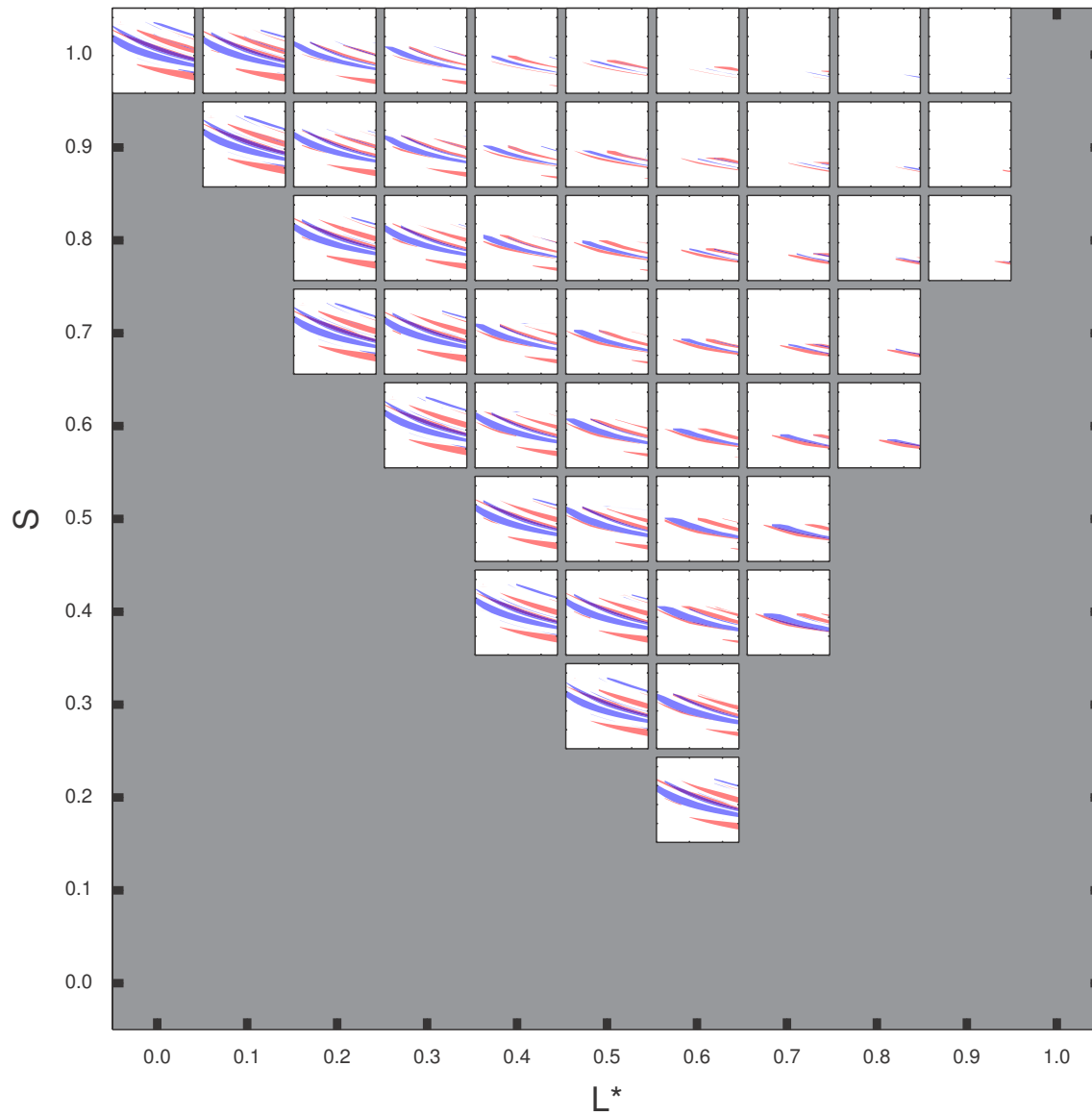


Figure 5.10: Gap maps with odd mode gaps (blue), even mode gaps (red) and overlapped gaps (purple) for dimer cylinder structures with  $r_l$  value of 0.40.

Contour plots of the minimum dielectric contrast necessary for opening band gaps as a function of the structure parameters are shown in the supplemental materials Figure 5.11 (odd modes) and Figure 5.12 (even modes). Large 3 – 4 odd gaps were supported at low dielectric contrasts ( $\epsilon_c = 6$ , ZnS) for shape parameter regions I-III in dimer cylinder structures. The dimer cylinder and the dimer particle plots showed similar features for 10% shift in basis spacing value. For both dimer cylinders and dimer particles the low minimum dielectric contrast value of 6 was found for the 2 – 3 even mode band gaps. However, in dimer cylinders the gaps remained moderate for region III to non-substantial for regions I and II. The dimer particles had large gap sizes that opened at low dielectric contrasts corresponding to region III shape parameters. Table 5.1 lists shape and structural parameters as well as the dielectric contrast to open and maximize gaps with sizes greater than 5%.

The effect of slab height variation on gap size for dimer cylinder arrangements is illustrated in Figures 5.13 and 5.14. The structure leading to the maximum odd mode gap width for all shape parameters ( $r_l = 0.30$ ,  $L^* = 0.1$ ,  $S = 0.83$ ,  $\epsilon_c = 10$ , region I) was examined. The 3 – 4 odd band gap size was largest at  $h^* = 1.0$ . The corresponding band diagram is provided in Figure 5.13c. Higher index gaps were supported that reached moderate sizes at increased slab height, i.e.,  $\Delta\omega/\omega_{max} = 9.7\%$  at  $h^* = 1.6$  for 4 – 5 odd gap and  $\Delta\omega/\omega_{max} = 7.8\%$  at  $h^* = 3.4$  for 6 – 7 odd gap. For the even mode in the case of a moderately fused, moderately asymmetric dimer cylinders ( $r_l = 0.40$ ,  $L^* = 0.7$ ,  $S = 0.7$ ,  $\epsilon_c = 16$ , region III), the 2 – 3 even mode gap was present ( $\Delta\omega/\omega = 5.8\%$ ) and the 3 – 4 even gap was maximized to  $\Delta\omega/\omega = 6.1\%$  at  $h^* = 1.0$ . From slab height  $h^* = 1.0$  to 0.48, the 2 – 3 even gap attained a maximum gap size of 7.8%. The band diagram for the structure at  $h^* = 1.0$  is presented in Figure 5.13d. Even gaps for higher band indices with maximum gap sizes less than 5% opened for thicker or thinner slabs including the 4 – 5 gap at  $h^* = 0.2$ , the 6 – 7 gap at  $h^* = 1.4$  and the 8 – 9 gap at  $h^* = 3.1$ .

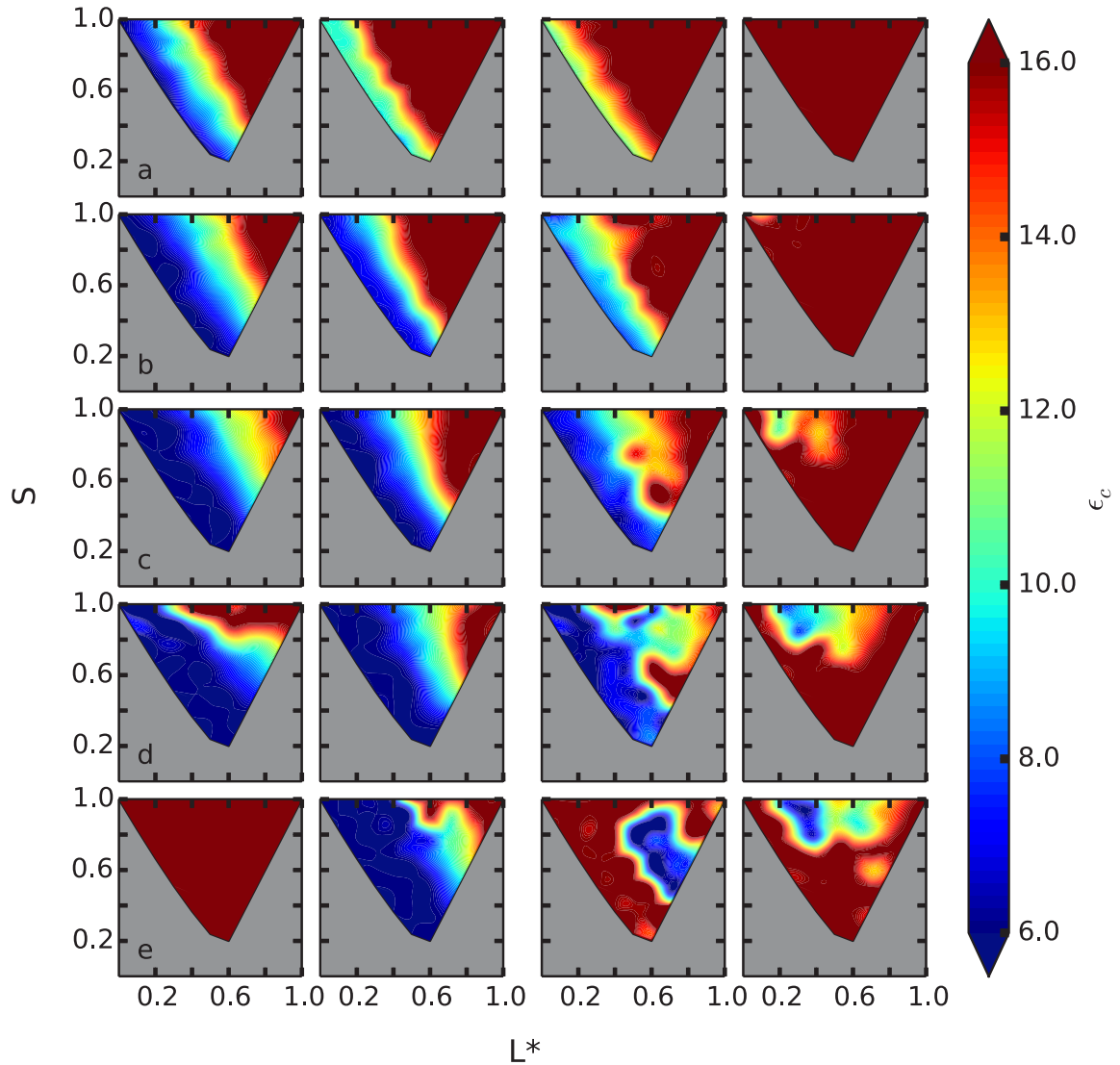


Figure 5.11: Minimum dielectric contrasts for odd mode gaps in dimer cylinder and dimer particle bases at  $r_l$  values of a) 0.30, b) 0.35, c) 0.40, d) 0.45, e) 0.50 (tangent). The left column pair corresponds to the 3 – 4 band gap and the right column pair corresponds to the 4 – 5 band gap. Within column pairs the cylinder motif is modeled on the left and dimer bases on the right.

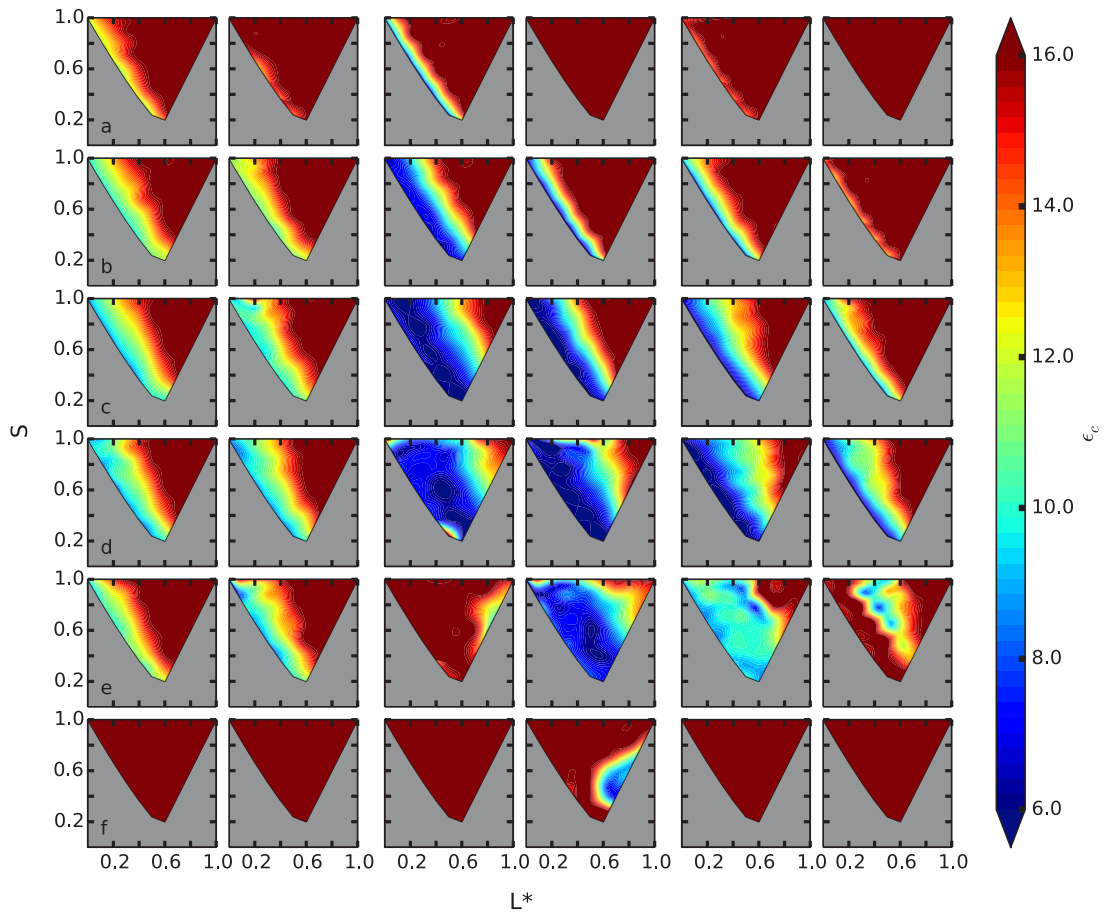


Figure 5.12: Minimum dielectric contrasts for even mode gaps in dimer cylinder and dimer particle bases at  $r_l$  values of a) 0.25, b) 0.30, c) 0.35, d) 0.40, e) 0.45, f) 0.50 (tangent). The left column pair corresponds to the 1–2 band gap, the center column pair corresponds to the 2 – 3 band gap and the right column pair corresponds to the 3 – 4 band gap. Within column pairs the cylinder motif is modeled on the left and dimer bases on the right.

Table 5.1: Shape and structural parameters yielding maximum gap sizes for direct slabs with  $h^* = 1.0$ . The corresponding dielectric contrasts for maximum gap widths and minimum dielectric contrasts opening the gaps are provided.

Polarization	Gap index	$L^*$	$S$	$r_l$	$f$ (%)	Max $\Delta\omega/\omega_m$ (%)	$\epsilon_c$	Min $\epsilon_c$
Odd	3-4	0.4	0.37	0.25	24.5	16.0	15.0	11.0
Odd	3-4	0.1	0.83	0.30	41.8	19.1	10.0	6.0
Odd	4-5	0.0	1.00	0.30	45.7	8.6	16.0	11.0
Odd	3-4	0.6	0.20	0.35	43.0	15.5	9.0	6.0
Odd	4-5	0.0	1.00	0.35	57.8	8.5	15.0	8.0
Odd	3-4	0.6	0.30	0.40	53.6	10.4	9.0	6.0
Odd	4-5	0.0	1.00	0.40	69.6	6.9	11.0	6.0
Odd	3-4	0.6	0.30	0.45	67.8	5.5	8.0	6.0
Even	1-2	0.1	0.83	0.25	30.5	7.6	16.0	12.0
Even	1-2	0.1	0.83	0.30	41.8	10.5	16.0	10.0
Even	3-4	0.2	0.67	0.30	38.7	8.7	12.0	8.0
Even	5-6	0.5	0.24	0.30	34.0	6.1	16.0	14.0
Even	1-2	0.0	1.00	0.35	57.8	13.5	16.0	9.0
Even	2-3	0.6	0.40	0.35	40.3	5.3	9.0	7.0
Even	3-4	0.0	1.00	0.35	57.8	8.7	10.0	6.0
Even	5-6	0.0	1.00	0.35	57.8	8.4	16.0	10.0
Even	1-2	0.0	1.00	0.40	69.6	14.6	16.0	9.0
Even	2-3	0.8	0.60	0.40	48.0	7.3	14.0	11.0
Even	3-4	0.7	0.70	0.40	52.2	6.1	16.0	13.0
Even	5-6	0.0	1.00	0.40	69.6	7.9	15.0	7.0
Even	1-2	0.1	0.83	0.45	78.9	9.3	16.0	10.0
Even	2-3	0.9	0.80	0.45	63.3	5.3	16.0	12.0
Both	4 odd-4 even	0.2	0.77	0.30	38.7	6.2	15.0	12.0
Both	4 odd-5 odd	0.2	0.87	0.30	39.4	5.1	16.0	14.0
Both	2 even-3 even	0.7	0.40	0.35	37.5	5.2	12.0	12.0
Both	4 odd-4 even	0.3	0.51	0.35	48.5	6.3	11.0	8.0
Both	3 even-4 even	0.4	0.37	0.35	47.1	6.8	12.0	12.0

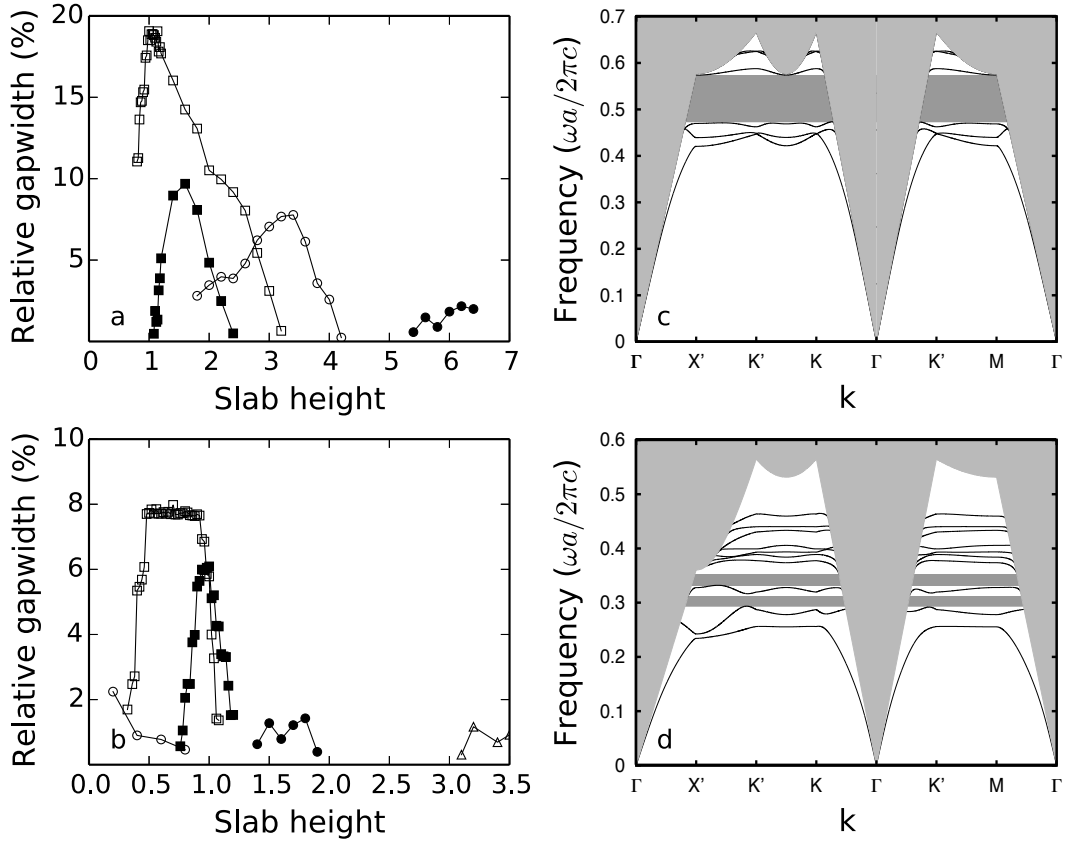


Figure 5.13: Relative gap width variation with slab height,  $h^*$ . a) Odd modes for  $r_l = 0.30$ ,  $L^* = 0.1$ ,  $S = 0.83$ ,  $\epsilon_c = 10$ , where gap indices are 3 – 4 (open square), 4 – 5 (filled square), 6 – 7 (open circle) and 9 – 10 (filled circle). b) Even modes for  $r_l = 0.40$ ,  $L^* = 0.7$ ,  $S = 0.7$ ,  $\epsilon_c = 16$ , where gap indices are 2 – 3 (open square), 3 – 4 (filled square), 4 – 5 (open circle), 6 – 7 (filled circle), 8 – 9 (open triangle). The corresponding band diagrams of maximum c) odd mode band gap and d) even mode band gap structures at slab height  $h^* = 1.0$ .

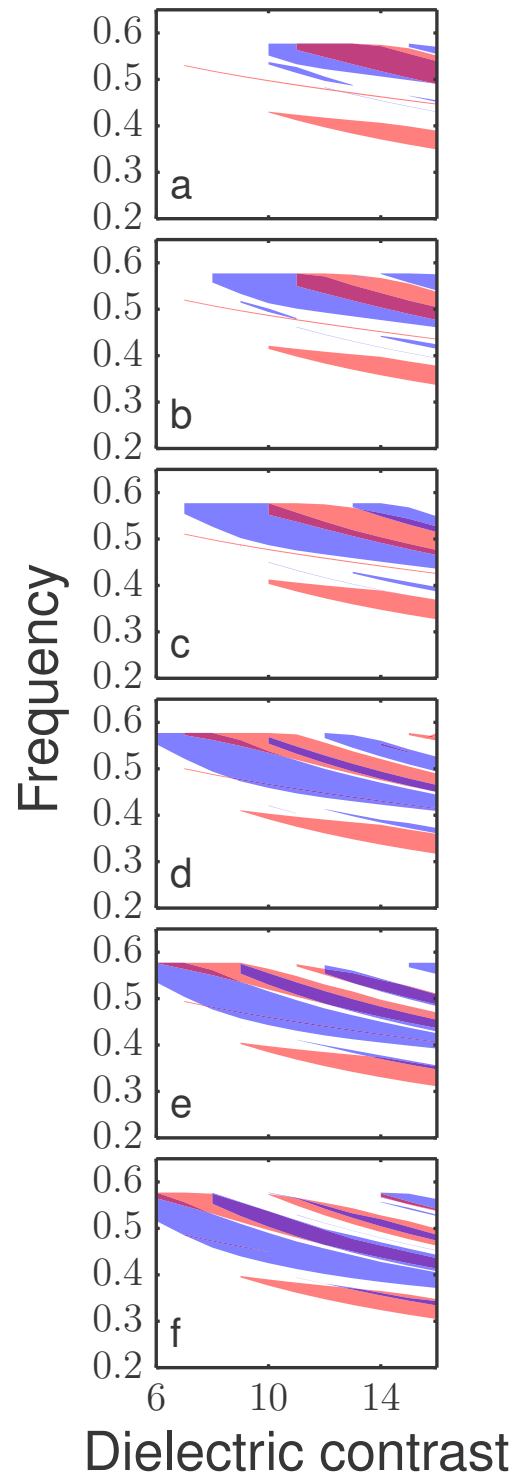


Figure 5.14: Gap maps for  $r_l = 0.35$ ,  $L^* = 0.1$ ,  $S = 0.83$  at slab heights a)  $h^* = 0.5$ , b)  $h^* = 0.6$ , c)  $h^* = 0.7$ , d)  $h^* = 0.8$ , e)  $h^* = 0.9$ , f)  $h^* = 1.0$ .

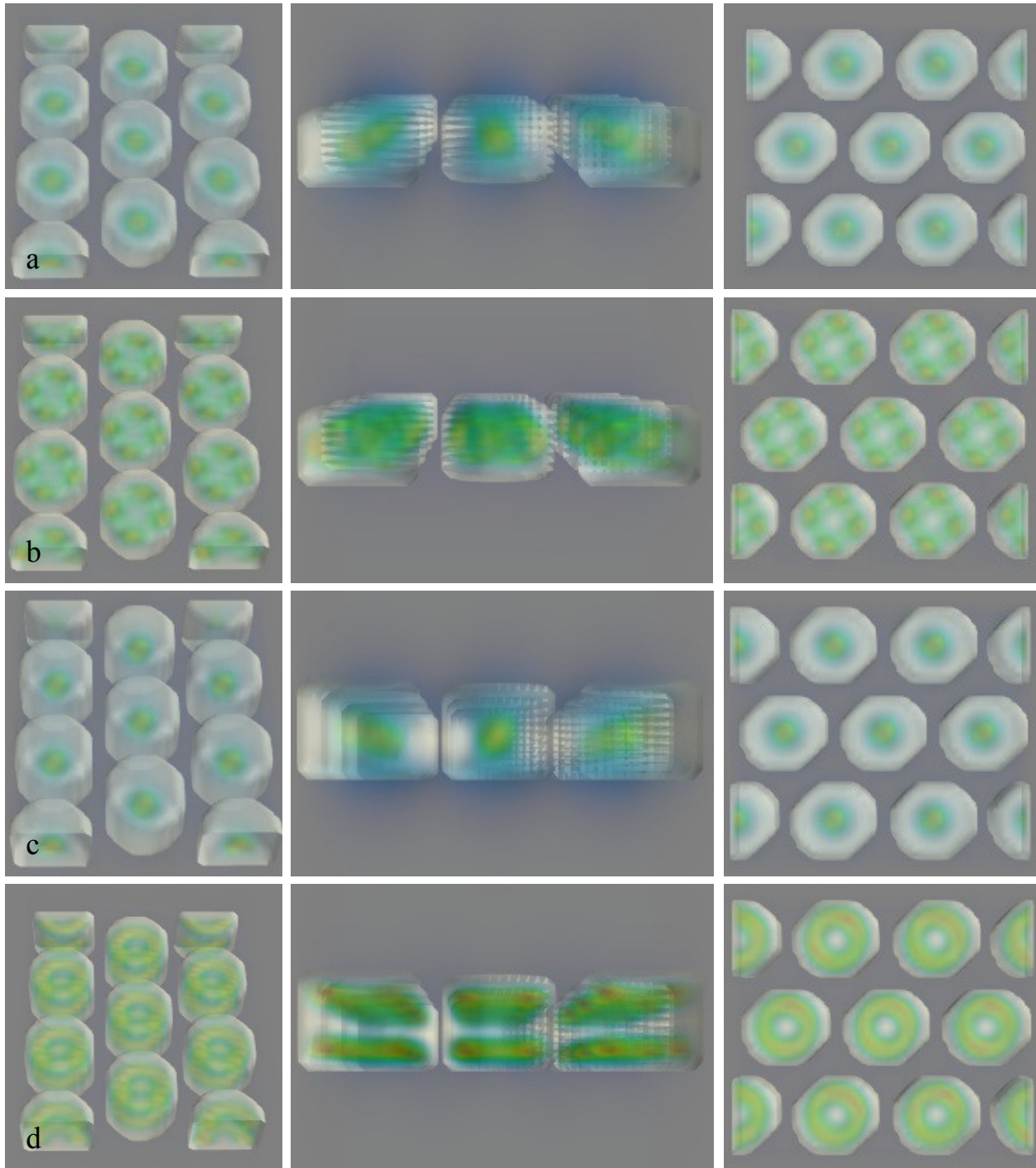


Figure 5.15: Displacement field (i.e., dielectric constant  $\times$  electric field) at the  $K'$  symmetry point for dimer cylinders at structure parameters  $r_l = 0.35$ ,  $L^* = 0.1$ ,  $S = 0.83$ ,  $\epsilon_c = 14$ . a) 3rd odd band,  $h^* = 0.5$ , b) 4th odd band,  $h^* = 0.5$ , c) 3rd odd band,  $h^* = 0.7$  and d) 4th odd band,  $h^* = 0.7$ .

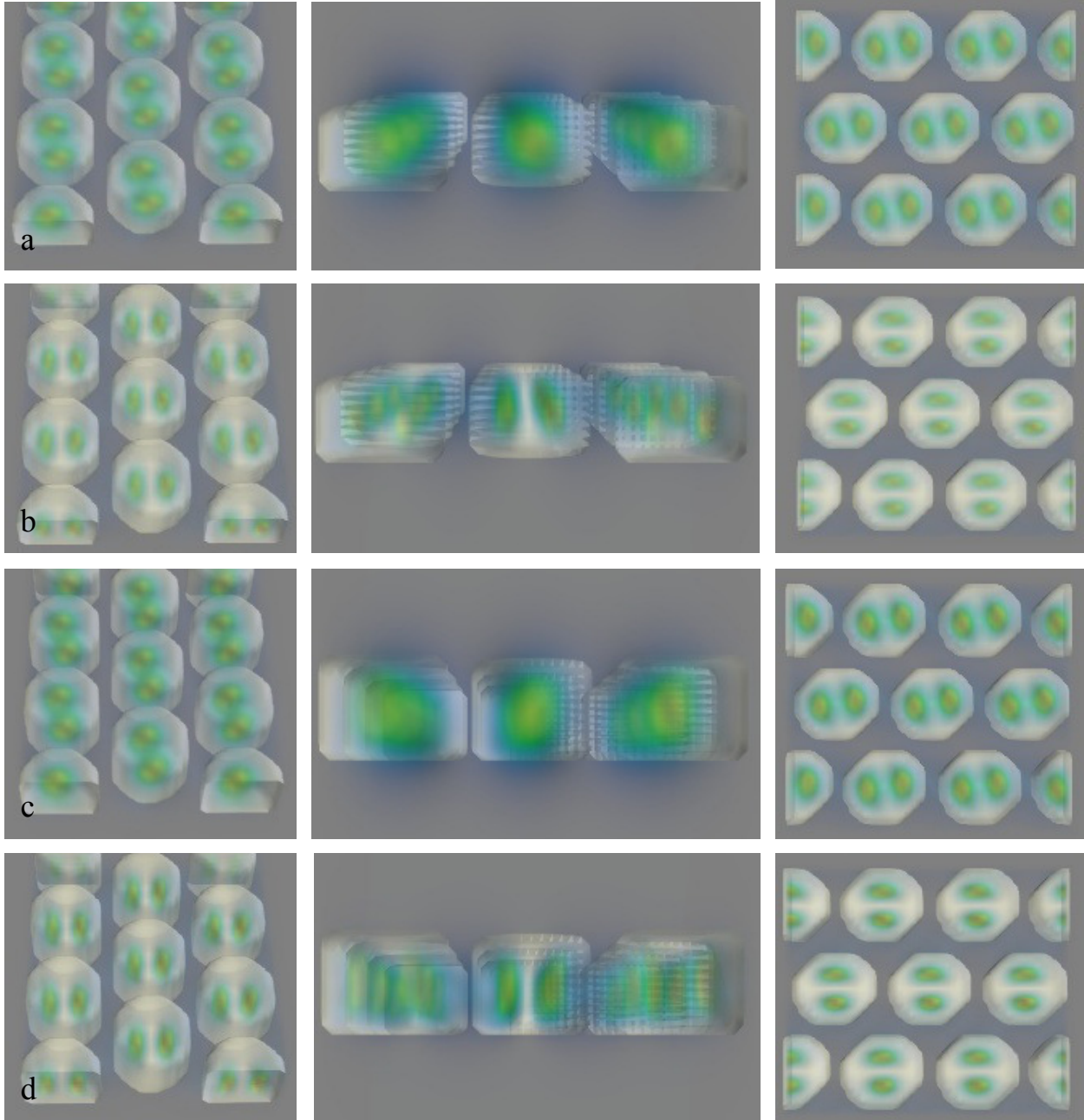


Figure 5.16: Magnetic field distribution at the  $K'$  symmetry point for dimer cylinders at structure parameters  $r_l = 0.35$ ,  $L^* = 0.1$ ,  $S = 0.83$ ,  $\epsilon_c = 14$ . a) 3rd even band,  $h^* = 0.5$ , b) 4th even band,  $h^* = 0.5$ , c) 3rd even band,  $h^* = 0.7$  and d) 4th even band,  $h^* = 0.7$ .

Figure 5.14 provides gap maps as a function of slab height for region I cylinder dimers with  $r_l = 0.35$ ,  $L^* = 0.1$  and  $S = 0.83$ . Multiple overlapped gaps at  $h^* = 1.0$  transitioned to an optimum 9.9% gap size as slab thickness decreased to  $h^* = 0.5$ . The predominant overlapping 3 – 4 even and 4 – 5 odd gap diminished in size and closed at  $h^* = 0.7$ . The 3 – 4 even and odd gaps intersected for moderate to high dielectric contrasts at  $h^* = 0.7$  and increased in frequency overlap as the gaps shifted towards higher frequency for thinner slabs. The frequency overlap of the 3–4 odd and even mode gaps can be rationalized from the displacement field (i.e., dielectric constant  $\times$  electric field) and magnetic field distributions in the dielectric material as shown in Supplemental Figures 5.15 and 5.16. Magnetic field maps associated with the 3rd and 4th even bands at the  $K'$  symmetry point were unchanged in distribution at  $h^* = 0.7$  and the reduced slab thickness,  $h^* = 0.5$  (Figure 5.16). Thus, the even gap frequency span remained largely constant as the height changed. The 4th odd mode displacement field at slab thickness  $h^* = 0.7$  was concentrated in two annular regions, separated in the vertical direction. As the slab height was reduced to  $h^* = 0.5$ , a configuration of four discontinuous coplanar nodes was adopted, indicative of the band shifted to higher frequency. The polarization independent gap size at  $h^* = 0.5$  compares favorably with previous reports for champion inverted photonic slabs. For example, triangular cross-section holes in silicon ( $\epsilon_c = 12.2$ ) on a hexagonal lattice yielded a 3.5% gap; a 5.2% gap was found for elliptical cross-section holes on a centered rectangular lattice (effective indices  $n_{TE} = 2.91$  and  $n_{TM} = 2.52$ ); a honeycomb lattice with two hole sizes ( $\epsilon_c = 11.9$ ) on a silica substrate had a 8.6% gap; a 10.2% gap was determined for a hexagonal lattice with rotated hexagonal cross-section holes in silicon ( $\epsilon_c = 11.9$ ); and an ellipse cluster with  $3m$  point symmetry produced an 11% gap. [24, 20, 2, 27] Notably, no polarization independent gap existed (i.e., no gap above threshold of  $\Delta\omega/\omega = 1\%$ ) for direct structures of cylindrical rods on a square lattice and binary-sized circular cross-section holes on a rectangular lattice.[11, 1, 18]

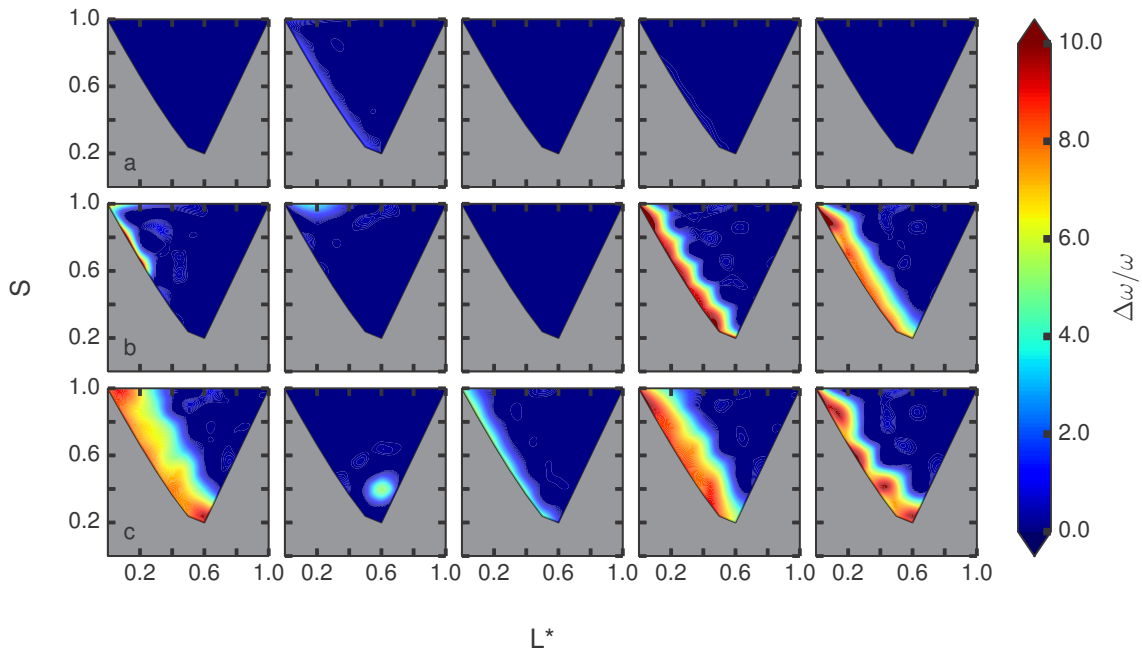


Figure 5.17: Contour plots of maximum polarization independent gap indices 3 odd–4 odd from (left) overlapping 3 – 4 odd and 3 – 4 even gaps, 3 odd–4 even from (left center) overlapping 3 – 4 odd and 3 – 4 even gaps, 6 odd–6 even from (center) overlapping 6 – 7 odd and 5 – 6 even gaps, 3 even–4 odd from (right center) overlapping 3 – 4 odd and 3 – 4 even gaps, 3 even–4 even from (right) overlapping 3 – 4 odd and 3 – 4 even gaps at  $h^* = 0.5$  and  $r_l$  values of a) 0.30, b) 0.35, c) 0.40.

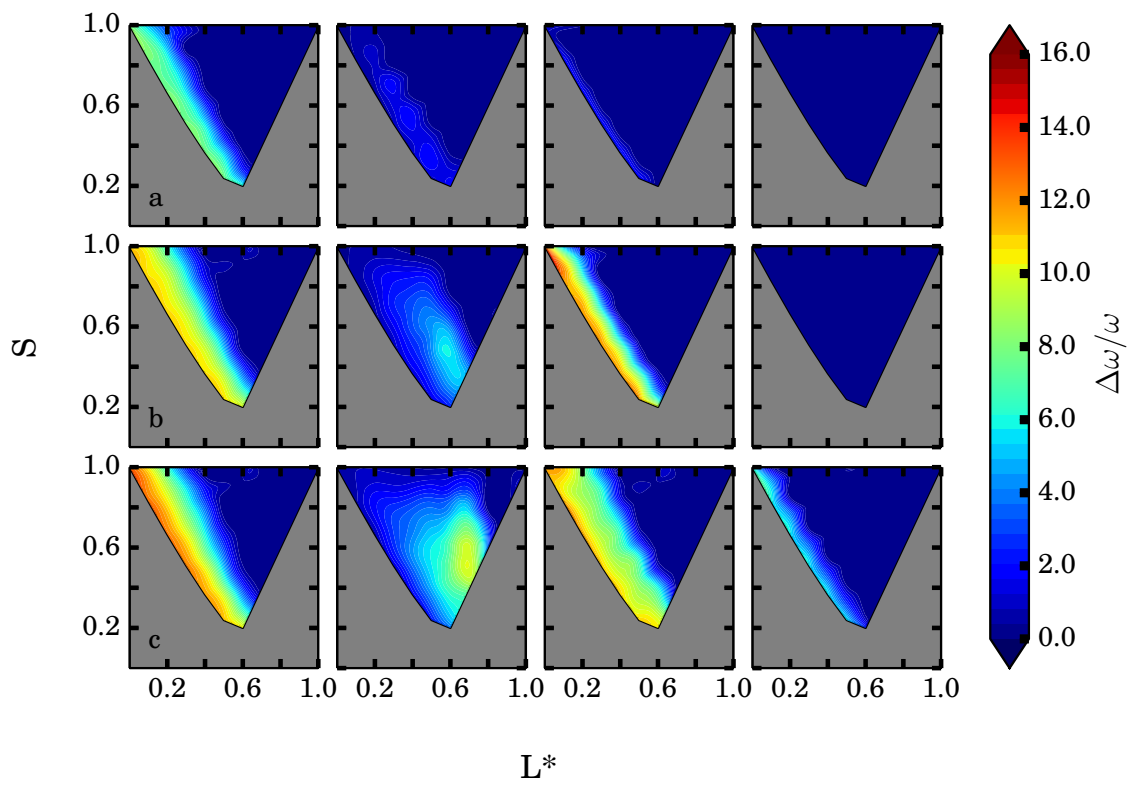


Figure 5.18: Contour plots of largest even gaps for gap indices 1–2 (left), 2–3 (left center), 3–4 (right center) and 5–6 (right) at  $h^* = 0.5$  and  $r_l$  values of a) 0.30, b) 0.35, c) 0.40.

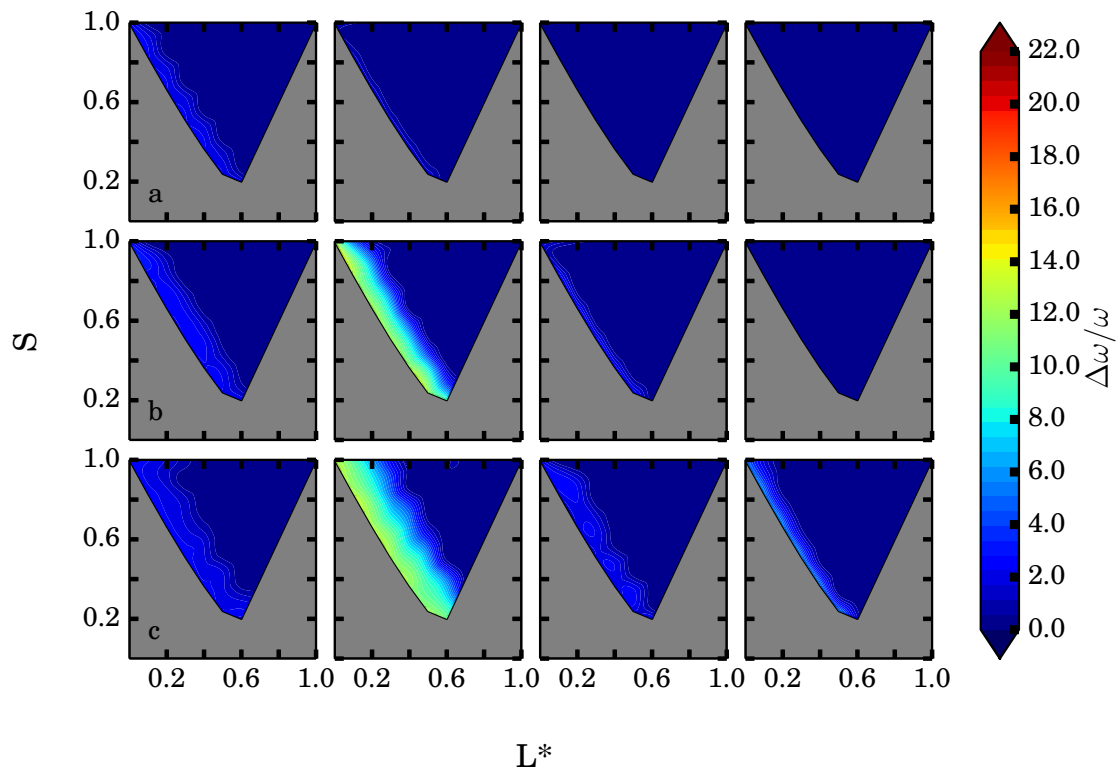


Figure 5.19: Contour plots of odd mode gaps for gap indices 2 – 3 (left), 3 – 4 (center left), 5 – 6 (center right), 6 – 7 (right) at slab height  $h^* = 0.5$  and  $r_l$  values of a) 0.30, b) 0.35, c) 0.40.

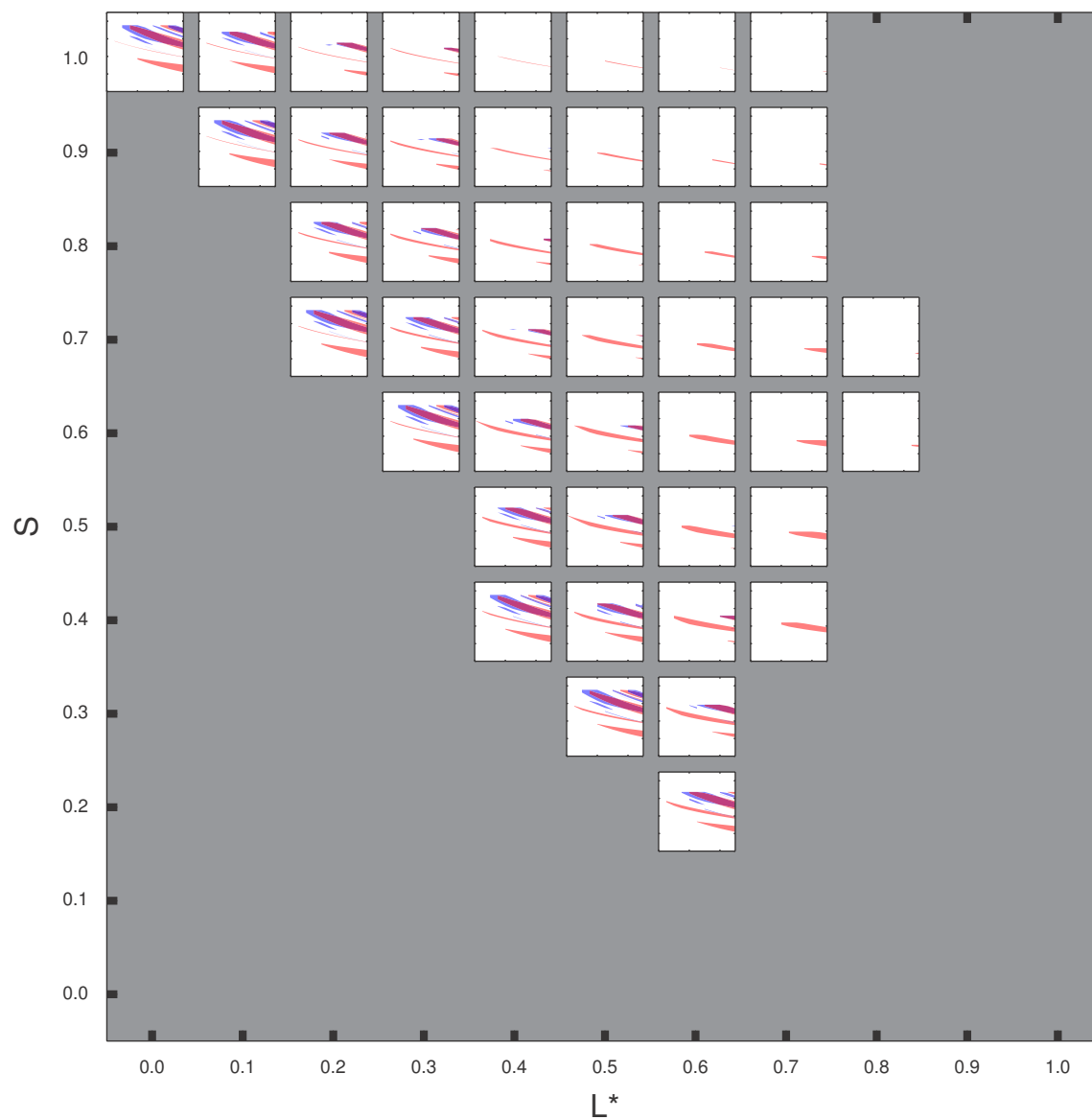


Figure 5.20: Gap maps with odd mode gaps (blue), even mode gaps (red) and overlapped gaps (purple) for direct dimer cylinder structures at  $h^* = 0.5$  with  $r_l$  value of 0.40.

Figure 5.17 displays the gap width dependence on the basis shape in contour plots of the maximum polarization independent gaps for structures with slab height  $h^* = 0.5$ . The 2 – 3 even mode gaps in region III shape parameter space increased in width from 7.3 % at  $h^* = 1.0$  to 9.9 % at the reduced slab height (Supplemental Figure 5.18). The maximum 1 – 2 even gap width in region I shapes decreased from 14.7 % to 12.9 % and the maximum odd mode gap size decreased from 19.1 % to 12.3 % (Supplemental Figure 5.19). However, region I shapes promoted larger polarization independent gap widths at  $h^* = 0.5$  ranging from 6.0 – 9.9 % for overlapping 3 – 4 even and 3 – 4 odd gaps (Supplemental Figure 5.20) in contrast to slab height  $h^* = 1.0$  where the frequency ranges of these gaps were in poor coincidence.

The inverted dimer cylinder structures with  $r_l = 0.45$  at slab height  $h^* = 0.5$  were explored to exploit the effect of connectivity on even gap size.[11] Large 1 – 2 even gaps up to 40.4 % , 34.2 % and 33.0 % were found for shape parameter regions I, II and III, respectively (Supplemental Figure 5.21). The 2 – 3 odd mode gaps only achieved a maximum size of 9.0 %. The hexagonal lattice with single cylinder holes, in comparison, had a 40.8 % even mode gap at a slab height  $h^* = 0.5$ .

As a perspective on fabrication of the direct photonic crystal slabs based on dimer particles and dimer cylinders, the colloidal particles can be self-assembled into large area structures using low cost parallel processing methods versus serial writing of lithographic features. Small perturbations from circular cross-section cylinders (select region I shapes), however, may be more readily achieved in the centered rectangular structures through mask design and formation of dimer cylinders by lithography. Also, filling fractions can be more easily adjusted via basis separation designed into the mask for non-closepacked arrangements. For self-assembly, such structures require advanced techniques including soft core potentials,[31] electrical field[6] and co-assembly with nanoparticles.[30] An-

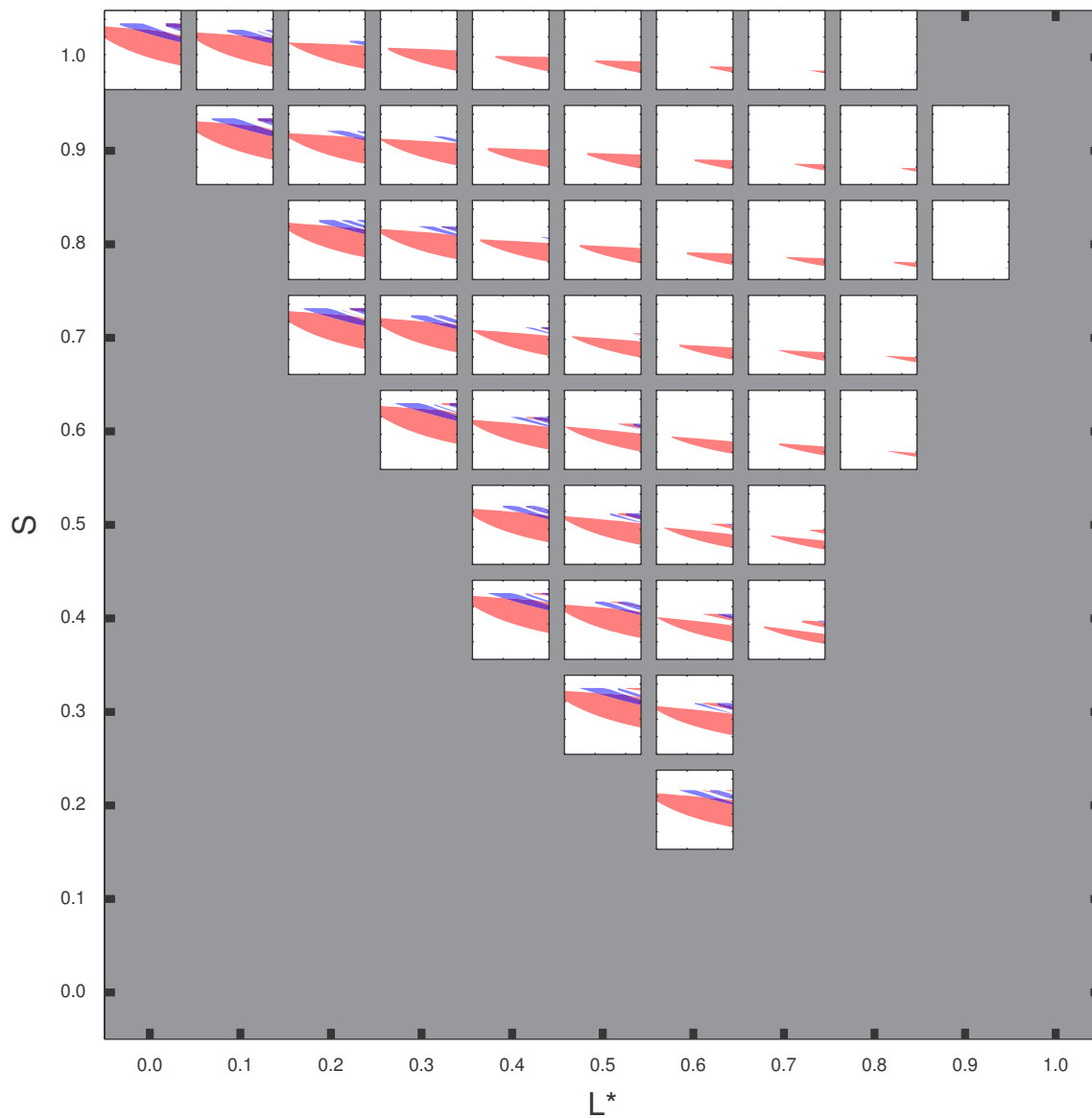


Figure 5.21: Gap maps with odd mode gaps (blue), even mode gaps (red) and overlapped gaps (purple) for inverted dimer cylinder structures at  $h^* = 0.5$  with  $r_l$  value of 0.45.

other constraint is that dimer particle based slabs have height fixed by the particle size and crystal structure. In contrast, slab thickness can be modified with ease using lithographic realizations. Scale up of patterned films has been demonstrated using reel-to-reel micromolding processes from lithographic templates.[8, 23]

## 5.5 Conclusions

In summary, a wide range for degree of lobe fusion and lobe symmetry supported odd, even and polarization independent band gaps in direct dimer cylinder structures. Significant gaps remained at moderate Brillouin zone anisotropy up to 37.5%. In comparison to dimer particles, the shape parameter regions for maximum odd and even gap sizes were found at modified basis separations in dimer cylinder arrangements. The 3 – 4 odd mode gap in the direct slabs and the 1 – 2 even mode gap in the inverted slabs for separated dimer cylinder bases were sizable at low dielectric contrasts. Thus, the slab photonic crystals can be fabricated with a wide range of common materials, i.e., semiconductors. The isolated dimer rods preferentially encouraged odd mode gap formation and the dimer cylinder holes in high connectivity matrix favored even mode gaps. The slab thickness variation brought the large odd and even mode gaps into frequency coincidence for direct structures. The dimer structures here have been inspired by arrangements driven through the thermodynamics of self-assembly. A rich range of crystallographic groups and mesophases (i.e., plastic crystals, degenerate crystals, Archimedean tilings, etc.) can arise from atypical basis shapes and the wide array of appropriate processing methods. Our work suggests that ideation for structural design in slabs is enriched by the combination of thermodynamically-inspired structures with the ease of optimizing slab height (i.e., through lithographic fabrication).

## REFERENCES

- [1] Solomon Assefa, Peter T. Rakich, Peter Bienstman, Steven G. Johnson, Gale S. Petrich, John D. Joannopoulos, Leslie A. Kolodziejski, Erich P. Ippen, and Henry I. Smith. Guiding  $1.5\ \mu\text{m}$  light in photonic crystals based on dielectric rods. *Appl. Phys. Lett.*, 85(25):6110–6112, 2004.
- [2] C. G. Bostan and R. M. de Ridder. Design of photonic crystal slab structures with absolute gaps in guided modes. *J. Opt. Adv. Mat.*, 4:921–928, 2002.
- [3] Julie A. Champion, Yogesh K. Katare, and Samir Mitragotri. Particle shape: A new design parameter for micro- and nanoscale drug delivery carriers. *J. Controlled Release*, 121(1-2):3–9, August 2007.
- [4] E. Y. K. Fung, K. Muangnapoh, and C. M. L. Watson. Anisotropic photonic crystal building blocks: colloids tuned from mushroom-caps to dimers. *J. Mater. Chem.*, 22:10507–10513, 2012.
- [5] R. Gajić, D. Jovanović, K. Hingerl, R. Meisels, and F. Kuchar. 2D photonic crystals on the archimedean lattices (tribute to johannes kepler (1571-1630)). *Opt. Mater.*, 30(7):1065–1069, March 2008.
- [6] T. Gong and D. W. M. Marr. Electrically switchable colloidal ordering in confined geometries. *Langmuir*, 17(8):2301–2304, 2001.
- [7] Masashi Hase, Mitsuru Egashira, Norio Shinya, Hiroshi Miyazaki, Kenji M. Kojima, and Shin-ichi Uchida. Optical transmission spectra of two-dimensional quasiperiodic photonic crystals based on penrose-tiling and octagonal-tiling systems. *J. Alloys Compd.*, 342(1):455–459, 2002.
- [8] Kevin P. Herlihy, Janine Nunes, and Joseph M. DeSimone. Electrically driven alignment and crystallization of unique anisotropic polymer particles. *Langmuir*, 24(16):8421–8426, August 2008.
- [9] I. D. Hosein and C. M. Liddell. Convectively assembled asymmetric dimer-based colloidal crystals. *Langmuir*, 23(21):10479–10485, 2007.
- [10] J. D. Joannopoulos, Steven G. Johnson, Joshua N. Winn, and Robert D. Meade. *Photonic Crystals: Molding the Flow of Light*. Princeton University Press, Princeton, 2nd edition, 2008.

- [11] Steven G. Johnson, Shanhui Fan, Pierre R. Villeneuve, J. D. Joannopoulos, and L. A. Kolodziejski. Guided modes in photonic crystal slabs. *Phys. Rev. B*, 60(8):5751–5758, August 1999.
- [12] Steven G. Johnson and John D. Joannopoulos. Block-iterative frequency-domain methods for maxwell’s equations in a planewave basis. *Opt. Express*, 8(3):173–190, 2001.
- [13] Stephanie H Lee, Esther Y. Fung, E. K. Riley, and C. M. Liddell. Asymmetric colloidal dimers under quasi-2D confinement. *Langmuir*, 25(13):7193–7195, 2009.
- [14] Zhi-Yuan Li, Jian Wang, and Ben-Yuan Gu. Creation of partial band gaps in anisotropic photonic-band-gap structures. *Phys. Rev. B*, 58(7):3721, 1998.
- [15] L. F. Marsal, T. Trifonov, A. Rodríguez, J. Pallares, and R. Alcubilla. Larger absolute photonic band gap in two-dimensional air-silicon structures. *Physica E*, 16(3):580–585, 2003.
- [16] H. Men, N. C. Nguyen, R. M. Freund, K. M. Lim, P. A. Parrilo, and J. Peraire. Design of photonic crystals with multiple and combined band gaps. *Phys. Rev. E*, 83(4):046703, April 2011.
- [17] Ali Mohraz and Michael J. Solomon. Direct visualization of colloidal rod assembly by confocal microscopy. *Langmuir*, 21(12):5298–5306, June 2005.
- [18] Curtis W. Neff, Tsuyoshi Yamashita, and Christopher J. Summers. Observation of brillouin zone folding in photonic crystal slab waveguides possessing a superlattice pattern. *Appl. Phys. Lett.*, 90(2):021102, 2007.
- [19] Susumu Noda. Recent progresses and future prospects of two- and three-dimensional photonic crystals. *J. Lightwave Technol.*, 24(12):4554–4567, December 2006.
- [20] Kris Ohlinger, Yuankun Lin, and Jeremy S. Qualls. Maximum and overlapped photonic band gaps in both transverse electric and transverse magnetic polarizations in two-dimensional photonic crystals with low symmetry. *J. Appl. Phys.*, 106(6):063520, 2009.
- [21] Priyadarshi Panda, Kai P. Yuet, T. Alan Hatton, and Patrick S. Doyle. Tuning curvature in flow lithography: A new class of Concave/Convex particles. *Langmuir*, 25(10):5986–5992, May 2009.

- [22] E. K. Riley, E. Y. Fung, and C. M. Watson. Buckled colloidal crystals with nonspherical bases for two-dimensional slab photonic band gaps. *J. Appl. Phys.*, 111(9):093504–093504, 2012.
- [23] Jason P. Rolland, Benjamin W. Maynor, Larken E. Euliss, Ansley E. Exner, Ginger M. Denison, and Joseph M. DeSimone. Direct fabrication and harvesting of monodisperse, shape-specific nanobiomaterials. *J. Am. Chem. Soc.*, 127(28):10096–10100, 2005.
- [24] Sei-ichi Takayama, Hitoshi Kitagawa, Yoshinori Tanaka, Takashi Asano, and Susumu Noda. Experimental demonstration of complete photonic band gap in two-dimensional photonic crystal slabs. *Appl. Phys. Lett.*, 87(6):061107, 2005.
- [25] Rongzhou Wang, Xue-Hua Wang, Ben-Yuan Gu, and Guo-Zhen Yang. Effects of shapes and orientations of scatterers and lattice symmetries on the photonic band gap in two-dimensional photonic crystals. *J. Appl. Phys.*, 90(9):4307, 2001.
- [26] Matthew D. Weed, Hubert P. Seigneur, and Winston V. Schoenfeld. Optimization of complete band gaps for photonic crystal slabs through use of symmetry breaking hole shapes. *Proc. SPIE*, 7223:72230Q–72230Q–9, February 2009.
- [27] Feng Wen, Sylvain David, Xavier Checoury, Moustafa El Kurdi, and Philippe Boucaud. Two-dimensional photonic crystals with large complete photonic band gaps in both TE and TM polarizations. *Opt. Express*, 16(16):12278–12289, 2008.
- [28] Y. Xia, B. Gates, and Z.-Y. Li. Self-assembly approaches to three-dimensional photonic crystals. *Adv. Mater.*, 13(6):409–413, March 2001.
- [29] Seung-Man Yang, Shin-Hyun Kim, Jong-Min Lim, and Gi-Ra Yi. Synthesis and assembly of structured colloidal particles. *J. Mater. Chem.*, 18(19):2177, 2008.
- [30] Xiaozhou Ye and Limin Qi. Two-dimensionally patterned nanostructures based on monolayer colloidal crystals: Controllable fabrication, assembly, and applications. *Nano Today*, 6(6):608–631, December 2011.
- [31] Anand Yethiraj. Tunable colloids: control of colloidal phase transitions with tunable interactions. *Soft Matter*, 3(9):1099, 2007.
- [32] G.-R. Yi, V. N. Manoharan, E. Michel, M. T. Elsesser, S.-M. Yang, and D. J. Pine. Colloidal clusters of silica or polymer microspheres. *Adv. Mater.*, 16(14):1204–1208, July 2004.
- [33] Y. Yin and Y. Xia. Self-assembly of monodispersed spherical colloids into complex

aggregates with well-defined sizes, shapes, and structures. *Adv. Mater.*, 13(4):267–271, February 2001.